uc3m | Universidad Carlos III de Madrid

University Degree in Biomedical Engineering
2018-2019

Bachelor Thesis

"Implementation and characterisation of radiation detectors based on SIPM for medical imaging"

Alejandro Canales Barroso

Tutores

Juan José Vaquero López

Rigoberto Chil Pérez

Departamento de Bioingeniería e Ingeniería Aeroespacial

Madrid, June 2019

ABSTRACT

In the last decades, medical imaging techniques have revolutionized medicine facilitating the work to the clinicians, favouring the earlier diagnosis of diseases such as cancer, and reducing the time required for surgical procedures. Among these techniques, one of the most promising is Positron Emission Tomography (PET) due to its constant evolution, the functional information it provides and the possibility of combining it with other structural techniques such as CT or MRI. Recently, new generations of PET detectors have been developed leaving behind the conventionally used photomultiplier tubes (PMTs) for the state-of-the-art digital silicone photomultipliers (d-SiPM). In this work, the last generation of radiation detectors, Philips Digital Photon Counting's (PDPC) d-SiPMs, was studied and characterized. These detectors are used in the commercial Philips Vereos time-of-flight PET/CT scanner, as well as in the Hyperion-II^{D} preclinical PET scanner.

The main objective of this work was to learn how to operate this new system in optimum conditions for small-animal imaging, how to design a precise centre of gravity (COG) algorithm for the localization of the scintillator pixels in a scintillator array, and to characterize the energy and spatial resolutions obtained with this PDPC module. Different COG algorithms were tested, and the final one was designed in such a way that only valid events were considered. This algorithm focuses on the main pixel of each event and the eight pixels surrounding it, discarding scatter and noise as much as possible. The energy resolution was measured by studying the full width half maximum (FWHM) of the photopeak, whereas the spatial resolution was measured by computing the valley-to-peak ratio (V/P) and the resolvability index (RI) of a profile taken from the flood field images acquired.

In this project, we used a 30×30 scintillator matrix of LYSO crystals of 1.3×1.3×12 mm^3, coupled to a 50×50×2 mm^3 light guide in order to spread the scintillation photons among 36 of the 64 die sensors integrated in the PDPC DPC 3200-22 module. A study of how the temperature affects the performance of the system and which acquisition parameters, light guide and time window gives better results was performed. As a final check, we compared the initial and final images obtained, considering their spatial and energy resolution.

AKNOWLEDGMENT

I would like to acknowledge my director, Juan José Vaquero, for trusting in me from the first moment, for giving me the opportunity to do the internships and the final degree project in the bioengineering department and having made me feel important, and also for having helped and advised me in any doubt I had.

I would like to thank also Rigoberto Chil for being so patient with me, for having taught me so much these months and for having helped me at any time I asked.

Thanks to my family for being so proud of me, for always supporting me and for their unconditional love.

But specially, thanks to my grandfather for trusting me, for loving me and for supporting me. Although you are no longer with us, I know that you are very proud of me wherever you are. These thanks are especially for you.

TABLE OF CONTENTS

LIST OF FIGURES

LIST OF TABLES

1 INTRODUCTION

1.1 Medical imaging

During the earliest times of medicine, doctors have wanted to see what is inside the human body. To this end, they applied invasive methods which could cause potential damage or trauma. Examples of these invasive methods are cutting the patient’s body or, others less invasive, introducing an endoscope by a cavity to monitor and record what is inside its body.

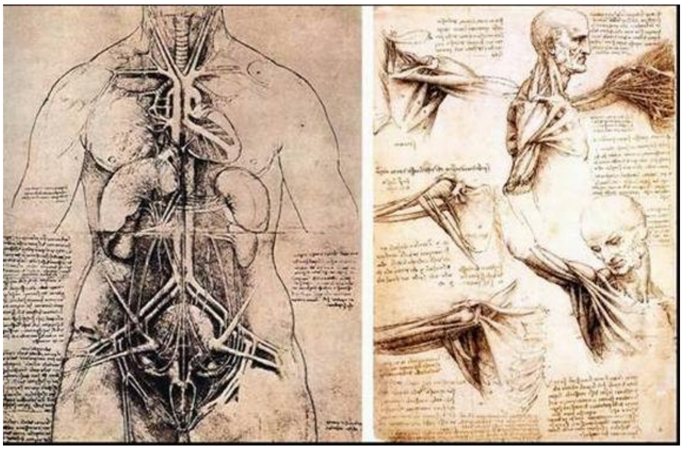

Figure 1: Illustration of ancient anatomy (Da Vinci) [49]

Non-invasive methods are an alternative to these practices. They are termed as medical imaging and they began in November 1895 with Wilhelm Conrad Roentgen's discovery of the X-ray [1]. Medical imaging refers to all the different technologies that are used to view inside the human body in order to diagnose, monitor, or treat medical conditions. Each type of technology gives different information about the area of the body being studied or treated, related to possible disease, injury, or the effectiveness of medical treatment [2].

These non-invasive methods involve irradiating the patient with a certain energy and they can be classified as ionizing methods, able to strip electrons creating highly reactive free radicals and forming ion pairs (photoelectric effect): X-ray, CT and nuclear medicine; and non-ionizing methods, whose energy is not enough to detach an electron from an atom, such as MRI and ultrasound.

Among the different technologies used, we can also classify them into structural or functional imaging depending on the kind of information they provide. Structural imaging (Radiography, CT, ultrasound, MRI) provides information about the anatomy inside the body whereas functional imaging (Nuclear Medicine (SPECT, PET), MRI) provides information about changes in the metabolism, blood flow, etc.

Some of these modalities can be combined in order to obtain a functional image with a better spatial resolution, as it is the case of PET/CT images [3].

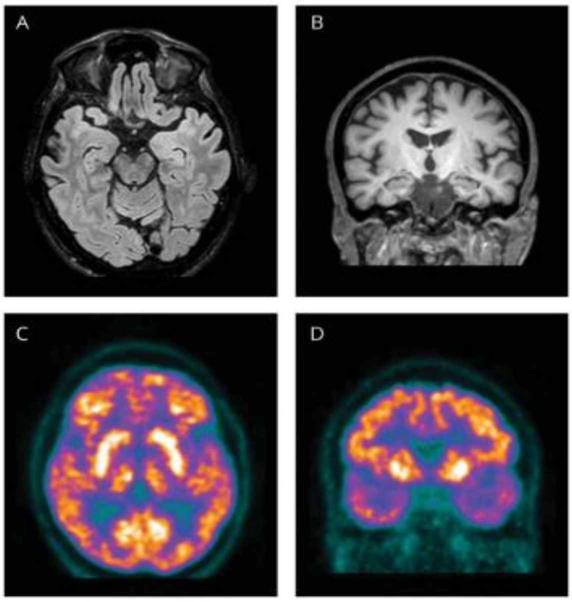

Figure 2: Structural vs. functional medical imaging [50]

1.2 Nuclear Medicine

Nuclear medicine is a functional ionising medical image modality that uses electromagnetic radiation in the form of gamma photons. It involves the administration of a radioactive tracer inside the body to provide diagnostic information. This radiotracer is a labelled compound that consists on a signalling component (the radioactive isotope) detectable from the outside; and an affinity component that determines the biological behaviour by binding to any molecule or macromolecule such as antibodies, proteins, etc. It will finally bind to the target, the final receiver that we want to study.

When the radionuclide decays, it emits electromagnetic radiation in the form of gamma photons, and they are measured by PET or SPECT detectors. The energy of these kind of photons is such that a significant number can exit the body without being scattered or attenuated. The detectors consist on a position-sensitive gamma-ray "camera" that can detect these gamma photons and generate an image of the radiotracer distribution inside the body.

We can divide nuclear medicine imaging in two main types: *single photon emission computed tomography* (SPECT) and *positron emission tomography* (PET). SPECT is based on radionuclides that decay by single photon emission (in general: heavy metals) and consists on a single gamma-camera rotating around the patient. Since several images are obtained from different angles around the patient, the distribution of the radiotracer can be reconstructed in a tomographic image. On the contrary, PET makes use of radionuclides that decay by positron emission (in general: "organic" atoms) with very short lifetime. The positron disintegration produces two gamma photons in "almost" opposite directions that are detected by at least two gamma cameras operating in coincidence (electronic collimation). These detectors are similar to those of SPECT, but they do not need physical collimators and they can detect higher energy photons [4].

1.2.1 PET

In PET, as the tracer with the positron emitting radionuclide is injected in the patient, several phenomena occur. This radionuclide decays emitting a positron which annihilates as it interacts with an electron after travelling a small distance. This distance is known as positron range. The annihilation produces two 511 keV photons in opposite directions 180º apart that will be detected by two gamma detectors facing each other and surrounding the patient.

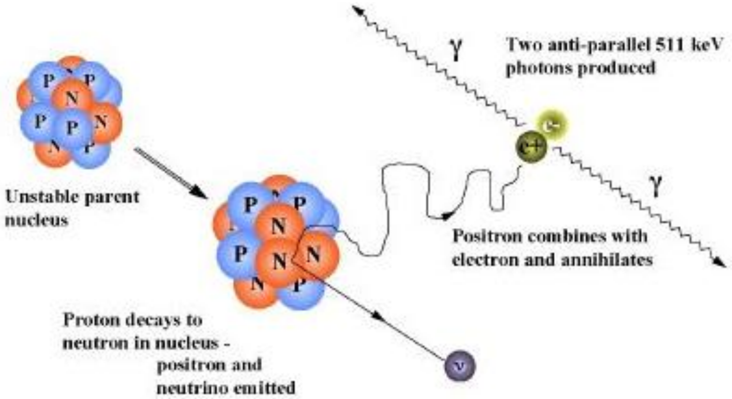

Figure 3: Positron emission and annihilation [5]

The detectors are linked electronically so that we can stablish a time window of a few nanoseconds that is used to discriminate which of the detected events correspond to the same annihilation. This time window is called coincidence window and allows the system to highly improve its efficiency, as only the desired events are detected and the rest, as scatter events or noise, are discarded. Once all the coincidence events are listed, a PET image can be reconstructed using standard tomographic techniques. The results of these tomographic images are the tracer concentration inside the patient's body.

PET systems do no need a physical collimator, as with the coincidence window only the photons of interest are detected providing positional information. Those coincident events corresponding to the same annihilation are assigned to the same line of response (LOR) connecting the two detectors, what is known as electronic collimation.

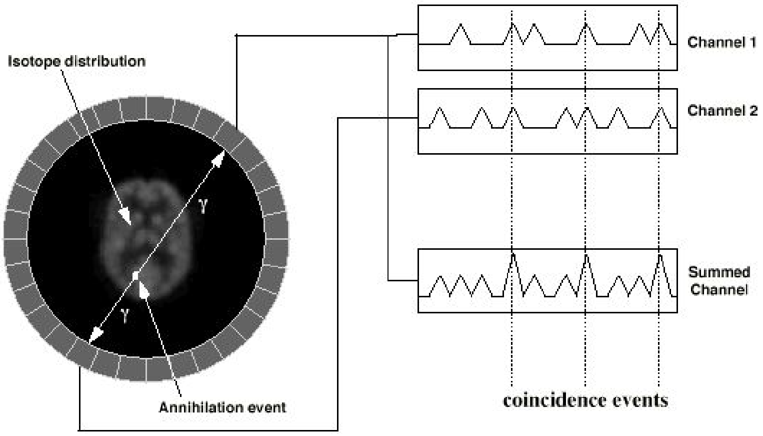

Figure 4: Coincidence detection in PET [5]

We can classify the coincidence events into three different types as we can see in **Figure 5**: true, scattered and random coincidences.

- **True coincidences** occur when a pair of photons from the same annihilation event are detected, without any interaction of the photons and with no other event detected at that time interval.
- **Scattered coincidences** correspond to a pair of photons from the same annihilation event but in which at least one of the photons has suffered any type of scatter. The coincidence event will probably be assigned to the wrong LOR as the direction of the photons has changed during scatter, decreasing contrast resolution and adding noise to the image.
- **Random coincidences** are those in which a pair of photons from different annihilation events are detected in the same coincidence window. This type of coincidences will also add statistical noise to the data [5].

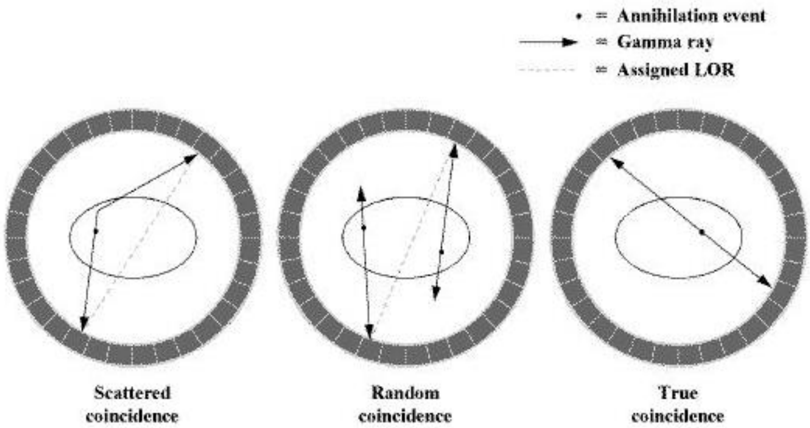

Figure 5: Types of coincidences in PET [5]

1.2.1.1 Time-of-flight PET (TOF-PET)

One of the main problems in conventional PET imaging is that the annihilations are not assigned to the actual location of the event, but along the LOR between the two detectors. To reconstruct the tomographic image, the intersecting 180 degree lines should be calculated considering also the attenuation of the photons, implying a reconstruction with complex mathematical algorithms [6]. In a standard PET, the event has the same probability over the whole line of response. Time of flight PET improves this by assigning a new probability function that improves the prediction of the actual event determining also the difference in the time at which the two photons are detected. The probability on TOF-PET follows a gaussian distribution along the 180-degree line, like is shown on **Figure 6**. The empiric formula used to calculate the actual location of the annihilation event with respect the midpoint between the detectors (Δd) is:

$$\Delta d = \frac{\Delta t \times c}{2} \quad (1)$$

where Δt is the difference in the arrival time of the photons and c is the speed of light ($3 * 10^8\ m/s$). This method improves considerably the image quality, providing better information and facilitating the work to the clinicians [4].

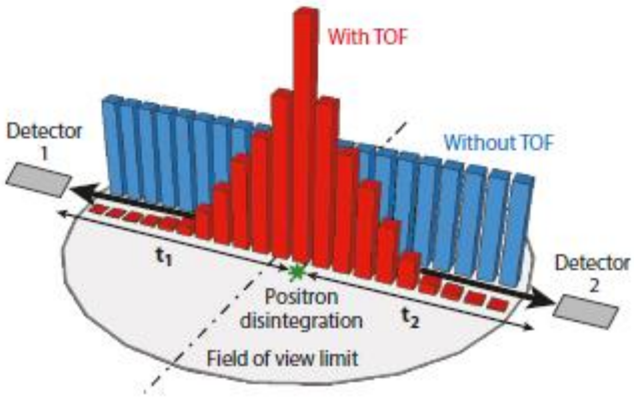

Figure 6: Time-of-flight PET: probability distribution for the scintillation location estimation with and without ToF information [18]

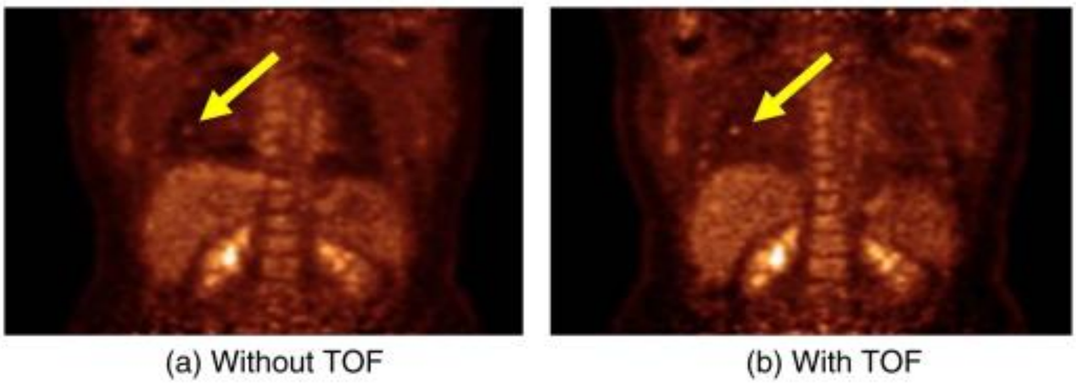

Figure 7: Comparison of a PET image with and without TOF [8]

1.3 Photodetectors

Radiation detectors can detect high energy particles like photos, but we need to convert this into something we can measure, an electric signal. To accomplish this end, most radiation detectors used on nuclear medicine are composed of a scintillator, which converts the gamma photons into light photons, and a photomultiplier tube (PMT), that converts light photons into electric current.

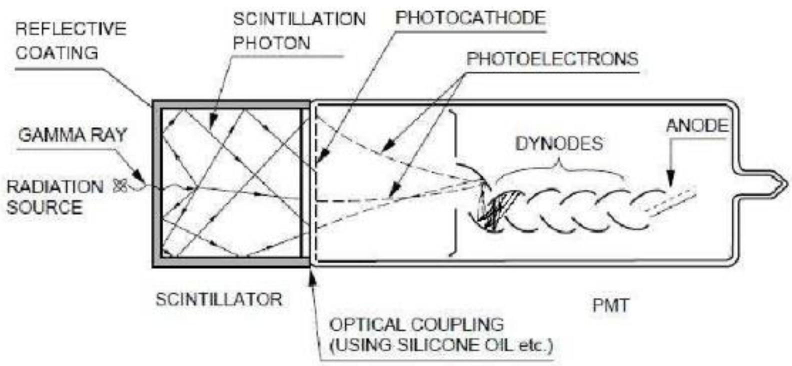

Figure 8: Schematic drawing of a scintillator and PMT detector [9]

Photodetectors used in nuclear medicine can be divided into two main types depending on their operating principle: external photoelectric effect and internal photoelectric effect. In external photoelectric effect, electrons are emitted from the semiconductor into the vacuum when light strikes its surface. On the other hand, in internal photoelectric effect, electrons are excited into the conduction band thanks to the photovoltaic effect. PMTs make use the external photoelectric effect whereas Si photodiodes make use of the photovoltaic effect [7].

1.3.1 Scintillator

A scintillator is a material that absorbs high energy photons such as those emitted in PET, and then, it emits light. The radiation excites the substance by transferring energy modifying its electronic configuration. As the material de-excites, it emits visible light photons [8]. Scintillators can be organic or inorganic materials. Organic scintillators are usually made of aromatic hydrocarbons in crystalline shape, characterized by a low atomic number, and are used for particle detection. Inorganic scintillators in the form of solid crystals are characterized by a higher density and atomic number and are a better choice for radiation detection [9]. The most commonly used scintillator in nuclear medicine is NaI(Tl). This material is used as a scintillator because of its density ($\rho = 3.67$ g/cm^3) and its high atomic number (iodine, Z=53). It can absorb very efficiently gamma radiations in the 50-250 keV range by photoelectric absorption, yielding one visible photon per 30eV. Another important advantage is that this material can be frown inexpensively in large plates, fundamental for imaging detectors. The light emission wavelength from the scintillation process is well-matched to the peak response of the PM tube photocathode.

If higher energies from positron emitters (511 keV) need to be detected, denser scintillators are used. Bismuth germanate (BGO) is characterized by its excellent detection efficiency at this energy, and lutetium oxyorthosilicate (LSO), although is not as efficient as BGO, is much faster and brighter, but it is also more expensive to grow. This last is used for high counting rate detectors. As nuclear medicine is being developed, new scintillator materials are being used. The most promising in this research area are LuAP [$LuAlO_3(Ce)$], lanthanum bromide [$LaBr_3(Ce)$], and lanthanum chloride [$LaCl_3(Ce)$] [10].

Usually, for radiation detection, scintillators are coupled to light guides. They are thin pieces of crystal that are placed between the scintillator and the light sensor whose function is to increase the light collection efficiency. They diffuse the light from the scintillator improving its uniformity and homogeneity, spreading the photons as they arrive to the sensor and inducing that the majority of photons are properly detected: no photons are left from the gaps between photomultipliers [4].

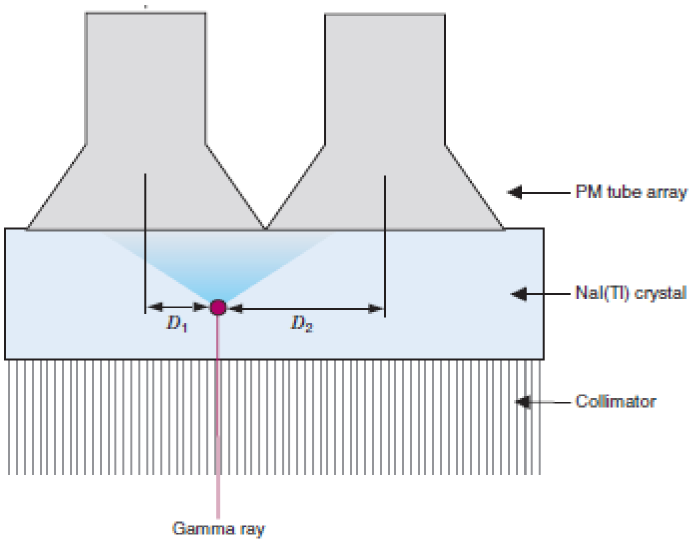

Figure 9: Illustration of the light spread produced by the light guide crystal [4]

One light guide property to consider is its refractive index. It needs to be such that the light diffraction goes in the proper direction in order to reach the PMTs.

1.3.2 PMT

A photomultiplier tube is a device that converts the extremely weak light signal consisting in no more than a few hundreds of photons from a scintillation pulse into a corresponding electrical current [11]. It is a vacuum tube consisting of an input window through which light passes, a photocathode where electrons are excited and then emitted, focusing electrodes that accelerates and focuses the photoelectrons onto the first dynode, an electron multiplier multiplies the photoelectrons by means of secondary electron emission, and finally an anode that receives and collects the multiplied secondary electrons from the las dynode [7].

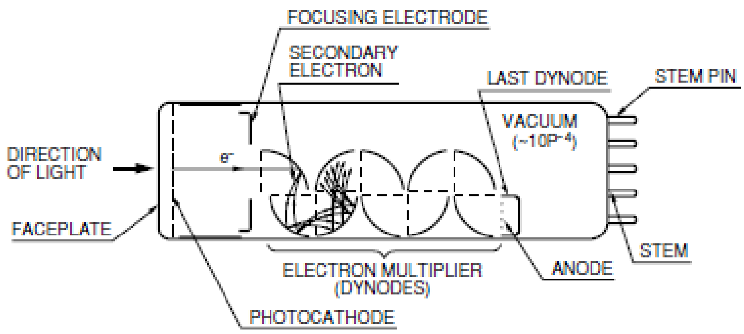

Figure 10: Schematic view of a photomultiplier tube [7]

As it has been previously described, PMTs work by external photoelectric effects. The first step performed by the PMT is the conversion of light photons into electrons. This process is performed by the photocathode and is called photoemission, consisting on three sequential steps: absorption of incident photons transferring energy to the electrons of the material, migration of excited electrons towards the surface of the photocathode and finally, if they absorb enough energy, their emission to the vacuum and later to the focusing electrodes. The unit that characterizes the performance of the photocathode is its *quantum efficiency* (QE), which is defined as

$$QE = \frac{number\ of\ photoelectrons\ emitted}{number\ of\ incident\ photons} \quad (2)$$

Ideally the QE should be 100%, but in the real world, photocathodes have quantum efficiencies of no more than 30%.

Bearing in mind that only a few hundreds of photons arrive to the faceplate and that the QE of the photocathode is very far from the ideal world, a huge gain is needed to measure reasonable quantities of current. Electron multipliers are composed of up to 19 dynodes with an electron gain on the order of 10^6. When an electron leaving the photocathode strikes the surface of a dynode, δ secondary electrons are produced. These resulting electrons have low energies, and by an electrostatic field they are guided to the next dynode until reaching the last one. The overall gain of the PMT would be $\alpha\delta^N$, where α is the fraction of photoelectrons reaching the electron multiplier, δ is the average secondary emission ratio and N the total number of dynode stages [11].

Finally, the anode receives and collects all the secondary electrons from the electron multiplier step and outputs the electron current to another circuit. In order to obtain a large output current, there must be an adequate potential difference between the last dynode and the anode [7].

1.3.3 Solid-state PM (Si photodiodes)

Besides PMTs, advances in the development of the semiconductor industry, especially in the field of photodiodes, have led to the improvement of radiation detectors introducing solid-state photomultipliers in some applications. The most common type of photodiodes used in PET are Silicon photomultipliers (SiPM) and there has been a shift in the last few years following a general trend to move from the vacuum based PMTs towards this new type of photodetector. Some of the advantages that silicone photodiodes offer over the conventional PM tubes are higher quantum efficiency, lower power consumption, more compact size and improved ruggedness [11]. They also provide features such as excellent linearity with respect to incident light, low noise, wide spectral response range and long life. Si photodiodes can be classified into PN type Si photodiode, Si avalanche photodiode (Si APD) and multi-pixel photon counter (MPPC), also known as SiPM.

1.3.3.1 Si photodiode (PN type)

Silicon PN is the most basic silicon photodetector. In **Figure 11** it can be seen how these devices are designed. The P-layer is located at the photosensitive surface and acts as the anode, whereas the N-layer is at the substrate and has the function of the cathode. Both together form the PN junction and operate as a photoelectric converter. The region located between the two layers is known as the depletion layer.

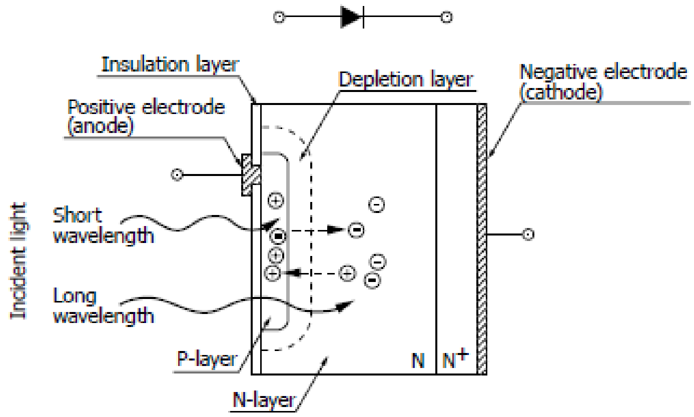

Figure 11: Schematic of Si photodiode [12]

If this photodetector is illuminated by a light with an energy higher than the band gap energy, the electrons of the valence band will be excited and emitted to the conduction band leaving holes in the valence band as it is represented in **Figure 12**. This process occurs throughout the three layers. The electric field accelerates these electrons toward the N-layer whereas the holes are accelerated toward the P-layer. Besides, electrons are diffused towards the N-layer conduction band resulting in a negative charge at this site, while holes diffuse towards the P-layer valence band resulting in a positive charge. If an electrode from an external circuit is connected to the P and N-layers, electrons will flow from the N-layer to the opposite electrode and holes will do the same from the P-layer, generating current. These electrons and holes are named carriers [12].

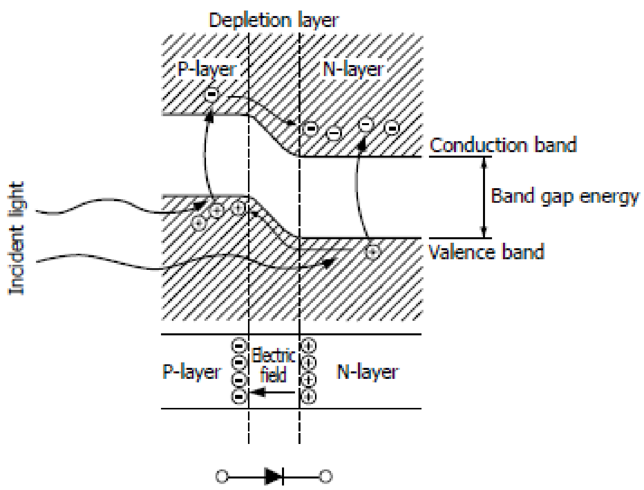

Figure 12: Si photodiode PN junction [12]

Si photodiodes are based on internal photoelectric effect, generating current due to the photovoltaic effect. These devices provide a very linear photocurrent with respect to incident light, especially for low levels in within the range of 10^{-12} to 10^{-2} W. The dark current can be defined as the small electric current that flows through photodiodes even when no photons are reaching the detector [13]. It is caused mainly by thermal noise, and it is almost linear in the range from -10 to 10 mV.

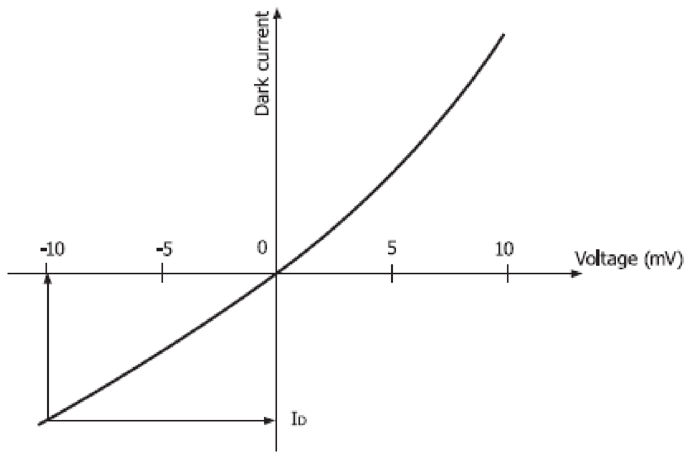

Figure 13: Dark current vs. voltage in a Si photodiode [12]

1.3.3.2 Si APD

Avalanche photodiodes are photodetectors that increase the small amount of charge produced by conventional photodiodes. These devices apply a reverse voltage in order to multiply low-level light signal into a large electrical current. Si APDs are used for short wavelengths of 400 nm and they can detect light from the UV to visible region with extremely low noise.

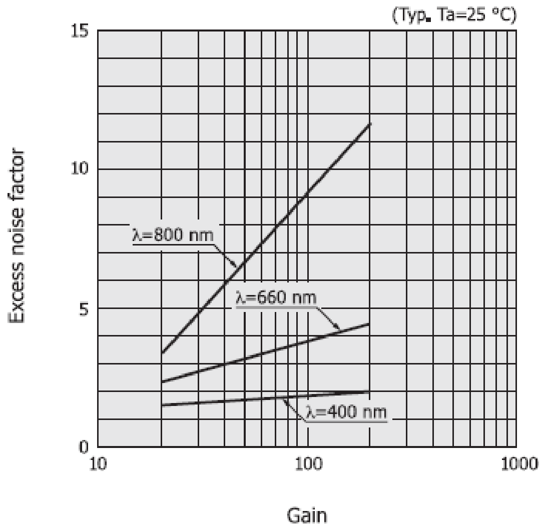

Figure 14: Excess noise factor vs. gain for a typical Si APD [14]

By increasing the reverse bias voltage across a PN junction, Si APDs intensify the electric field in the depletion layer increasing the electric force exerted on charge electron-hole pairs. The drift speed of these carriers is augmented, being more likely to collide with atoms in the crystal's lattice. There is a point where this speed is saturated and some carriers experience a huge increase in kinetic energy, favouring ionization whenever these particles collide with the crystal lattice. These carriers would create additional electron-hole pairs in a chain reaction process. That increase in carrier population is known as avalanche multiplication and is depicted in **Figure 15**.

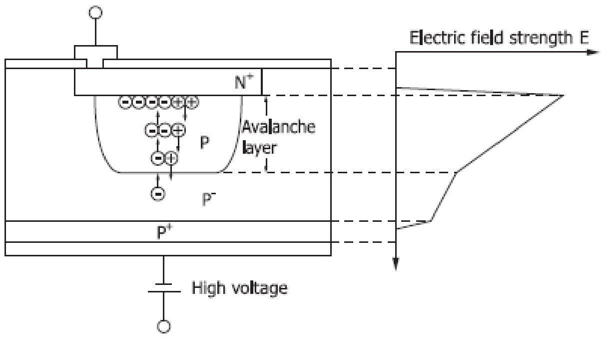

Figure 15: Schematic of avalanche multiplication [12]

The ionization produced by the collisions between these carriers and the crystal lattice determines the gain of the APD. This means that as the reverse voltage is increased, the gain increases until reaching the breakdown voltage. But the gain not only depends on the reverse voltage, it also depends on temperature. As it raises, crystal lattice vibrations increase and so does the possibility of a collision of the carriers and the lattice before reaching enough kinetic energy and making more difficult its ionization. Thus, the lower the temperature, the higher the ionization probability, and the higher the gain. It is important that the temperature is kept constant to obtain a constant output.

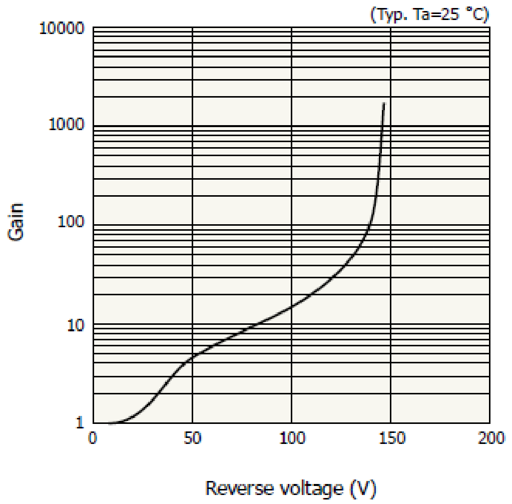

Figure 16: APD gain vs. reverse bias voltage [14]

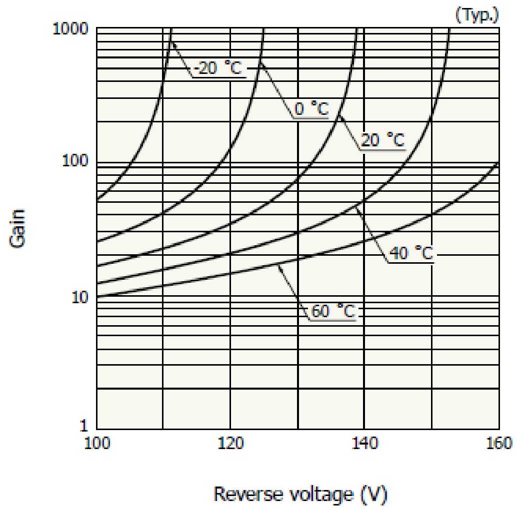

Figure 17: Effects of temperature on gain vs. reverse voltage [14]

Spectral response characteristics of avalanche photodiodes changes with respect normal photodiodes when a reverse voltage is applied. The penetration of light in the Si APD depends on wavelength. The shorter the wavelength, the shallower the depth light can reach, and the more carriers would be generated at the surface. The contrary effect occurs for longer wavelengths, where carriers are generated in the bulk. As for the phenomenon of avalanche multiplication to occur it is necessary that the carriers pass through the high electric field near the PN junction reaching the P layer, higher gains will be achieved for long wavelengths.

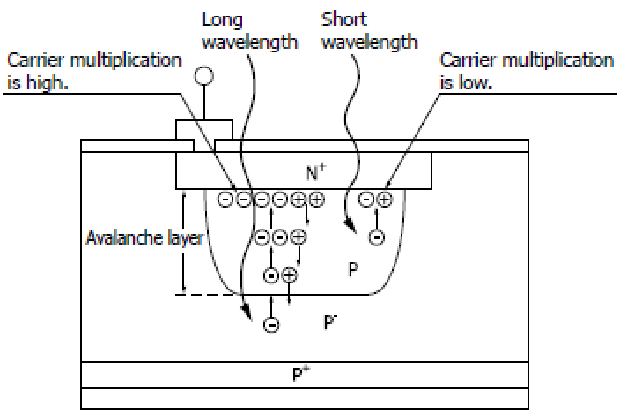

Figure 18: Absorption of short and long wavelengths in an APD [14]

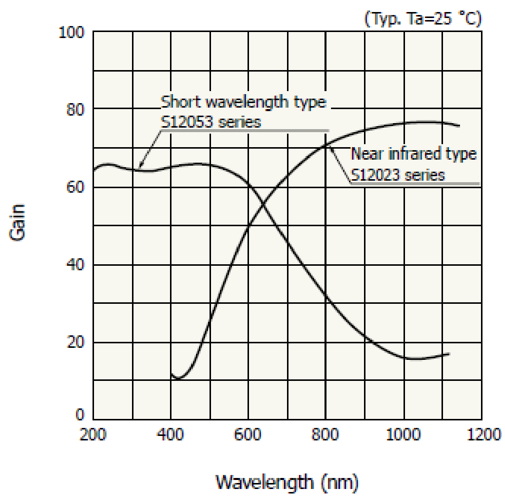

Figure 19: Gain vs. incident light wavelength for an APD [14]

1.3.3.2.1 Photon counting

Si APDs are mostly used for photon counting. This technique is based on the fact that a stream of light particles can fall to such a low level that the arriving photons can separated from each other. Avalanche photodiodes can detect very low light levels and even they can detect single photons if the reverse voltage is set higher than the breakdown voltage, obtaining a large gain. This condition is referred to as Geiger-mode operation.

During Geiger mode, a high electric field is produced even for weak light input, obtaining gains in the order of 10^5 or 10^6. Under this condition, when a carrier arrives to the avalanche layer, a very large pulse is generated, and constant output currents are obtained no matter the number of input photons. If a quenching resistor is connected to an APD and the reverse voltage is decreased below the breakdown voltage, the resistor resets the APD, as it saturates, and events can no longer be detected. Then, the number of photons is counted to measure light level.

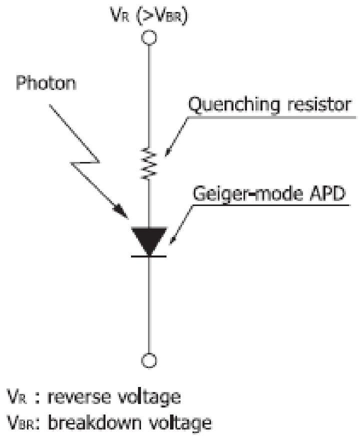

Figure 20: Geiger mode APD and a quenching resistor [12]

1.3.3.3 SiPM or MPPC

A Silicon photomultiplier (SiPM), also known as multi-pixel photon counter (MPPC), is a type of photon-counting device that use several APD pixels operating in Geiger mode fabricated on a monolithic silicon crystal. SiPMs offer features such as excellent photon counting capability, low voltage operation, high gain up to 10^5 or 10^6, excellent time resolution and uniformity, good spectral response for scintillators, small dimensions, simple readout circuit operation and they are immune to magnetic fields. These devices combine several APDs operating at Geiger mode and quenching resistors connected in parallel as it is shown in the following figure:

.

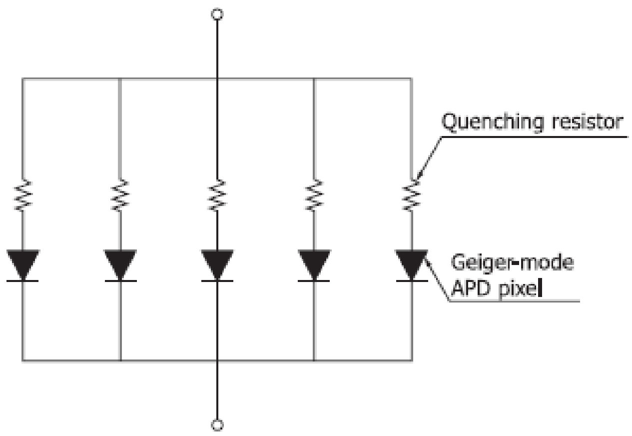

Figure 21: SiPM equivalent circuit [12]

Figure 22 represents the actual appearance of a MPPC array.

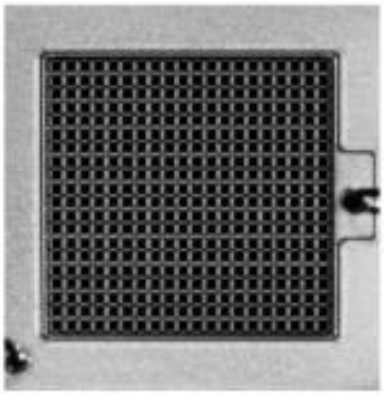
Figure 22: Actual matrix implementation of MPPC microcells [14]

Each of the avalanche photodiodes detects a single photon and only provide information on whether it has entered or not. It does not matter the number of photons reaching each individual APD, the output will be constant. As a MPPC is a combination of APDs, the final output will be number of APDs that detected at least one photon. Since the quenching resistor is in series with each of the APDs, it allows their output currents to flow through it. The final output of the system is a large pulse created by the overlapping of the output pulses from each single APD pixel. The number of photons reaching the SiPM detector can be estimated by calculating the charge of the final pulse as in equation (3) :

$$Q_{out} = C \times (V_R - V_{BR}) \times N_{fired} \quad (3)$$

where Q_{out} is the electric charge of the pulse, C the capacitance of the APD pixel, V_R and V_{BR} the reverse and breakdown voltages respectively and N_{fired} the total number of APDs that have detected photons.

If the MPPC is coupled to an amplifier, sharp pulse waveforms can be visualized when connected to an oscilloscope. The height of each wave will depend on the number of photons detected by the device, as it is represented in **Figure 23** [12].

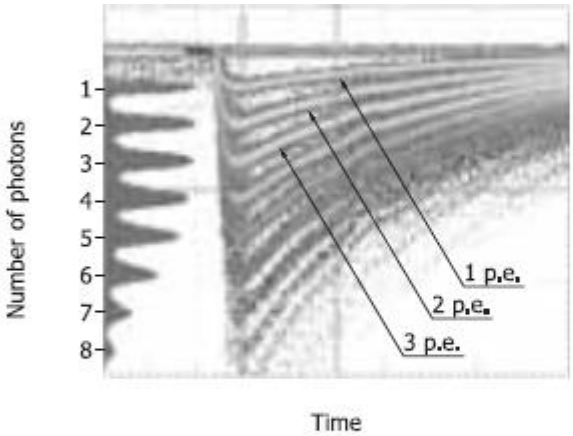

Figure 23: Pulse waveforms depending on the number of photons detected [12]

As it has been commented, one of the most important features on the MPPC is its gain. It is the factor by which the APDs in Geiger mode multiplies the charge of the starting electron ($q = 1.6 \times 10^{-19}\ C$) to obtain a large output charge of the SiPM. Bearing in mind equation (3), the gain is proportional to overvoltage ($V_R - V_{BR}$) and it varies with the reverse voltage. The final output needs to be processed by a PC in order to obtain a digitized frequency distribution for that charge [14].

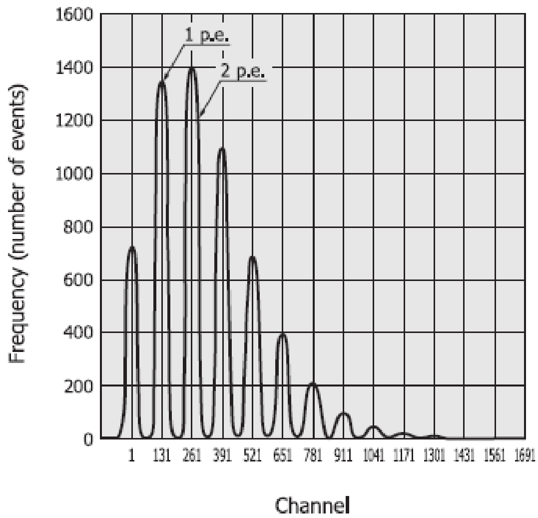

Figure 24: Frequency distribution vs. number of detected photons [12]

Figure 24 represents the amount of output charge of the SiPM. As we move to the right in the abscissa coordinate, the output charge increases. The Y axis represents the number of events at each of the output charges while the number of photon equivalents (p.e.) is represented by each of the peaks. The output charge of one detected photon is equal to the distance between peaks, so the gain can be finally expressed as:

$$Gain = \frac{\#\ of\ channels\ between\ peaks\ \times ADC\ rate}{q} \qquad (\ 4\ )$$

where q is the electron charge and the ADC rate are the electric charge per channel. This gain is characterized by their excellent linearity.

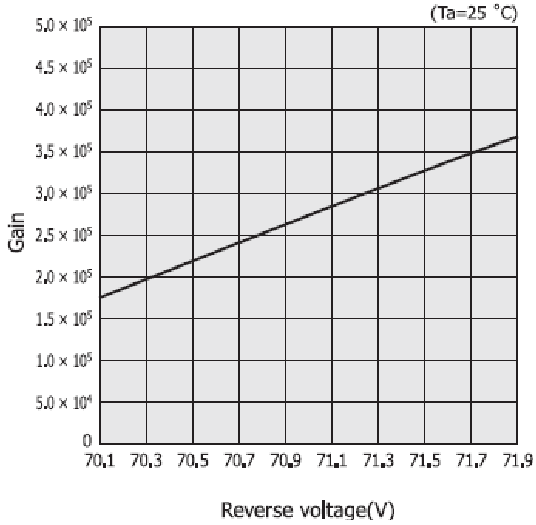

Figure 25: Gain vs. reverse voltage [12]

As it was explained in **Figure 17**, the APD gain is dependent on temperature, being higher for lower temperatures and dropping as temperature raises (vibrations on the lattice are stronger and carriers strike de crystal before acquiring enough kinetic energy, making more difficult ionization). Since a Si photomultiplier is a set of APDs, they share the same principle: the MPPC's gain depends on temperature. For a fixed reverse voltage, the gain will lower as temperature is increased (**Figure 26**), so it is highly recommended to operate MPPCs at constant lower temperature. In the case that temperature varies, the reverse voltage should be adjusted in order to obtain a stable output as it is shown in **Figure 27**.

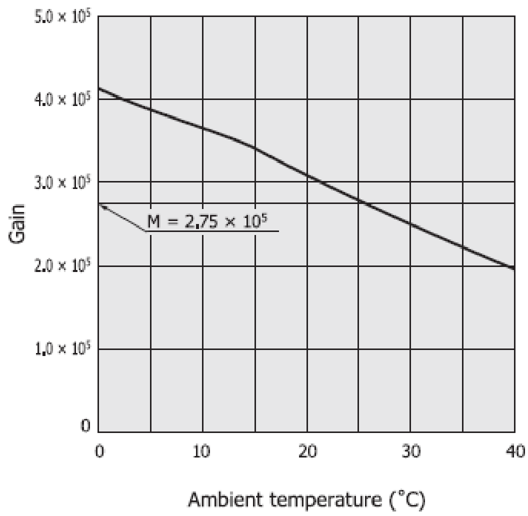

Figure 26: Gain vs. ambient temperature for a given reverse voltage [12]

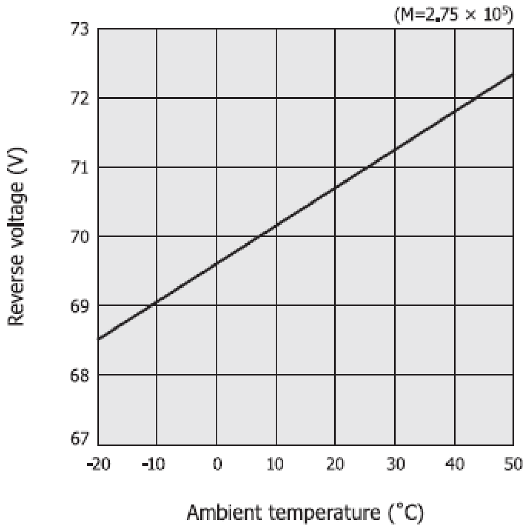

Figure 27: Reverse voltage vs. temperature to maintain constant the gain [12]

1.3.3.3.1 Noise in SiPM

There are three main sources of noise that may alter the efficiency of the MPPC: crosstalk, afterpulses and dark counts.

Optical crosstalk is a phenomenon that occurs when a primary avalanche in an APD triggers secondary discharges in adjacent APDs inside the MPPC. Some of the charged carriers inside a single APD may transmit their energy through scatter collisions as heat and emitting photons. These photons can travel to neighbour APDs initiating Geiger avalanches in them. If the avalanche occurs simultaneously, it is called prompt crosstalk, whereas if it is delayed in time, it is a delayed crosstalk.

If these thermal carriers get trapped in some impurity energy level and they are released after short delays after receiving the needed energy to reenter either the conduction or valence band, they may initiate new avalanches which are referred as **afterpulses**.

These phenomena are examples of correlated noise due to thermal generation of a carrier, and they must be corrected in order not to have higher signals than the ones implied by the amount of incident light [14][15].

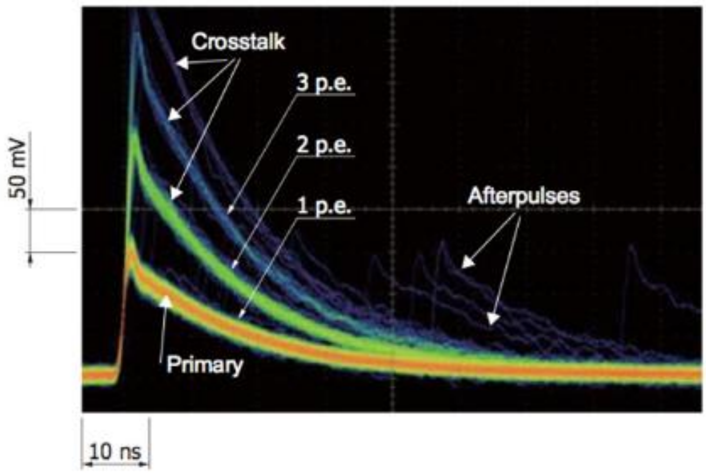

Figure 28: Types of noise due to thermal generation of a carrier [15]

The SiPM is a solid-state device, so it works under the same principles as Si photodiodes. A small current flows through this instrument due to thermal excitation even when no photons are detected: the dark current. Since MPPCs have a huge gain due to Geiger avalanche, this dark current is also amplified, giving as result **dark pulses**. This quantity is measured as counts per second (cps), and it is a key parameter in determining how good is the device. As dark counts increase with the gain, they will also depend on temperature and reverse voltage (**Figure 29** and **Figure 30**).

It is very difficult to distinguish one dark pulse from the pulse obtained when one photon arrives to the detector, since both outputs are pulses of 1 photon equivalent (p.e.). Nevertheless, dark pulses greater than 1 p.e. are very unlikely detected, so by setting a proper threshold (usually 1.5 p.e.), they can be eliminated.

In order to measure the dark counts, the detector is set in dark conditions with no incident photons under a threshold of 0.5 p.e. To evaluate crosstalk, the threshold can be set to 1.5 p.e. [12].

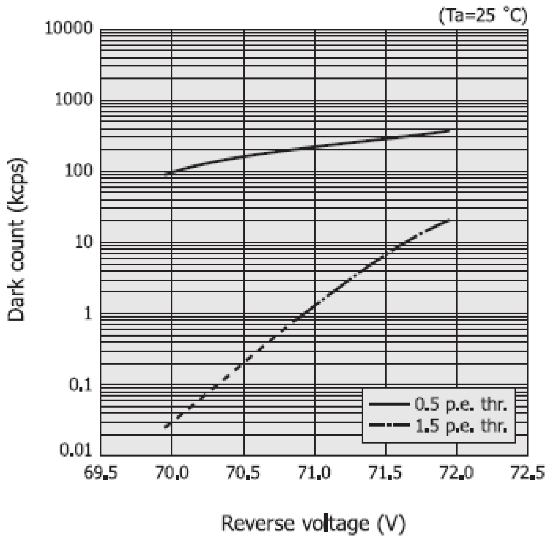

Figure 29: Dark count vs. reverse voltage [12]

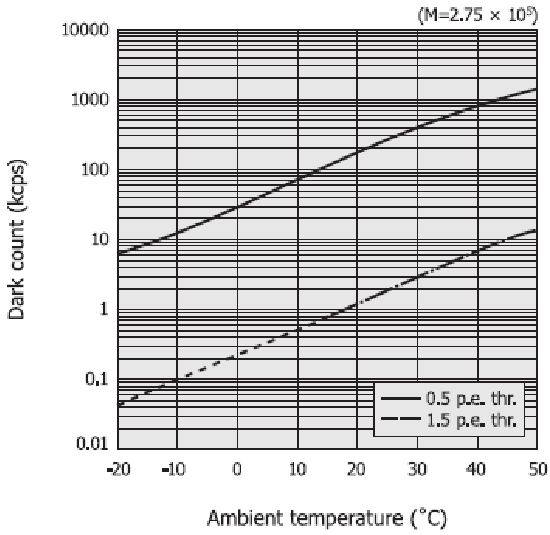

Figure 30: Dark count vs. ambient temperature [12]

In applications where several photons are detected per light event, if the threshold is increased, the dark count rate can be excluded from the readout [14].

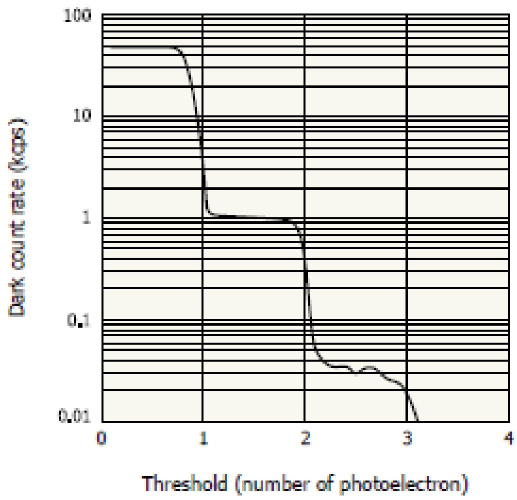

Figure 31: DCR vs. counting discriminator threshold level [14]

1.3.3.3.2 Photon detection efficiency, dynamic range and time resolution

Apart from dark count rate, some other SiPM characteristics depend on temperature, as it is the case of photon detection efficiency (PDE). It is a measure of the percentage of incident photons detected (e.g. the probability that the detector produces an output signal in response to an incident photon) and it can be calculated as the product between the quantum efficiency (QE), the MPPC pixel fill-factor (effective pixel area / total pixel area) and the Geiger mode avalanche probability (# of excited pixels / # of photon-incident pixels).

$$PDE = QE \times Fg \times Pa \quad (5)$$

SiPM reaches the maximum PDE at around 440 nm, which matches the emission wavelength of LSO scintillators. This is the reason why this type of scintillators is the most used with MPPC detectors [12] [14].

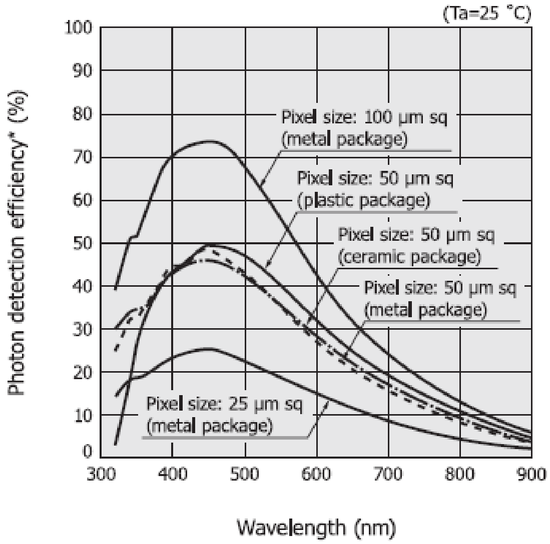

Figure 32: PDE vs. Wavelength [12]

The dynamic range of the incident photons is determined by the PDE and the total number of pixels of the SiPM. Since the output of each pixel is the same regardless the number of photons that it has detected, the linearity reaches a plateau when the number of incident photon is relatively large with respect to the number of pixels. It is described in equation *(6)*:

$$N_{fired} = N_{total} \times (1 - e^{-\frac{N_{photon} \times PDE}{N_{total}}}) \quad (6)$$

where Nfired is the number of excited pixels, Ntotal is the total number of pixels, and Nphoton is the number of incident photons.

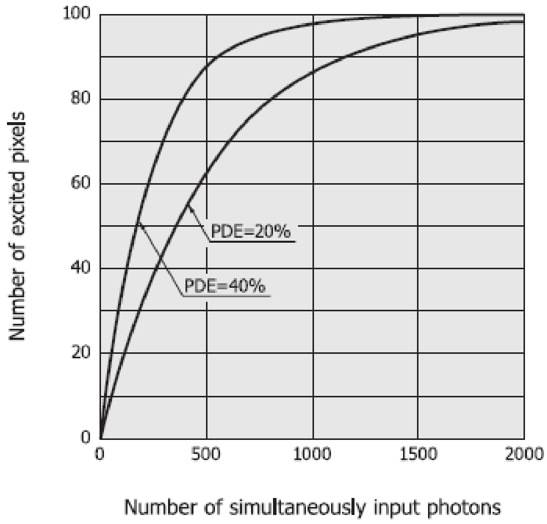

Figure 33: Number of excited pixels vs. number of simultaneously input photons [12]

After a certain period of time, the pixels become able to detect photons again. This is called recovery time and it lasts approximately 20 ns until the pixel is completely restored [12].

Finally, the time resolution can be defined as the shortest difference of time existing between a detected event and another one. This time resolution is determined by several factors:

$$\sigma_{OveralTiming} = \sqrt{\sigma^2_{PulseTiming} + \sigma^2_{TimeStamping} + \sigma^2_{DetectorJitter}} \quad (7)$$

where pulse timing correspond to the detection time of the output pulse, time stamping is the time that lasts the system in recording the signal once it has met the trigger requirements, and detector jitter is defined as the limiting factor of the overall time resolution of a photodetector, caused by the detection system alone [14].

The time resolution is usually described as the full width half maximum (FWHM) of the signal:

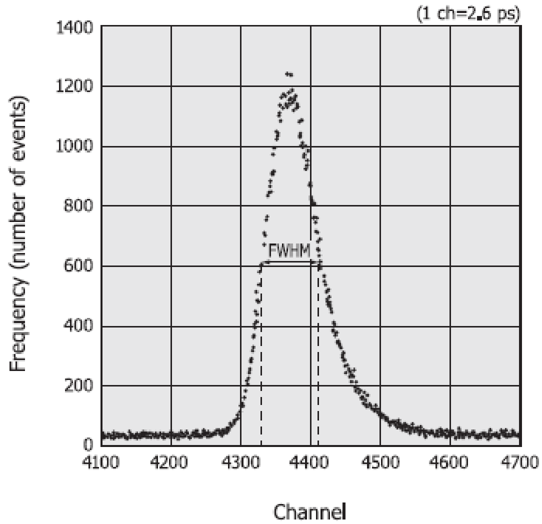

Figure 34: Pulse response distribution [12]

where the channel corresponds to the height of the pulse and is proportional to its energy [12].

1.3.3.3.3 Digital SiPM

The last generation of photodetectors for photon counting corresponds to the new digital SiPM (dSiPM). While analog SiPMs work summing all cell outputs leading to an analog output signal with limited performance, dSiPM include digital readout electronics where each diode is a digital switch and whose digital output is the sum of all detected photons and a time stamp. Since the main function of dSiPM detectors is to count the total number of photons arriving, they are termed digital photon counters (DPC) [16] [17].

dSiPM sensors are based on a single photon avalanche photodiode (SPAD), integrated in a CMOS process (complementary metal-oxide-semiconductor), one of the most used logic families implemented in integrated circuits, favouring low power consumption and adding possible integration of data post-processing. The main difference between the APD and the SPAD is that the former is a linear amplifier with limited gain that operates at a bias lesser than the breakdown voltage, while the latter is a trigger device (the gain concept is meaningless) specifically designed to operate with a reverse bias voltage well above the breakdown voltage.

In these devices, each SPAD has its own read-out circuit, and next to each of them there is integrated a one-bit memory switch with the purpose of enabling or disabling the diode. Each SPAD together with its matching electronics correspond to a single cell, which is connected to the TDC (time-to-digital converter). Each cell is connected to the photon counters to determine the total number of photons reaching it, by a synchronous bus. This number is proportional to the total energy of the pulse. Additionally, a small bias voltage generation can be integrated in the detector together with a feedback control loop in order to adapt it to the actual value of the breakdown voltage. In this way, the sensor will be oblivious to temperature drifts.

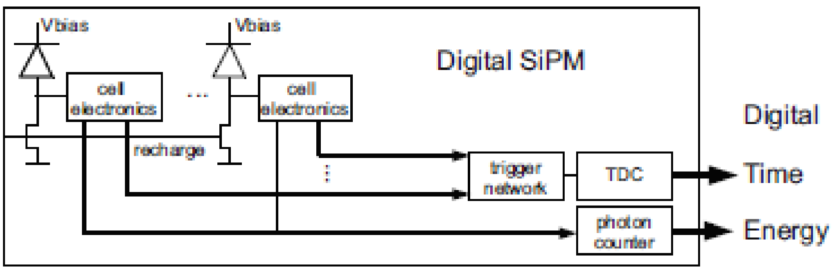

Figure 35: Photodetector based on digital silicon photomultiplier [17]

Figure 36 shows the actual appearance of a digital SiPM chip.

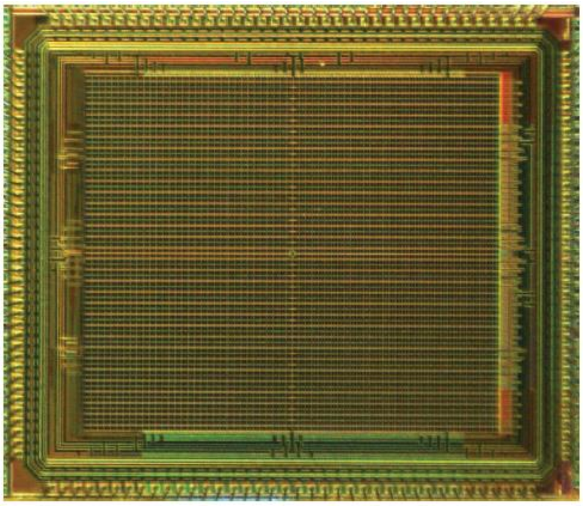

Figure 36: Microphotograph of the test chip [17]

Unlike analog SiPM, the cells that compose dSiPM are able to detect and store only one photon. Once it is detected, a transistor is used to quench the avalanche and another one to reset the diode to its initial sensitive stage.

Two signals are provided by each cell: the trigger signal and the data output signal. The first one is connected to a trigger network which is at the same time connected to the TDC. Different triggers can be chosen depending on the desired level of selectivity. With lower triggers it is more probable that a dark count reaches the threshold and it can be considered as an event, but increasing the trigger level, dark counts are recognized, and diodes are reset. All cells in a column are connected to the same data line and the data output signal is applied to that line using a row enable signal. The acquired data can be read out row by row.

Finally, to improve the efficiency of the dSiPM detector, a dark count map (DCM) can be obtained. To perform this DCM, it is necessary to enable each cell separately setting the trigger level to the first photon trigger, count the total number of triggers in a second to obtain the dark count rate and repeat the process successively for each diode in the pixel. If the diodes that contribute to the dark count rate are switched off, the total dark count rate will be reduced, and the system will be improved [17].

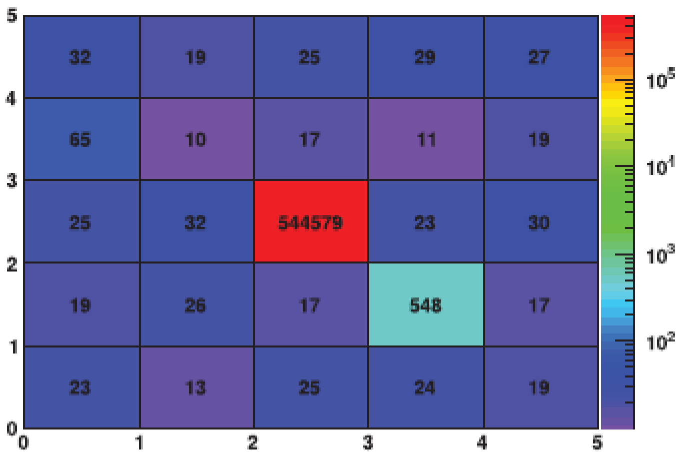

Figure 37: Dark count map of a dSiPM [17]

Figure 38 shows the operating principle of a digital photon counter. The arrival time of the first photon sets the beginning of the time interval of the event, and once this period of time ends, the total amount of photons counted is converted into a digital number, proportional to that quantity and also to the total energy of the scintillation gamma photon [18].

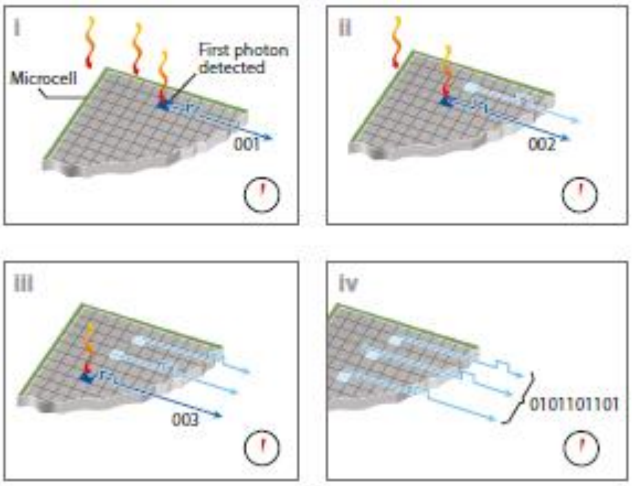

Figure 38: Actual functioning of digital photon counters [18]

Until now, only Philips is working with this type of detectors. They designed the Philips Digital Photon Counting (PDPC), which implements in its sensors dSiPM technology. Today, they are employing these PDPCs in Vereos, the first digital PET/CT of the world, redefining image acquisition with PET, discovering smaller injuries, in a faster way and using less radiotracer concentrations [19].

1.4 STATE-OF-THE-ART

1.4.1 Hyperion II^D, PDPC based small animal PET/MR

In biomedical research, before the clinical application of a treatment, most of the times there is a preclinical phase in which it is tested with animals. The Hyperion II^D PET is a scanner composed of 20 PDPC stack detectors for PET/MR small animal imaging. This system combines the anatomical information provided by MRI with the functional in-vivo imaging provided by PET. The energy resolution achieved with this scanner is 12.7% and the coincidence resolution time is 609 ps. The PET ring has a diameter of 209.6 mm between the opposing detectors, so animals as big as a rabbit can be tested with this system. The MRI transmit/receive coil is inserted into the PET gantry [20]. More details about PET/MR will be discussed in section 1.4.4.

Figure 39 represents an illustration of Hyperion IID system, and **Figure 40,** an image obtained with it.

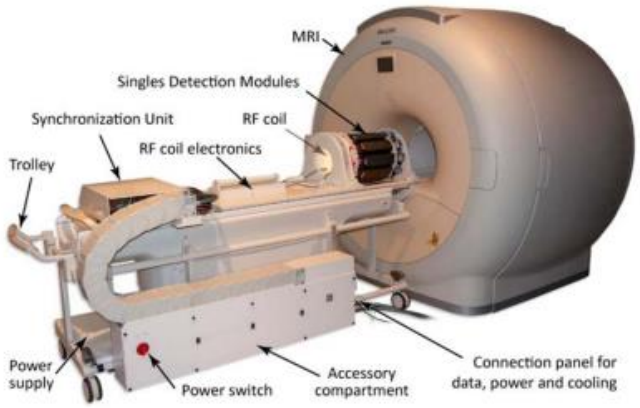

Figure 39: Hyperion II^D PET /MR system [20]

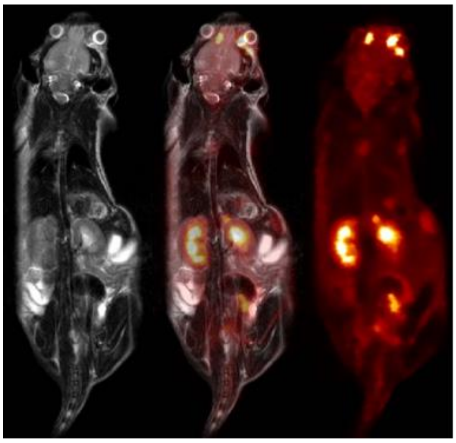

Figure 40: Coronal views of in-vivo mouse scans using Hyperion II^D system [20]

1.4.2 PhenoPET, PDPC based plant research PET

Apart from animals, this type of technology has also been tested with plants. PhenoPET is a PDPC based PET system, being the first one dedicated to plant research. It uses $^{11}CO_2$ as a radiotracer to study the carbon transport of the plant. This system was the smaller scanner employing time-of-flight information. The reason of the use of PDPCs as photodetectors is the need of a fast timing and high data rates, as ^{11}C is a short living isotope. The system consists of three detector rings with a 25.5 cm diameter and a FOV of 18 cm diameter and 20 cm axial height [21].

Figure 41 represents the PhenoPET system, while **Figure 42** represents a green bean plant image obtained with this technology.

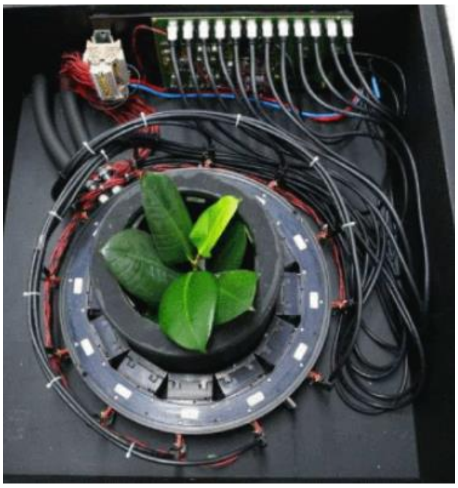

Figure 41: PhenoPET system with a plant introduced [21]

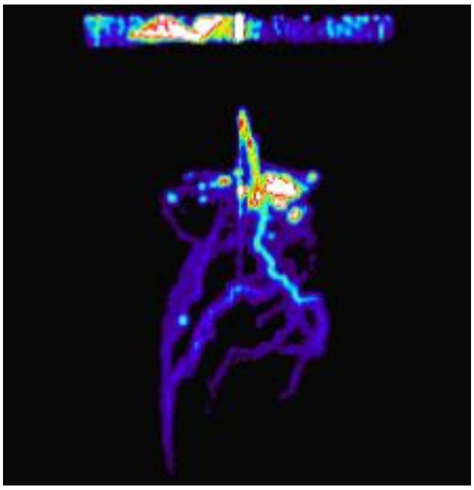

Figure 42: Image of the roots of a green bean plant acquired with the PhenoPET system [22]

1.4.3 VEREOS, PDPC based TOF PET scanner

As it has been said, the state-of-the-art technology related to PET imaging is the one implemented by Philips in Vereos PET/CT, the first and only commercial digital PET system including the aforementioned PDPCs. This technology is constituted by a ring of detectors coupled 1 to 1 to each scintillator, offering a high level of performance due to its time-of-flight technology and its time resolution of 325 ps (the fastest in the market). The achieved energy resolution is 11.1 % [23]. The proven capabilities of this multimodal imaging system allow for detectability and characterization of smaller injuries. This scanner improves image quality requiring only half of the standard radiotracer dose and allows for uncompromised lesion detectability at one tenth of the time. By fusing the structural image obtained by the CT and the functional information from PET, Vereos PET/CT is a powerful diagnosis tool [24] [25].

In **Figure 43,** an illustration of this system is shown, while in **Figure 44**, a comparative of an image obtained using analog PET systems and Vereos PET/CT can be seen.

Figure 43: Philips Vereos PET/CT system [19]

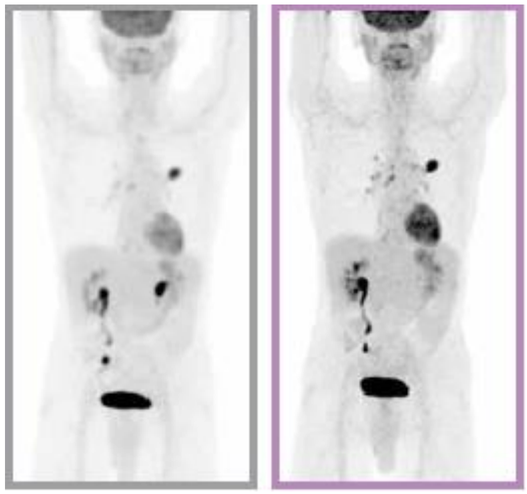

Figure 44: Image acquired with an analog PET scan (left) and with digital Vereos system (right) [25]

1.4.4 PET/MR scanner

Although PET/CT is the most used combination, there are other alternatives such as PET/MR imaging. The development of this multimodal system has been slower due to technical challenges when combining both modalities. It is obvious that the structural information provided by MRI is better than that of CT, especially in soft tissue, so one may think that this combination provides better results than the former one. Furthermore, PET/MR provides truly simultaneous imaging, unlike PET/CT. Most of the PET/MR scanners developed so far are meant for preclinical image and are mainly used for research. Although it is a very promising technology, two main challenges have slowed its development: attenuation correction and PET calibration. In PET/CT systems, the attenuation correction is easy to obtain, as they both are affected by the same processes when talking about photon scattering, while for MRI the complexity highly increases.

PET calibration is also simple for these systems, as is can be achieved by implementing water-filled phantoms, but in MRI they show artefacts and inhomogeneities [18].

The first whole-body PET/MR clinical scanner is the Siemens Biograph mMR, which still used APD technologies instead of SiPM. The GE Healthcare was the first in replacing APDs by SiPM in PET/MR commercial systems, increasing the gain, the rise time and decreasing the supply voltage. Digital SiPMs (specifically PDPCs) were first implemented in PET/MR preclinical devices in 2012, improving the energy resolution to 11.4% and the 3D spatial resolution to 0.73 mm FWHM. Apart from whole-body systems, organ specific PET/MRs have also been developed, being the brain the target to which more research groups have focused. One example is INSERT, focusing in breast system and having an energy resolution of 14%. The most recently project is Horizon 2020 (HYPMED), which have been funded to build a PET/MR breast insert [26].

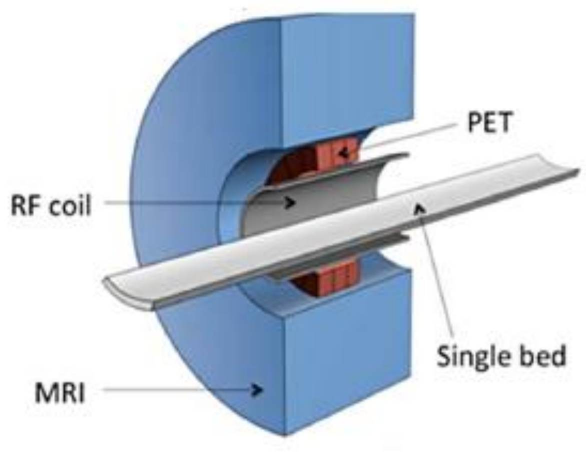

Figure 45: Schematic of a PET/MR system [26]

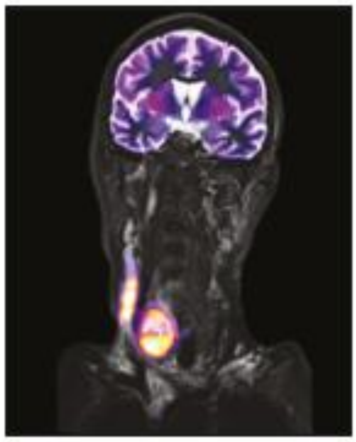

Figure 46: Coronal slice combining PET/MR technology [18]

1.4.5 Total-body PET

Until now, the most advanced PET system is the EXPLORER total-body PET scanner. It has a 194-cm axial and 68.6-cm transaxial fields of view that allows it to cover the entire human body in a single acquisition. It is also possible to perform total-body pharmacokinetic studies with frame durations of one second. This scanner is composed of 8 axial units, each with an axial field of 24 cm and with 2.5 mm gaps between units. Due to its large size, the signal-to-noise ratio is highly improved, allowing for higher quality images. Since the sensitivity is also increased, PET images with very small amounts of activity can be acquired, what will decrease the potential damage from ionising radiation. It has a coincidence time resolution of 430 ps, enabling it to use ToF, and an energy resolution of 11.7%.

The idea of developing this type of total-body PET scanners has been studied for many years, and finally Simon Cherry and his research group achieved its implementation publishing the first result in November 17th, 2018. The potential benefits of this system are based on 5 primary claims: image better, faster, lower dose, dynamic images and high temporal resolution [27].

Figure 47: Photograph of EXPLORER total-body PET/CT [27]

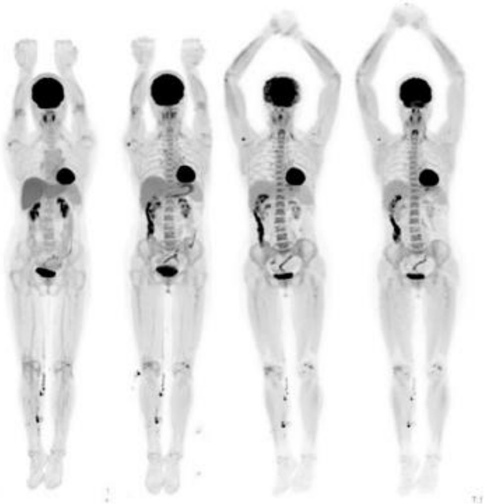

Figure 48: Total-body images obtained using EXPLORER [27]

1.4.6 New scintillator materials

In the last years, not only new photodetectors have been developed, but also new scintillators. Since 1990's, the demand for higher performance scintillators has dramatically increased to a point where it is possible to design scintillators for specific purposes, adjusting the energy levels and other features. Regarding PET, the challenge is to improve the SNR in order to reduce the concentration and activity of the radiotracer, so the main points to achieve are improving the sensitivity and the spatial, energy and temporal resolutions. To do so, the scintillator materials have to be chosen to have a good stopping power and conversion efficiency. At the end of the nineties, BGO crystal arrays was the first choice, providing high density (7.1 g/cm^3) and a very high atomic number (75) resulting in a efficient photoelectric conversion. The main counter was related the slow decay time (300 ns) of the scintillating light. Then in the 2000's, a new, 10 times faster scintillators appeared applying phoswich technology: Cerium doped Lutetium ortho-silicate (LSO). The gain in sensitivity increased about one order of magnitude and in spatial resolution it doubled. Now, innovating crystals of the family of Lutetium perovskites (LuAP) are being produced industrially. They have properties complementary to those of LSO and can be combined, with a density of 8.34 g/cm^3 and a time response of 17 ns, twenty times faster than BGO. Their response as a function of energy is much more linear, resulting in a better energy resolution. Finally, Cerium doped Gadolinum ortho-silicate (GSO) has been developed. The decay time dependent on Cerium concentration make possible to combine two different varieties or also with LSO to determine the depth of gamma ray interaction [28].

Scintillator	Type	Density (g/cm^3)	Light yield (Ph/MeV)	Emission wavelength (nm)	Decay time (ns)	Hygroscopic
NaI:Tl	Crystal	3.67	38,000	415	230	Yes
CsI:Tl	Crystal	4.51	**54,000**	550	1000	Slightly
BGO	Crystal	**7.13**	9000	480	300	No
GSO:Ce	Crystal	6.7	12,500	440	60	No
LSO:Ce	Crystal	**7.4**	**27,000**	420	**40**	No
LuAP:Ce	Crystal	**8.34**	10,000	365	**17**	No
$LaBr_3$:Ce	Crystal	5.29	**61,000**	358	35	Very

Table 1: Characteristics of the state-of-the-art scintillators [28]

1.5 Regulatory framework

As this project involves the manipulation of radioactive sources, it is important to consider the regulation that exists in Spain about ionizing radiation.

The Nuclear Safety Council (Consejo de Seguridad Nuclear: CSN) is the only competent body in Spain in this matter. It is the responsible for proposing to the Government the necessary regulations on nuclear safety and radiation protection. In addition, it adapts the national legislation to the international one, especially the one derived from the directives of the European Union.

The regulation of nuclear safety is based, fundamentally, on the practical application of the principle of defense in depth, which consists of the interposition of a set of physical and administrative barriers against potential radiological risks. Its regulation is also aimed to the prevention of incidents and the mitigation of their consequence.

In order to achieve and maintain an adequate level of nuclear safety, the CSN also requires the availability of qualified personnel, an adequate approach to physical security and the establishment of an effective safety culture.

Apart from nuclear safety, the damage that the misuse of artificial ionizing radiation can produce in health has given rise to the discipline called radiological protection. Its purpose is the protection of people and the environment against the harmful effects that may result from exposure to ionizing radiation.

Since 1928 there is an independent international body, the International Commission on Radiological Protection (ICRP), which issues recommendations and provides advice on all aspects related to protection against this type of radiation. These recommendations are the basis for the establishment of regulations and regulations by international organizations and regional and national authorities.

The three basic principles on which the recommendations of the ICRP are based are the following:

- Justification

  The practice involving exposure to ionizing radiation should always be a benefit to society. Negative effects and possible alternatives should be considered.

- Optimization or "ALARA Principle"

The term ALARA corresponds to the acronym of the expression "as low as reasonably achievable". All radiation exposures should be maintained at levels as low as reasonably possible, considering social and economic factors.

- Dose limitation

The radiation doses received by people must not exceed the limits established in the current legislation [29].

There are another three basic principles for radiation protection that can be applicable in the development of this project:

- Shielding

The ionizing radiation emitted by the radioactive source cannot penetrate lead, so shielding this source with lead prevents from radiation.

- Timing

The less the time, the lower the dose, so it is tried to stay the less time possible near the radioactive source.

- Distance

The bigger the distance, the lower the dose, as the intensity of the gamma-ray decays with distance. It was tried to maintain the maximum distance possible.

There exist special radioactive sources with low activity which students may use, as the one used in this project.

2 MOTIVATION AND OBJECTIVES

Cancer can be defined as a collection of related diseases in which some of the cells in the body start dividing without control and spread into surrounding tissues. These cells may divide without stopping and can end up forming masses of tissue called tumours. If these tumours are malignant, they will continue spreading and some of their cells may detach and travel to different tissues or systems through blood or the lymph system forming new tumours [30].

Nowadays, cancer is the second leading cause of death all over the world. It is estimated that in 2018 around 9.6 million of deaths were caused by this disease. Approximately 70% of these deaths occurred in underdeveloped regions including Central America, Africa and Asia. The number of new cancer cases is projected to increase to about 23.6 million by 2030. In 2017, only 26% of these underdeveloped countries reported they had treatment services in the public sector, what means that only one in five low income countries have enough resources to diagnose and fight against cancer. An early diagnosis and treatment are fundamental in order to reduce cancer mortality, since at late stages of this disease, curative treatment may not be an option [31] [32].

Nuclear medicine techniques such as PET are one of the leading imaging tools in medicine that contribute to the diagnosis and evaluation of cancer, providing information non-invasively about the location, size, spreading and a possible metastasis of the tumour. For this type of diagnosis, the radiotracer 2-deoxy-2-[fluorine-18] fluoro-D-glucose (^{18}F-FDG), an analogue of glucose, is used. It provides functional information about the increased glucose uptake of cancer cells in some tumours. These studies are repeated clinically with low radiation to have a continuous monitoring of the patient with results directly correlated with laboratory data [33] [34].

Figure 49: Axial image of a patient injected with 18F-FDG [34]

Nuclear medicine has gone from using the old PMTs to the new and improved dSiPMs. There is still much ground to cover in this branch of medicine. Thanks to the new technologies, the entire world is advancing from analogue to digital, and PET detectors are following the same trend. Digital photodetectors feature high imaging performance, improving the spatial and time resolution. The study these digital SiPMs and their use on nuclear medicine, can improve the early detection of cancer with optimum conditions and decreasing the deaths caused by this disease.

The main motivation of this project is to characterize this type of digital SiPM detectors. If we obtain good results, we could consider their use for small-animal PET imaging in a near future. Until now, our group have used analog SiPM detectors, and by replacing them by digital ones, we could improve our results in terms of time, spatial and energy resolution.

This work focuses on the use of the Philips Digital Photon Counting (PDPC) as a radiation detector for PET scanners. It is the first digital SiPM detector for PET imaging manufactured by Philips. It will be carefully studied and characterized. The specific objectives of this work are as follows

- Determine the optimal configuration of the acquisition parameters used by the PDPC
- Acquire a clean energy spectrum using a ^{22}Na radiation source
- Generate a flood field image using the PDPC with a pixelated scintillator array
- Develop and evaluate different event positioning algorithms
- Propose an optimal detector configuration that can be used to obtain high quality flood field images

3 MATERIALS

3.1 Philips Digital Photon Counting (PDPC)

The Philips Digital Photon Counting is a solid-state silicon photomultiplier (SiPM) digital photon counting (DPC). It is a trigger device whose only function is to count the number of incoming photons, so the gain concept is meaningless. All investigations are based on the Technology Evaluation Kit (TEK), a set of evaluation boards provided by the PDPC. In this work, the second version of these detectors is used (DLS 3200-22), including fewer and larger SPADs. It is composed of 3200 cells per pixel, with 78% area efficiency and a PDE higher than 30% using light sources of 430 nm.

The PDPC-Module-TEK provides two DLS 3200-22 detectors, one laptop, a programmable power supply, a base unit and all the needed cables to connect each module.

Figure 50: Image showing the laptop, power supply and base unit of the PDPC-module-TEK [35]

3.1.1 Detector structure

Each of the two detectors (DPC3200-22-44M22) is composed of 4 tiles of 16 sensor dies each, attached to a printed circuit board (PCB). The die sensor performs the actual data acquisition and photon counting autonomously. In turn, it is composed of 4 pixels containing the SPAD cells, which deliver the output photon count, and a TDC to generate the timestamp. This sensor contains 3200 cells per pixel, and since each of them can only detect one single photon per acquisition, the maximum number of detectable photons between two cell recharges is 3200 per pixel. Pixels are further divided into four sub-pixels, which are used to configure the different trigger schemes.

One single bias voltage supply is needed, as all dies in the sensor can be adjusted to have the same breakdown voltage. At the back of each tile, there is located a FPGA that configures and synchronizes each sensor die. It is responsible for the data post-processing, the timestamp calculation and different corrections. Together with the FPGA, the tile contains a flash memory chip used to able or disable individual cells on the sensor dies and a temperature sensor to adjust the bias voltage to the current temperature.

In **Figure 51** and **Figure 52,** the architecture of a tile and a die sensor are represented.

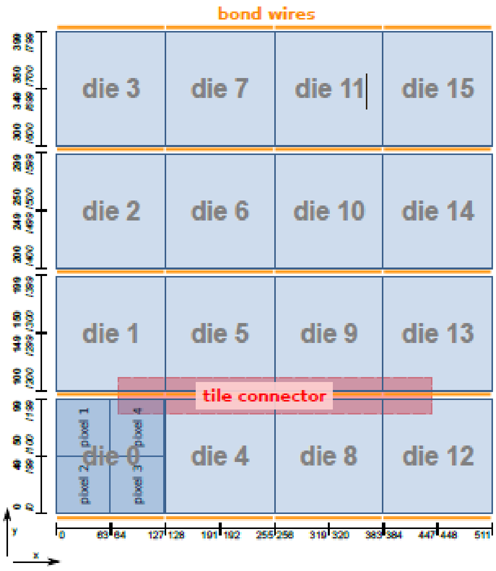

Figure 51: DPC3200-22 tile layout [35]

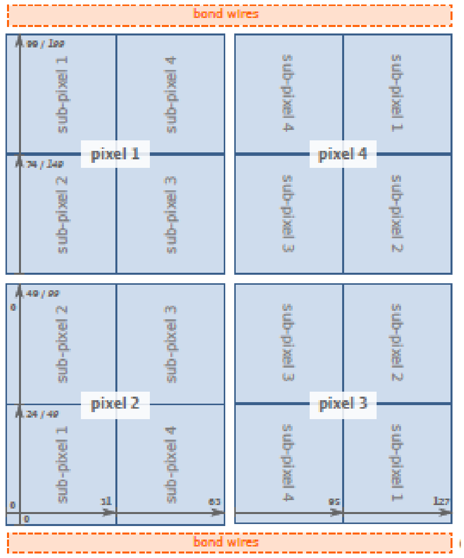

Figure 52: DPC3200-22 die layout [35]

The DPC3200-22-44M22 (Module-TEK version) containing the 4 tiles is provided with an aluminium housing designed for good heat transport from the tile sensors in order to stabilize the temperature when cooling the module, a local voltage conversion extension and a protective metal cover to shield the sensor electrically and mechanically.

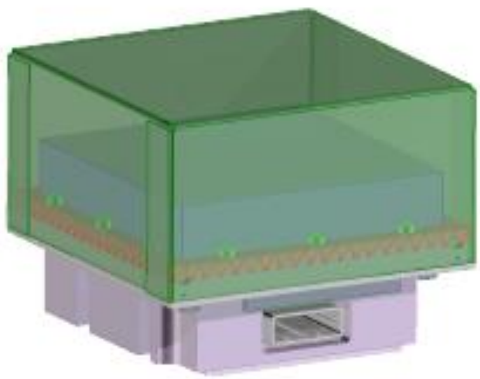

Figure 53: DPC3200-22-44-M22 module with cover [35]

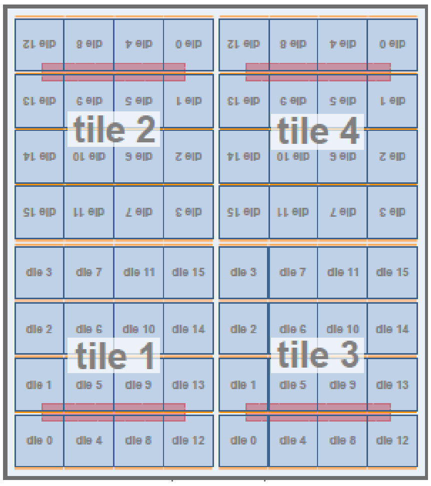

Figure 54: DPC3200-22-44-M22 module layout [35]

3.1.2 Principle of operation

These detectors operate with an event-based acquisition sequence. To start this sequence, individual dies need to detect enough photons to pass the threshold. Once the microcells are charged, the die will wait for the start of the event be in the ready state until a trigger occurs. When the trigger scheme is satisfied, the event acquisition starts.

There is a validation interval (5-40 ns) which separates real events from dark counts acting as a second threshold. If the validation scheme is fulfilled, the event will be validated, otherwise, the sensor will go to the recharge phase.

Once the validation interval has finished, the die enters in an integration phase (0-20 μs) in which it waits for more the delayed photons belonging to the same event. Usually they are delayed because of the decay of a crystal scintillation event.

After successful integration, the readout process starts (680 ns), where the state of the microcells is read row by row. A separate photon count per pixel is given when the number of discharged cells is summed up. The photon count values for the four pixels of each die are sent to the external data processing together with the trigger timestamps.

Finally, a global sensor charge is done (20 ns), preparing the sensor for the next event acquisition.

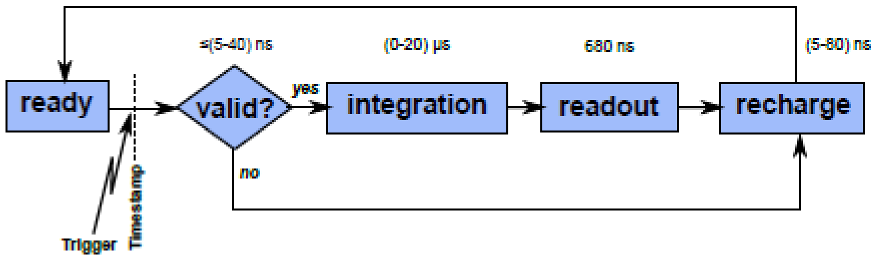

Figure 55: Event acquisition sequence for one event [35]

As it has been said, trigger conditions must be fulfilled in order to initiate the acquisition sequence. This trigger is the responsible of discarding the dark count events and is generated in each of the pixels as photons are detected in the different subpixels.

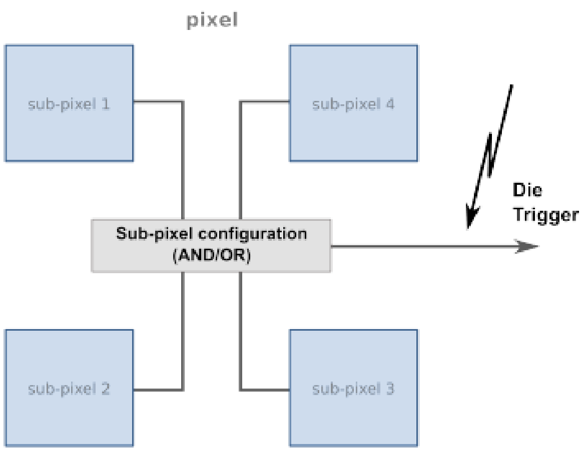

Figure 56: Trigger logic for a single pixel [35]

Trigger schemes are achieved by Boolean interconnections (OR/AND) of the triggers from the four subpixels. Depending on how they are connected, four different trigger schemes are supported (see **Table 2**). The most permissive one is trigger scheme 1, in which all subpixels are connected via OR gates, so one single cell discharge in any of the four subpixels causes the generation of the trigger signal. In trigger schemes 2 and 3, OR and AND combinations between subpixels are configured, being the former more tolerant than the later. Finally, trigger scheme 4 constitutes the most restrictive one, having all subpixels ANDed, so all of them need to have a cell discharge to generate the trigger signal.

Trigger Scheme	**Sub-Pixel Configuration**	***Average* Threshold**
1	sp1 ∨ sp2 ∨ sp3 ∨ sp4	1.0
2	[(sp1 ∨ sp2) ∧ (sp3 ∨ sp4)] ∨ [(sp1 ∨ sp4) ∧ (sp2 ∨ sp3)]	2.3
3	(sp1 ∨ sp2) ∧ (sp3 ∨ sp4)	3.0
4	sp1 ∧ sp2 ∧ sp3 ∧ sp4	8.3

Table 2: DPC3200-22 trigger settings [35]

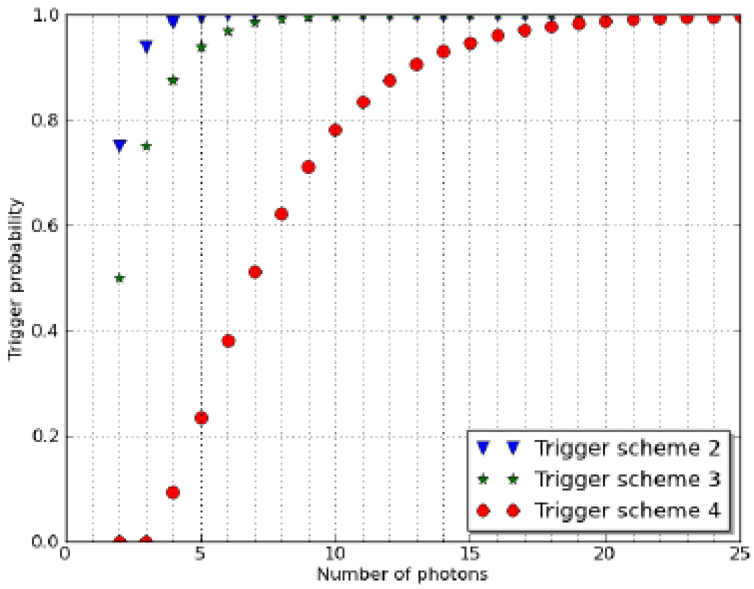

Figure 57: DPC3200-22 trigger probabilities [35]

For trigger schemes 2, 3 and 4, a false trigger can be generated by accumulation of dark counts over time. The sensor provides a fast recharge mode to avoid this problem, in which, if after a short interval of time none of the pixels generate a die trigger, full cell rows are recharged: the RTL refresh (row-trigger-lines). It checks all RTLs each 10 ns, and in case that one has triggered but no die trigger was generated after 20 ns, the sensor recharges it. One of the side effects of this mode is that it may increase noise, as there is a possibility that photon bursts are generated by photoemission, appearing as events in the data file.

Apart to the trigger logic, there is another threshold that checks for the distribution of cell discharges validating the ones that accomplish it and discarding which not: the validation logic. The subpixels of DPC3200-22 sensors are composed of 25 RTLs each, which are combined in groups of three or four, and if one of this detects a cell discharge, the logic gate is set to *high*.

There exist a 7-bit validation pattern which defines which of the gates are ANDed or ORed, being the validation pattern 00x7F the most tolerant (all gates as OR), and the validation pattern 0x00 the one with the highest threshold (all gates as AND). In **Table 3**, some of the validation schemes are shown with threshold values obtained from simulations (*tbd* means simulation pending). The threshold refers to the number of activated SPADs needed to validate the event.

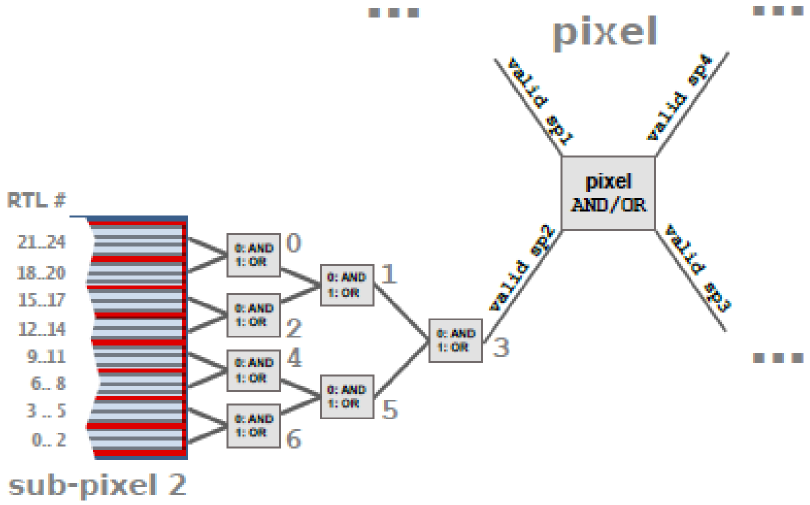

Figure 58: Validation logic of the DPC3200-22 [35]

Validation Scheme	Validation Pattern	Threshold (Average)	Threshold (Minimum)
1	0x7F:OR	1	1
2	0x77:OR	4.6 (± 2.1)	2
4	0x55:OR	16.9 (± 6.2)	4
8	0x00:OR	52.2 (±15.)	11*
16	0x55:AND	*tbd*	*tbd*
32	0x00:AND	*tbd*	*tbd*

Table 3: Predefined validation schemes with simulation results [35]

In order to control the dark count rate of the sensor, each tile contains a flash memory chip that can able or disable individual cells by writing the "inhibit memory", as was explained in the previous section. The hugest contribution to the whole dark-count rate is caused by a small number of cells (usually 10% of cells contributes to 70-80% of the total dark count rate), so by disabling them, it can be reduced. By measuring the dark-count rate of each single cell in complete darkness, a dark count map can be represented, and if those cells causing the highest rate are disabled, the detector performance will be improved (explained at the end of section 1.3.3.3.3). See **Figure 59** and **Figure 60**.

To have an optimum PDE and avoid high dark count rates (and so a successful operation of the sensor), the bias voltage needs to be properly set. This parameter is given by the following equation:

$$V_{bias} = V_{break} + V_{excess} \quad (8)$$

where V_{break} is the breakdown voltage of the cells and V_{excess} is the excess voltage. The excess voltage is 3.0 V by default. It is necessary to adjust the bias voltage periodically and measuring at the temperature at which the measurement will be performed, as it shifts +20 mV/ºC.

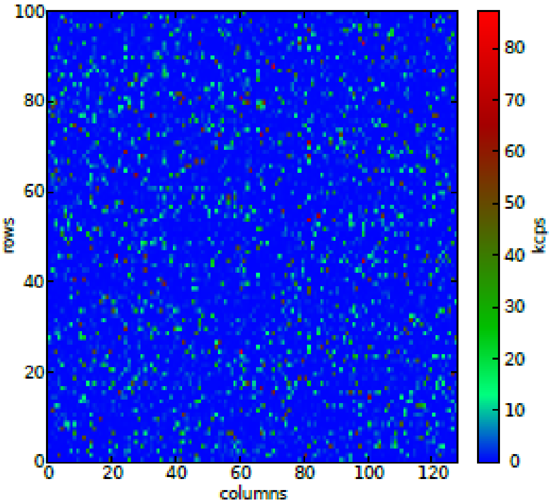

Figure 59: Dark count map example [35]

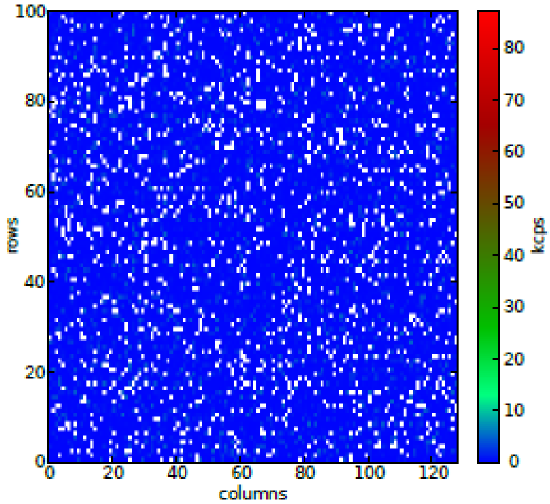

Figure 60: Inhibited dark count map example [35]

For an optimal functioning of the PDPC, a cooling system is crucial to maintain the detectors at low, constant temperatures. If the temperature increases, not only the breakdown voltage will increase, but also the dark count rate. All this section is taken from the PDPC Module-TEK manual [35], as it is the only reference available in the literature.

3.2 Cooling system

To maintain the detectors at low, constant temperature, a cooling system composed of a recirculating chiller connected to Aluminium cold plates was used. These cold plates, in turn, were connected to the detectors applying a thermal silicone with the purpose of transmitting the heat properly.

3.2.1 ThermoCube 400

The ThermoCube is a recirculating cooling system that uses thermoelectric technology to deliver 400 Watts of cooling capacity. It does not need neither compressors nor refrigerants. This system provides a stable temperature control in an operating range from -5 to 65 ºC with a stability of only ±0.05 ºC. Although it is recommendable to use a mixture of 27% propylene glycol / water as a coolant, it also allows to use only water. The tank volume is 300 ml, so it produces small wastes [36].

Figure 61: ThermoCube 400 [36]

ThermoCube is a very efficient chiller, as its thermoelectric modules are powered by a variable voltage supply providing the minimum power needed to control the desired temperature. In **Figure 62**, the cooling curves for the different models of ThermoCube (200, 300, 400 Watts) are represented. We are only interested in the red curve for 400 Watts [37].

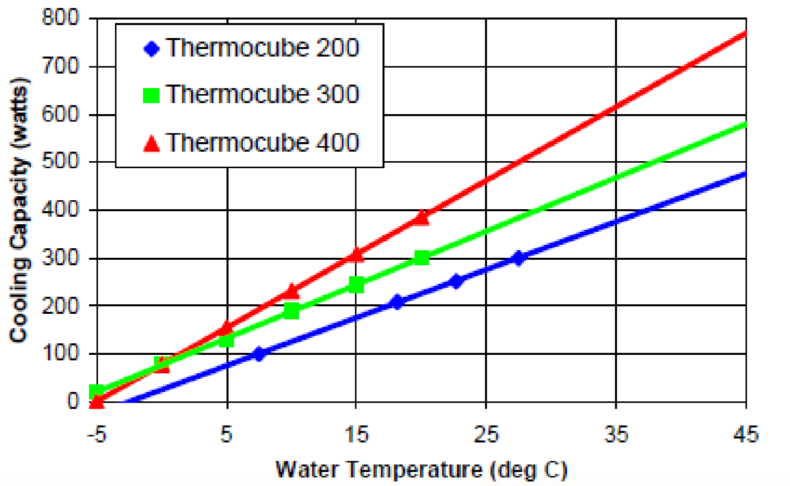

Figure 62: ThermoCube cooling curves at 20ºC ambient temperature [37]

3.2.2 CP10G14 Aluminium Cold Plate

To cool the two detectors, two CP10G14 Aluminium Cold Plates were used. These were connected to the ThermoCube process fluid supply by a system of tubes and John Guest connectors.

Figure 63 Front: view of CP10G14 Al cold plate [38]

Figure 64: Back view of CP10G14 Al cold plate [38]

These are single-sided aluminium cold plates consisting of cooper tubes pressed into a channelled aluminium extrusion. They are used for cooling applications where the heat load is low-to-moderate, as it is the case of study [38]. The specifications for this model are collected in **(**see Annex A**)**

We performed some perforations mechanically to connect the plates with the detectors. As the bores of the sensor modules did not fit with the plates because of the cooper tubes, an additional aluminium plate was designed and fabricated (see Annex B).

We used a technique to improve the heat exchange efficiency: smearing thermal silicone at the Al cold plate-designed plate and the designed plate-detector interfaces.

3.3 Scintillator and Light Guide

In order to convert the electromagnetic radiation in the form of gamma photons emitted by the radioactive source into light photons measurable by the PDPC sensor, a scintillator coupled to a light guide was used. Optical silicone was smeared between the scintillator-light guide and the light guide-sensor interfaces.

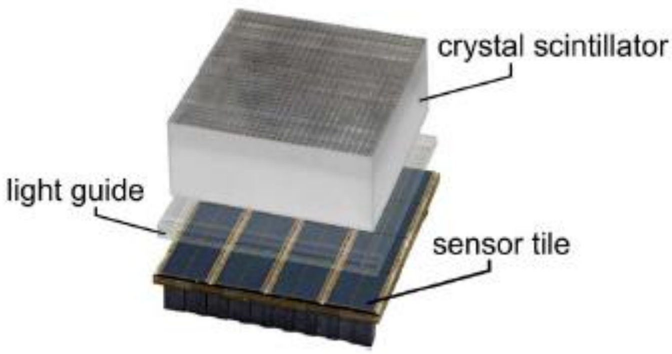

Figure 65: Arrangement of the scintillator-light guide-sensor stack [46]

3.3.1 Scintillator

The scintillators used for this project were 30×30 matrix of cerium-doped lutetium yttrium orthosilicate (LYSO) crystals with pixels of 1.3×1.3 mm and a height of 12 mm, with all faces chemically etched, surrounded by a 0.1 mm thick Lumirror film as inter-crystal reflector. In some sections of the experiment (4.2.6: Image improvement using different light guides), a scintillator composed of a 10×10 matrix of LYSO crystals with dimensions 1.2×1.2×12 mm covered with the same reflector was used.

The main properties of LYSO crystals are shown in the following table:

Density (g/m^3)	7.3
Melting point (ºC)	2047
Index of refraction	1.82
Radiation length (cm)	1.16
Attenuation (cm-1)	0.87
Decay constant (ns)	50
Light yield (%) Nal (TI)	75
Photofraction (%)	30
Energy resolution (511 kev, %)	20
Radioactivity	Yes

Table 4: Properties of LYSO crystals [39]

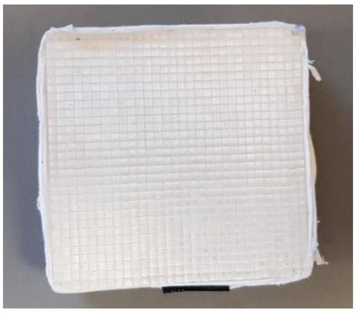

Figure 66: 30x30 LYSO scintillator

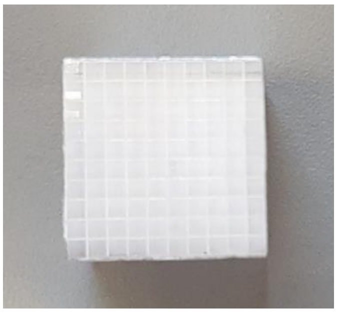

Figure 67: 10x10 LYSO scintillator

3.3.2 Light guide

Light guides of 12×12 and 1, 2, 3 and 4 mm thick were used to study which gave the best result with our detectors. The results of said experiments were that the optimum light guide thickness was 2 mm. For this reason, the light guides used were borosilicate windows, float grade, 50×50×2 mm thick, double sided AR coated 400-1000 nm. They have a refractive index of 1.472 and excellent transmission over the visible and NIR wavelengths from 310 nm to 2700 nm, so they are perfect for the purpose of this project [40] (The specifications of this light guide are collected in Annex C).

3.3.3 Optical silicone

The optical silicone used was the BC-630 Optical Grease, composed with 90-95% substituted polysiloxane and 4-6% silica, amorphous fumed. Its light transmission is 96-98% at wavelengths of 400-500 nm with an index of refraction of 1.463 [41].

3.4 Optical breadboard

As PET systems need a very precise location of the opposing detectors and the radioactive source to work in a proper manner, an optical breadboard was used. This way, the exact position of the detectors was well known.

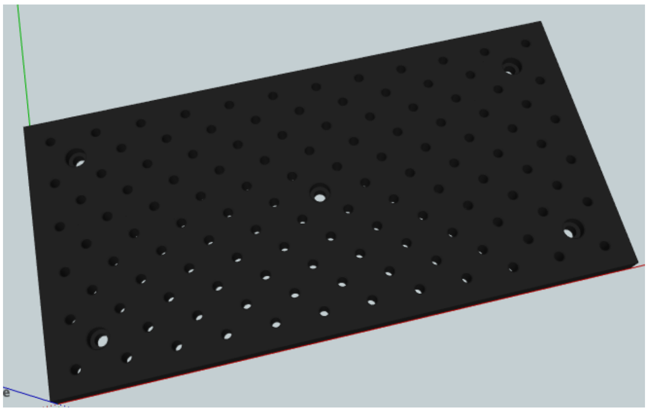

Figure 68: Optical breadboard[51]

3.5 3D Printer: Ultimaker 3

Ultimaker 3 is a 3D printer that uses dual extrusion combining build and water-soluble support materials to create mechanical structures ensuring a smooth, professional finish. The material used to print was PLA (polylactic acid), which prints dependably with high spatial accuracy and excellent surface finish [42].

Figure 69: Ultimaker 3 [42]

As the two detectors were one in front of the other to acquire coincident events, some pieces needed to be designed and printed. SolidWorks was used for the design of these pieces.

The first piece consists of a hollow square that would hold the light guide attached to the sensor tiles in such a way that it would not move.

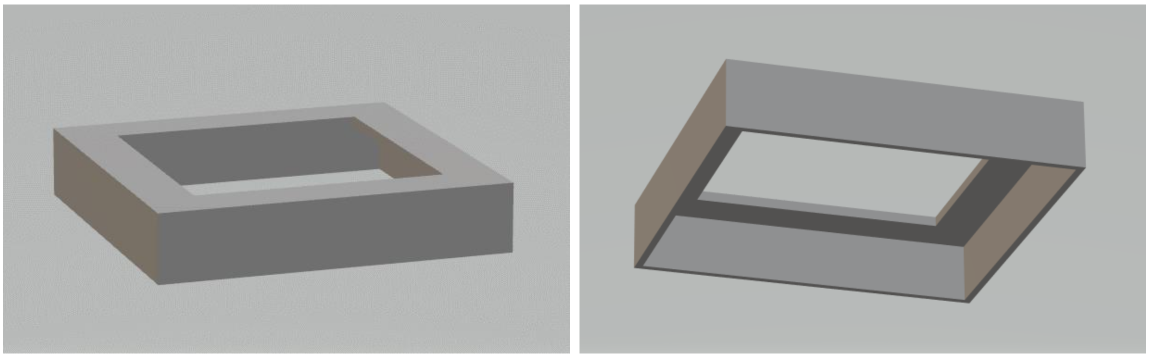

Figure 70: Top-side and bottom-side view of the piece supporting the light guide

The second one is a hollow cube embedded in the detector shield. It has space to fix inside the scintillator ensuring that it does not move. It will also cover the piece shown above with the purpose of coupling the scintillator and the light guide.

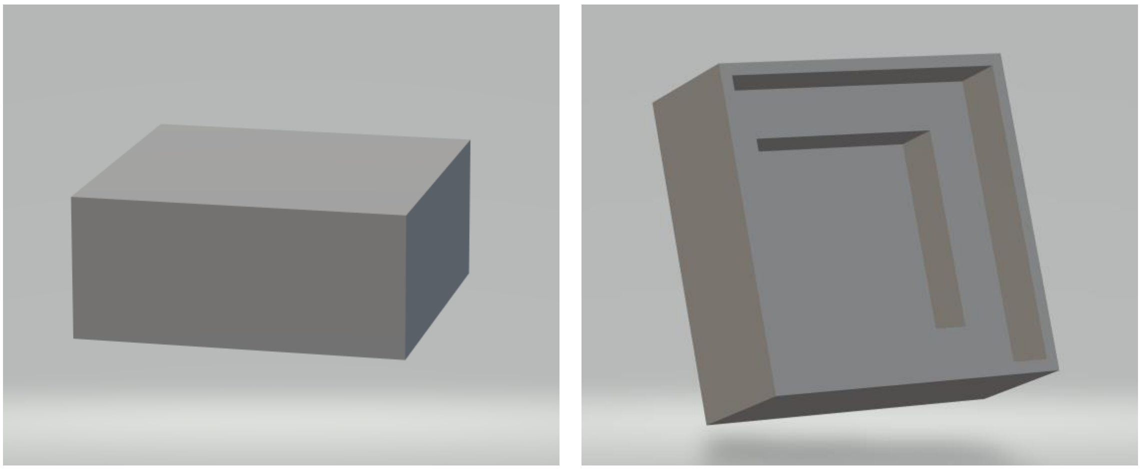

Figure 71: Top-side and bottom-side view of the piece supporting the scintillator

Once both pieces are coupled together with the scintillator and the light guide, they will be placed over the sensor module and the aluminium shield will close the whole stack.

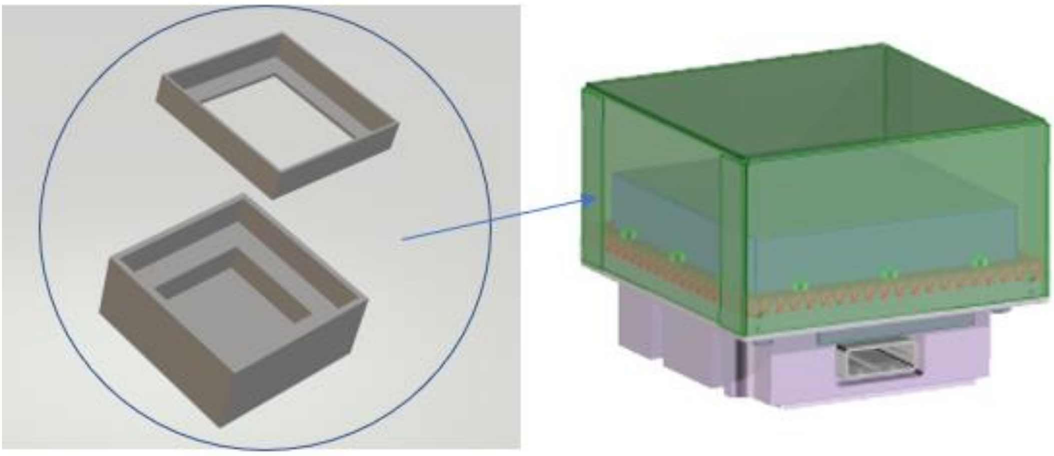

Figure 72: Both pieces together would be placed inside the shield

We designed a third piece to maintain the detectors vertically and fixed at an exact position. Since the experiment was mounted in an optical breadbord, screw holes were designed with excellent accuracy.

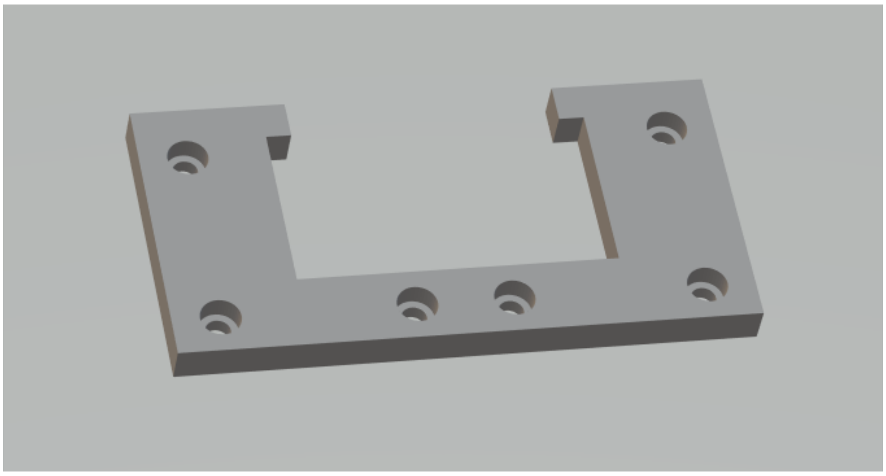

Figure 73: Piece supporting the detector at a fixed position

3.6 Radioactive Point Source

The isotope chosen is Sodium-22 (^{22}Na), an isotope with a half-life of 2.6 years. It decays by β^+ emission, what means that it emits a positron converting into stable ^{22}Ne (apart of emitting a positron, a proton in the nucleus is transformed in a neutron). Most of the decays lead to an excited state of neon, which passes into ground state emitting a 1275 keV gamma photon.

As the ^{22}Na emits a positron, it annihilates with a nearby electron leading to two gamma photons in opposite direction with an energy of 511 keV each [43].

Figure 74 represents the typical spectrum of this isotope of sodium with the respective peaks of energy as 511 and 1275 keV.

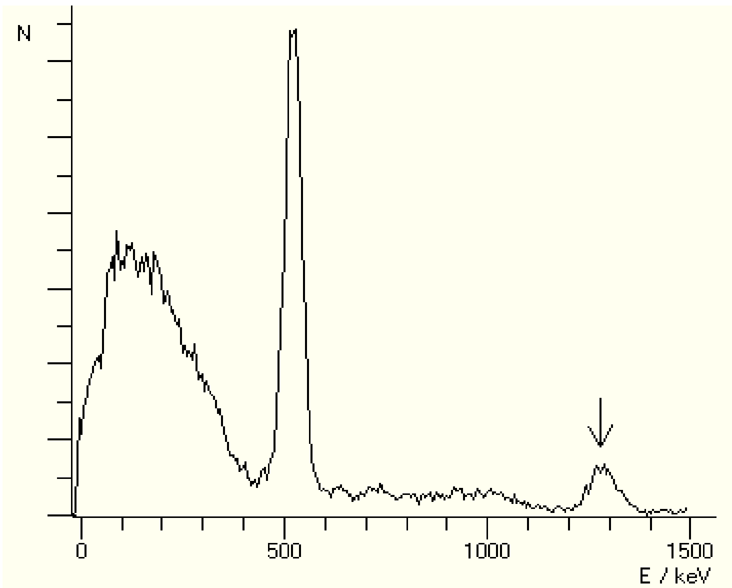

Figure 74: Typical spectrum of ^{22}Na [43]

We used as a radiation source an exempt ^{22}Na point source. It is a 25 mm diameter and 3mm thick plastic disk suitable for performing experiments involving radioactivity. This source had an activity of 1 μCi [44] when purchased, and currently, 4 half-lifes have elapsed, meaning that its current activity is 69.5 nCi. This source is exempt according to the regulations in [45]. Although it does not emit too much radiation, it is enough for the purpose of the experiment. There exist several protocols when handling radioactive material, and since the project is realized by a student, a source with high level of radiation cannot be used.

Figure 75: Set of radioactive sources including ^{22}Na used in the experiments [44]

4 METHODS AND RESULTS

4.1 Learning to work the system: preliminary results

In this work, all the acquisition process was performed with DPCShell, a console-based Linux software that provides all the commands needed to control, configure and operate the PDPC-TEK setup. Since all the equipment was bought some years ago, it was necessary to update it with the latest versions of the software. All the data processing and analysis was performed using Matlab. It took several weeks to understand and control the DPCShell software.

4.1.1 Calibration of the sensors

Previous to the data acquisition, the setup needed to be calibrated for optimal performance using the commands provided by the DPCshell software.

4.1.1.1 Dark Count Map

First of all, a dark count map was measured. About the 10% of the cells of each die are responsible for the vast majority of dark counts, and by inhibiting them, the sensor's efficiency is improved. For that measurement, the sensors were in completely darkness thanks to the black aluminium cover.

All the figures shown in this section belong to the die 0 of the tile 1 of one of the detectors.

4.1.1.1.1 Dependency on temperature

As has been explained, a constant, low temperature is fundamental for the proper functioning of any photodetector. When the dark count maps were measured without a proper cooling system, high amounts of dark counts appeared in a huge number of cells.

Figure 76 and **Figure 77** show how the median of the dark count rate decreases for lower temperatures from 2.655 kHz to 915.527 Hz. It can be observed how the red and green dots (high kcps) are reduced in the DCM with the use of a cooling system. The inhibited DCM from the first image still show some cells with around 15 kcps, while the one from the second one, has inhibited almost all the defective cells. This demonstrates that for lower temperatures, the dark count rate is decreased, improving the performance of the system.

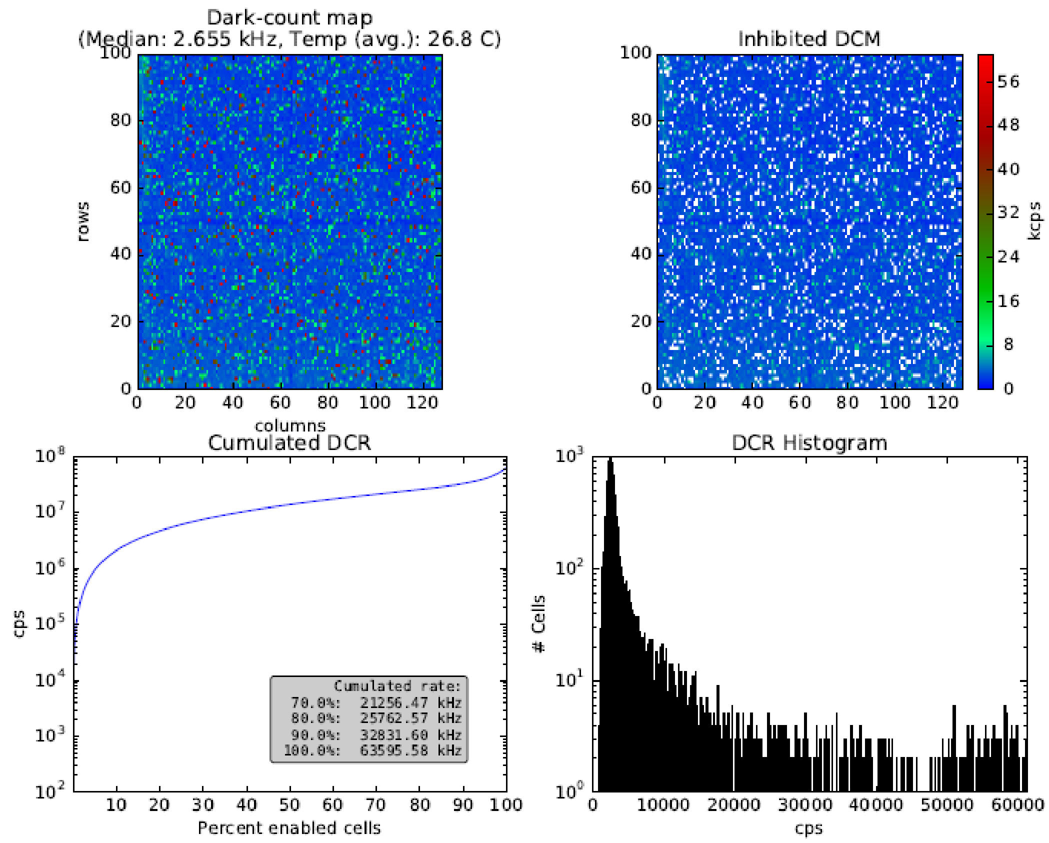

Figure 76: Dark-count Analysis for 100 frames (default) without cooling system

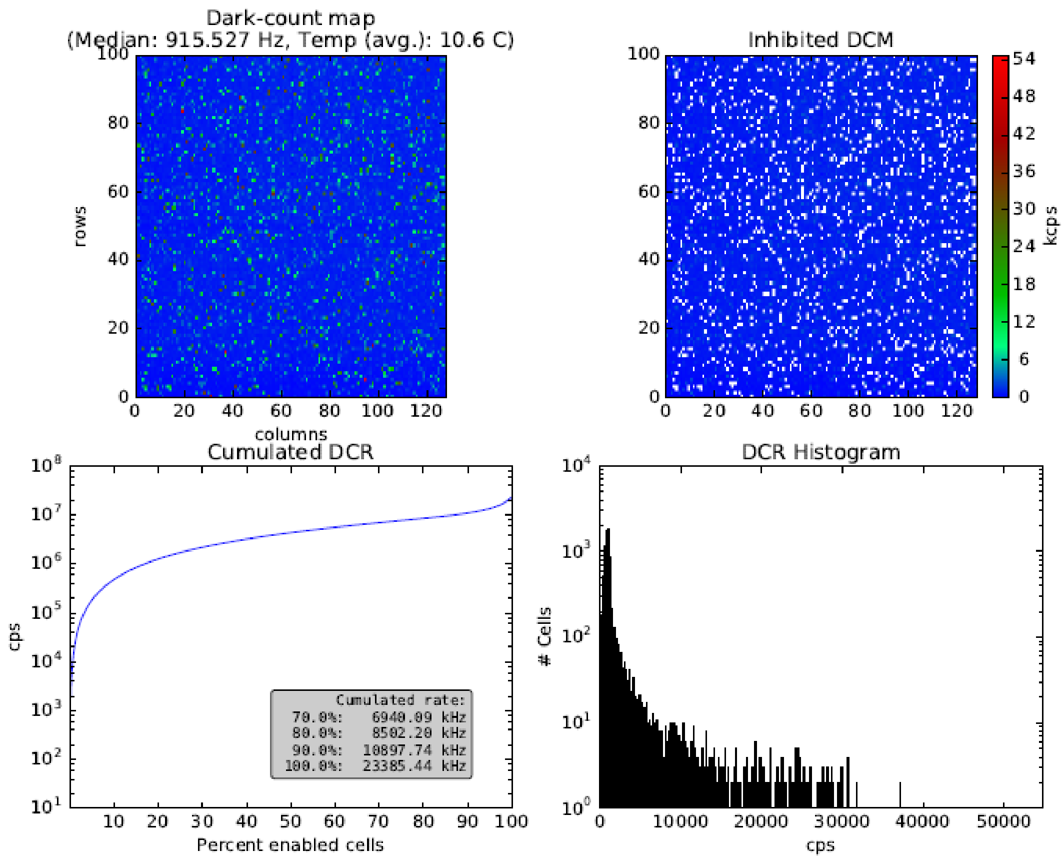

Figure 77: Dark-count Analysis for 100 frames (default) with cooling system

4.1.1.1.2   Dependency on the number of frames selected

As for lower temperatures, fewer dark counts are produced, it is necessary to augment the time per cell to obtain enough statistics. This time is augmented by increasing the number of frames for which each cell is measured.

By looking at **Figure 76** and **Figure 78**, the first difference is that the mean temperature has risen when increasing the number of frames. The reason is that when acquiring data, the detectors warm up, and for longer acquisition times, the mean temperature will rise slightly. Despite this, the median of the dark count rate has lowered to 576.782 HZ and the inhibited map looks similar or better, so it has been proven that increasing the time that each cell is measured, the obtained dark count map is improved.

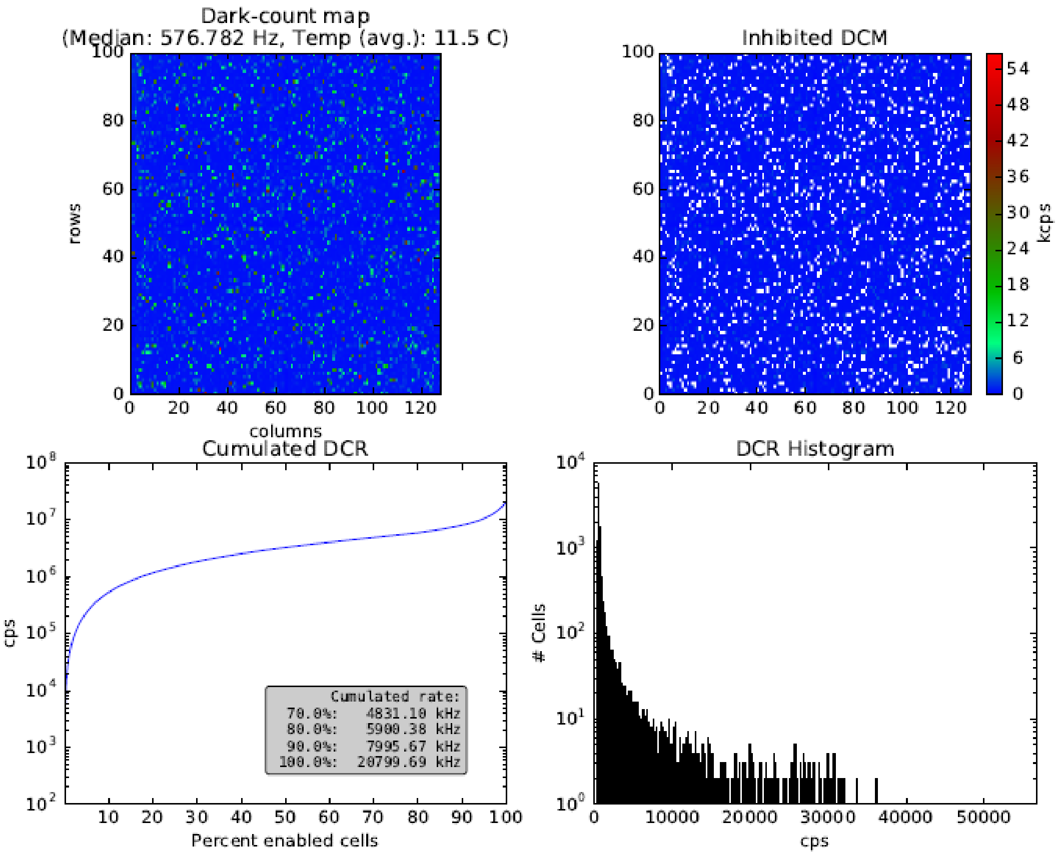

Figure 78: Dark-count Analysis for 1000 frames with cooling system

The next data acquisition was performed with the inhibited DCM of **Figure 78**.

4.1.1.2 Time-to-digital converter

After the DCM was calibrated, the statistical nature of the detector timestamp distribution needs to be calibrated as well. For this, the DPC shell provides us with a TDC calibration routine. This routine calculates the timing differences and uploads them to the tile flash memory, so that the correction can be applied to the timestamp values. These timestamp values have a bin width of 10 ns/512=19.5 ps.

4.1.2 First acquisitions

The results presented in this section were acquired using the default acquisition parameters, we used them to understand first how the system worked. For the same reason, no radioactive source was employed. To acquire data with the detectors, we used the command “capture” on the DPCShell console, specifying the total number of frames to acquire (capture --nframes <num_frames>). The acquisition data is stored as CSV file.

#> bb,	mod,	tile,	die,	frame_nr,	delay,	timestamp,
1,	1,	1,	9,	6115,	0,	94108,

p1,	p2,	p3,	p4,	temp,	status,	event_id,	frame_cou...
20,	3,	3,	17,	10.06,	0,	1,	0

Figure 79: Data acquisition format

Each line of the acquired data table indicates to which DPC module it belongs, the tile, the die, the timestamp of the acquisition, the number of photons acquired by each of the four pixels and the temperature of the measurement. It is worth mentioning that what the system calls “event” is each of the data lines, referring to the acquisition of a single die. However, on this work, we will refer to “event” as the annihilation event to which a burst of photons is associated (it may be detected by more than one die). We will assign all photons to a single event according to a time window.

Once an acquisition is performed with the DPCShell software, it returns several capture data files, each of them contains plenty of data lines as those of **Figure 79**. The number of captures that the system returns depend on the number of frames chosen. This is passed to the DPCShell as an acquisition parameter, with the command described above.

4.1.2.1 Organization of data in events

The only time reference that we have is the timestamp. This timestamp has a bin width of 19.5 ps as it was explained in the previous section, so by multiplying the timestamp number by 19.5×10^{-3}, we get the time in nanoseconds, a more relevant time unit than bins. Time windows in PET detectors are generally specified in nanoseconds. In order to organize the data in events, a proper time window needed to be selected. Data lines from different dies that belong to the same time window would be assigned to the same event. It is obvious that data associated to the same event will belong to dies very close to each other. In these first acquisitions, a large time window was selected, as we only were interested in learning how to work the system, but afterwards, a detailed study of which time window would be the most efficient was performed (section 4.2.4).

4.1.2.2 First energy spectra obtained

Once the data was organized in events, the next step was to create a recognizable energy spectrum. The detectors used are digital photon counters, so they only count the number of photons that arrive at each pixel before the cells are recharged. The sum of the number of photons counted by the four pixels of each die belonging to the same event would give a value proportional to the energy of that event. We can sum all these values from a single event and use several events to generate an energy histogram.

In the first acquisitions, as it has been said, no ^{22}Na source was placed near the detector, so only the scintillator intrinsic radiation was acquired. We took two acquisitions to study the effects of temperature on the sensors: one at 12 ºC and the other at 30 ºC. Both acquisition times were equal

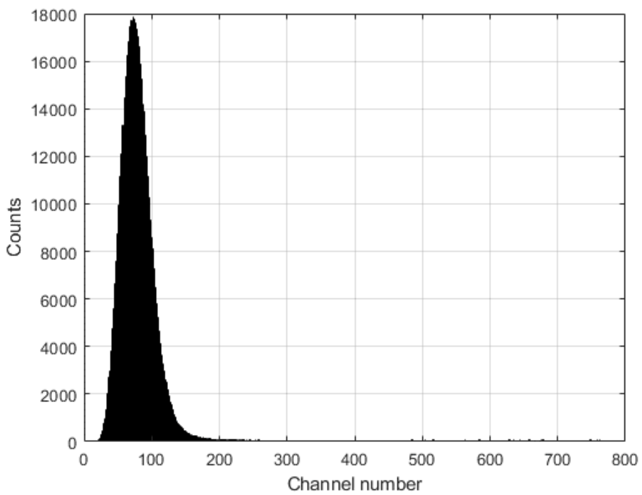

Figure 80: Energy spectrum obtained at 12 ºC

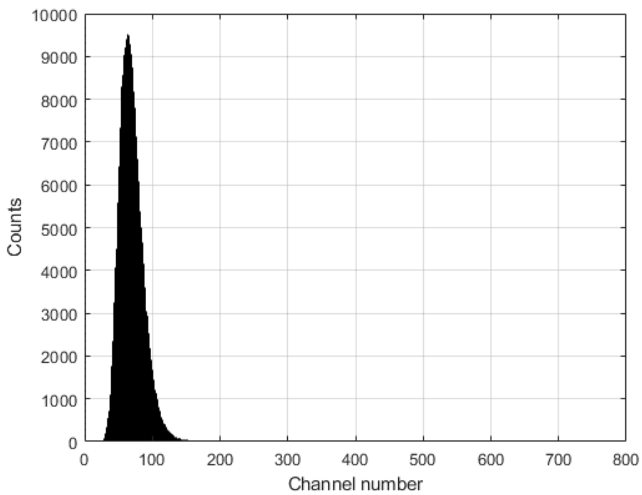

Figure 81: Energy spectrum obtained at 30 ºC

The majority of counts in both spectra fall in the lower channels, corresponding to low energies because of dark counts. It makes sense as no radioactive source was placed near the detector, so only noise was acquired.

For the same acquisition time, in **Figure 80**: 1,000,051 data frames were acquired, while in **Figure 81**, only 381,377 data frames were obtained. It is also reflected in the number of counts, as the peak of the Gaussian of the 12º detector is almost double the one at 30º. The reason is that as the sensor warms up, the gain decreases and the dark counts increase, so the spectrum at 30º has less counts and the peak of the Gaussian is slightly displaced towards the less energy channels.

Finally, the ^{22}Na source was placed near the detector, with the cooling system implemented. After setting the proper acquisition parameters (discussed in section 4.2.3) and a proper time window (discussed in section 4.2.4), the spectrum of **Figure 82** was obtained, which resembles the ^{22}Na spectrum of **Figure 74**. For this first spectrum, only one capture data file was analysed in order to have the same statistics as in the previous ones.

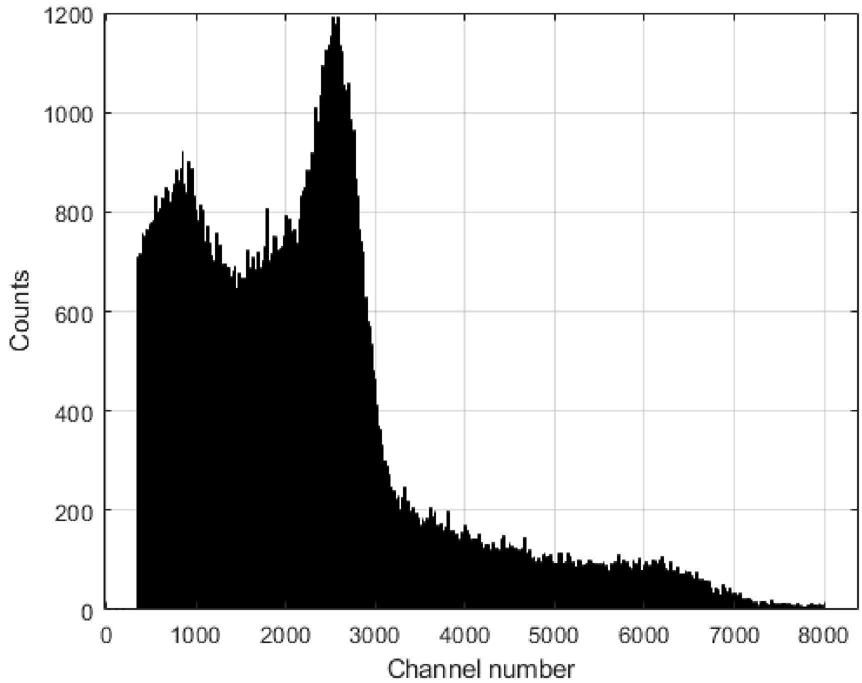

Figure 82: First ^{22}Na spectrum

4.2 First flood field images

All the results of this section were taken with the source of ^{22}Na placed near the detector. After the energy of each event was stored and its spectrum was plotted, the next step was to locate those events in the detector, obtaining a flood field image (basically a two-dimensional histogram where the photons acquired by each pixel are summed up). These events will depend completely on the energy spectrum, as not all the signals from the detectors are used. We are not interested neither in noise nor scatter events, which would produce an error in the position, blurring the flood image. Noise events can be discarded using energy thresholding on the acquired events.

4.2.1 Implementation of the centre of gravity for positioning

Energy and position information related to each event are needed to generate flood images. Once the energy and position of all the pixels belonging to the same event are obtained, a centre of gravity will be implemented to locate that event.

4.2.1.1 Energy Vector

One sensor is composed of 4 tiles, with 16 (from 0 to 15) dies each, and 4 pixels per die, what gives total number of 256 pixels. A position from 1 to 256 was assigned for each of those pixels, being “pixel 1, die 0, tile 1” the first position, and “pixel 4, die 15, tile 4” the one at position 256.

Then, for each event, the number of photons of each pixel was summed up in its corresponding position, in such a manner that it will be full of zeros except in the positions where photons had been detected. We can use the energy related to each pixel to perform a weighted sum that will give the event location.

4.2.1.2 Position Vector

The 256 pixels are arranged in a 16×16 matrix in the detector, so each of them will be assigned an x-position and a y-position, being the pixel in the lower left corner (1,1) and the one in the upper right corner (16,16). The bad news are that they are not arranged in a straight forward manner (pixel 1 does not correspond to (1,1) nor the pixel 256 corresponds to (16,16)), so it was tricky to fill a vector of dimensions 2×256 where each pixel number has its x-y location.

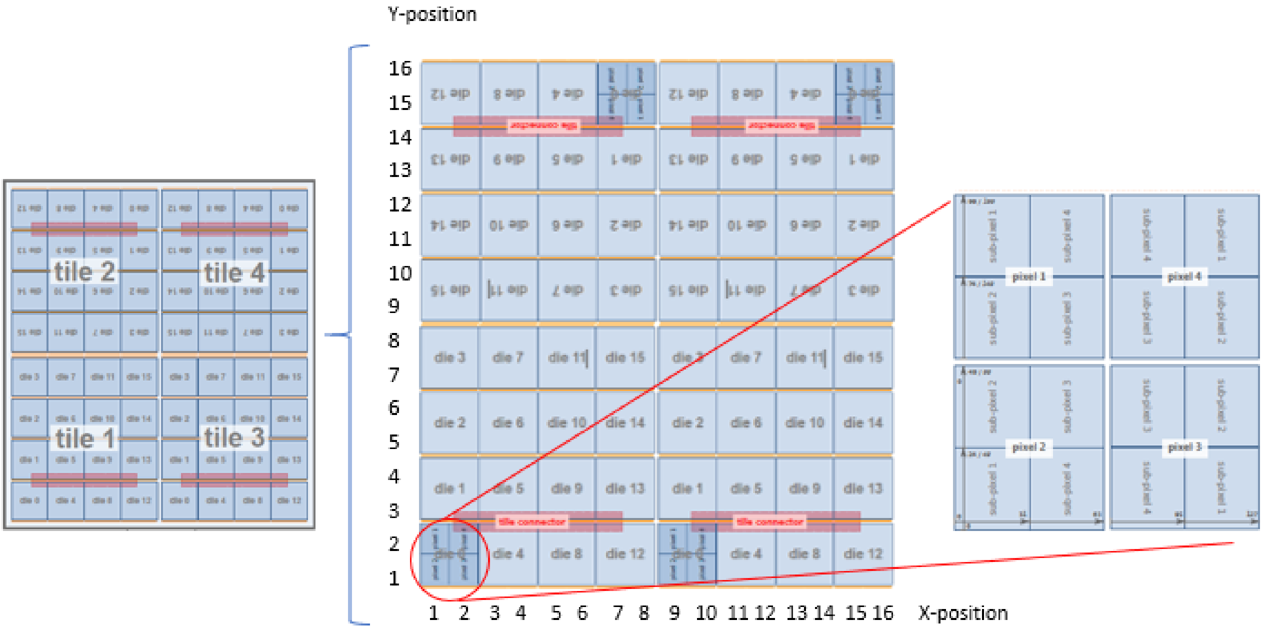

Figure 83: Representation of the x-y arrangement of each pixel in the detector

An example of how the list of x-y positions was arranged to each pixel can be seen in **Figure 84**, where the first row corresponds to the pixel number and the second and the third ones, to its x-y location.

60	61	62	63	64	65	66	67	68	69	70
8	7	7	8	8	8	8	7	7	8	8
6	8	7	7	8	15	16	16	15	13	14

Figure 84: Example of the x-y arrangement of the pixels

When the energy and positions vectors were acquired, for each aquired event, the software developed found the position for each event taking into account the total energy of said events. Events need to be compensated accoding to their total energy in order to acquire a proper positions, lets remember that not all events will have the same energy.

The Center of Gravity algorithms were applied following the equations (9) and (10):

$$X_{position} = \frac{\sum_i x_i q_i}{\sum_i q_i} \quad (9)$$

$$Y_{position} = \frac{\sum_i y_i q_i}{\sum_i q_i} \quad (10)$$

where x_i and y_i are the position of each pixel in the detector and $q_{i,}$ the total number of photon counts for that pixel. A matrix 2-dimensional matrix with the x and y positions of each event was created.

4.2.2 Flood field image generation

Once each event was located, we generated the flood field image.

We had to take into account that the values of the positions would have a range from 1 to 16, and we wanted a 512x512 image. We had to consider also the reference coordinates system: matlab assigns the first pixel to the upper-left corner, while the centre of gravity algorithm created assigned the first pixel to the bottom-left corner. The flood field image was generated in the following way:

1. Divide the positions of the event by 16, multiply by 512 and round the resulting value to have x-y positions from 1 to 512
2. Create the image array and fill it with zeros
3. Loop from the first to the final x-y position of each event.
    a. Add 1 to the 512x512 matrix in the corresponding position of each event
    b. Take care with the columns vector, as the y-position the event would be (513 – y position)
4. At the end, a two dimensional histogram with the number of event at each position of the matrix is obtained

4.2.3 Selection of the acquisition parameters

The default parameters offered by the system are collected in the following table.

Trigger scheme	4
RTL refresh	Off
Integration interval	165 nsec
Validation pattern	0x00:OR
Validation interval	5 ns

Table 5: Default acquisition parameters

The DPCshell command “config set” allows to select these parameters (config set --trigger <trg_scheme>, config set --val-len <nsec>, etc).

After trying several combinations of these parameters, we realised that the trigger scheme that better fitted our expectations was the third. We did not want a validation pattern too permissive nor too restrictive. Taking as a reference the results obtained in [46], it was decided to use the following combination:

Trigger scheme	3
RTL refresh	On
Integration interval	165 nsec
Validation pattern	0x54:OR
Validation interval	40 nsec

Table 6: Selected acquisition parameters

These parameters were also the ones used by the researchers on [20] when they were working with the Hyperion II^{D} system. Their good results invited us to test this combination of parameters too.

Figure 85 and **Figure 86** represent the flood images obtained with the parameters of the previous tables respectively. They both were taken with the same number of data frames (see **Figure 79**), 4 million, and with an event time window of 20 nanoseconds (explained in the following section: 4.2.4). As the trigger scheme had a high threshold (trigger scheme 3), the cooling system needed to be applied, and so did the RTL refresh. Since the validation interval was much wider, the separation of real events from dark counts was much more efficient. That is the reason why the number of valid events is lower in **Figure 86**. The default validation pattern (0×00:OR) needs an average number of activated SPADs of 52.2±15 and a minimum number of 11 in order to validate the event, whereas the validation pattern used (0×54:OR) needs an average of 27.5±10.3 and a minimum of 4 activated SPADs.. It was not as restrictive as the default scheme, but the results were much better, as can be seen in the following figures.

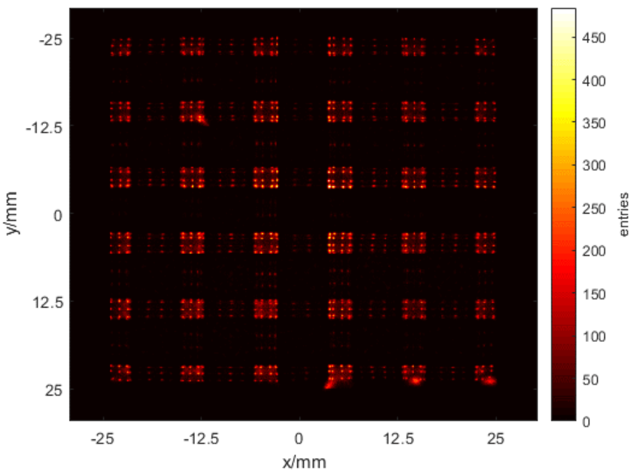

Figure 85: Flood image with default acquisition parameters

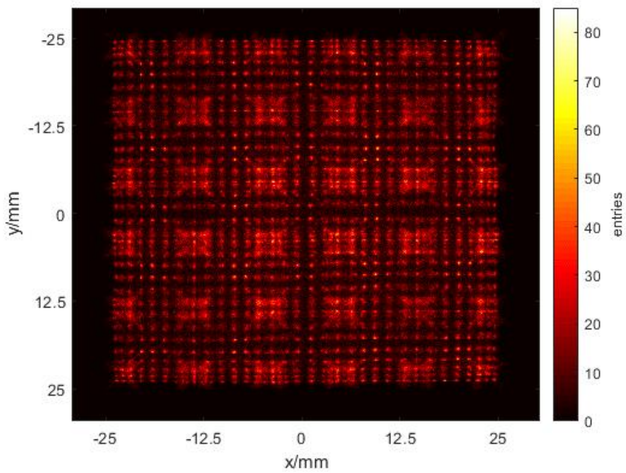

Figure 86: Flood image with selected acquisition parameters

In **Figure 86**, the 30×30 matrix of crystals can be more differentiated, whereas in **Figure 85** some shadows are observed. The reason may be either a too low validation interval in which some dark count may appear as valid events, the disabling of the RTL refresh, or it could be related to the trigger scheme or validation pattern used.

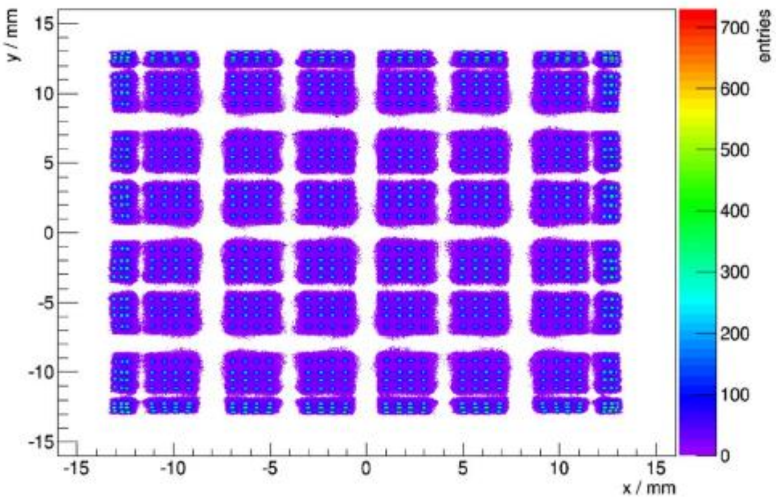

Figure 87: Representation of the flood field image obtained in [46]

Figure 87 represents the image obtained in [46], which was taken as the gold standard for this work. Each of the light blue dots represent the position of each crystal in the scintillator array. These researchers used also a 30×30 scintillator matrix of LYSO crystals with a height of 12 mm and a pitch of 1 mm, coupled to a light guide of 2mm. Their work is based in demonstrating that their method improves the sensitivity of the Hyperion II^{D}, the system mentioned in section 1.4.1.

4.2.4 Selection of the proper event time window

When the acquisition settings were configured, a proper time window was selected. This time window is fundamental to group photon bursts belonging to the same event and avoid mixing those from different ones, as neither their energy nor position would have true nor confident values.

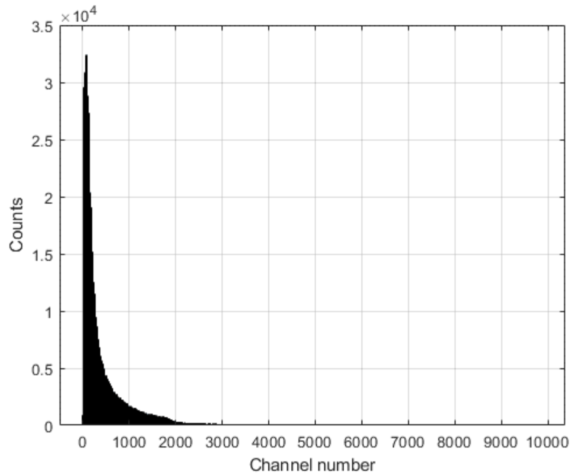

Figure 88: Energy spectrum without time window

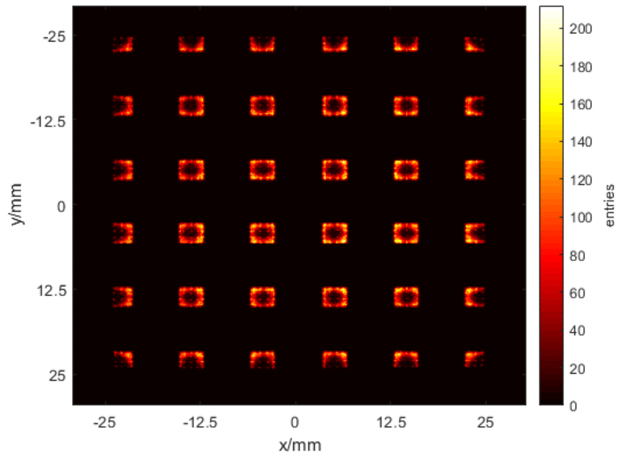

Figure 89: Flood image without time window

To know if the time window selected is the proper one, we need to check the energy spectrum of the events and how they are distributed when arriving to the detector. First, no time window was selected, and the result was the following:

Without a time-window, the developed program considers that each of the photon bursts arriving to a single die at the same time belongs to the same event, which is false. This is the cause why the energy spectrum in **Figure 88** decreases exponentially and all the counts belong to small channel numbers, as in a real event the photons are distributed along more than one die. The same reasoning can be applied to the flood image of **Figure 89**. The location of the event can only be distributed in a single die, along the centres of its four pixels, what is also wrong. We need a time window to correctly locate the positions of the crystals.

Then, a time window of 5 ns was applied:

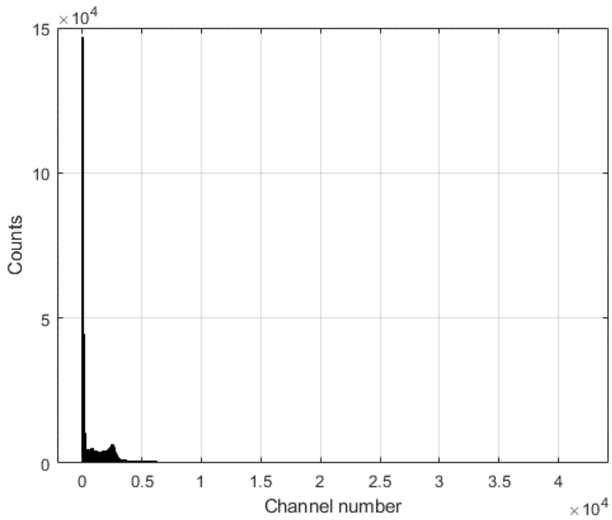

Figure 90: Complete energy spectrum with a time window of 5 ns

It can be observed that the spectrum of **Figure 90** accumulates a high number of counts at very low channels and that the histogram spreads to very high channels where there are almost no counts. This is due to noise present on some of the acquired events, so from now on, the resulting spectra will be shown at the interval of interest in order to evaluate them (from channel numbers 350-8000).

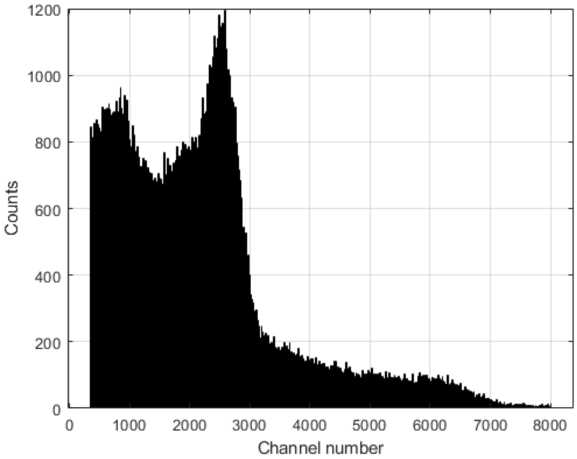

Figure 91: Interval energy spectrum with a time window of 5 ns

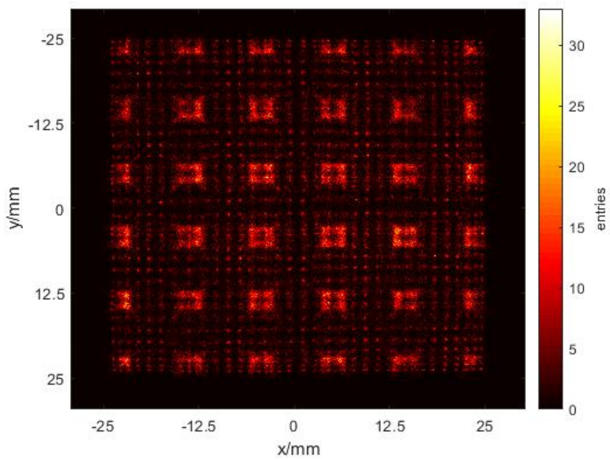

Figure 92: Flood image with a time window of 5 ns

It can be observed that the energy spectrum of **Figure 91** makes more sense, resembling the one of ^{22}Na with a very pronounced energy peak. When looking at the flood image, the positions of the crystals can now be recognized, although there is still a large accumulation of high energy events in the centres of the dies. The time window is not wide enough.

A time window of 10 ns was then applied:

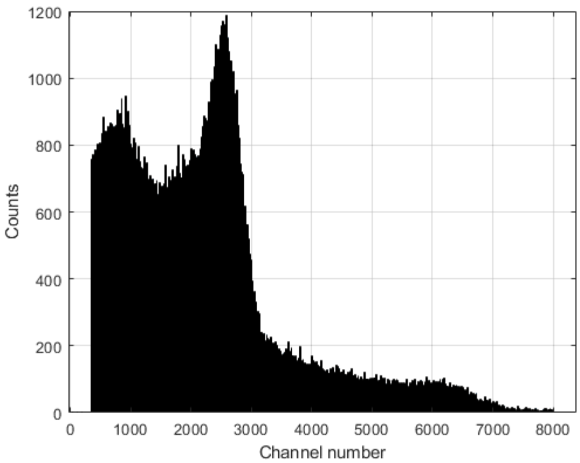

Figure 93: Energy spectrum with a time window of 10 ns

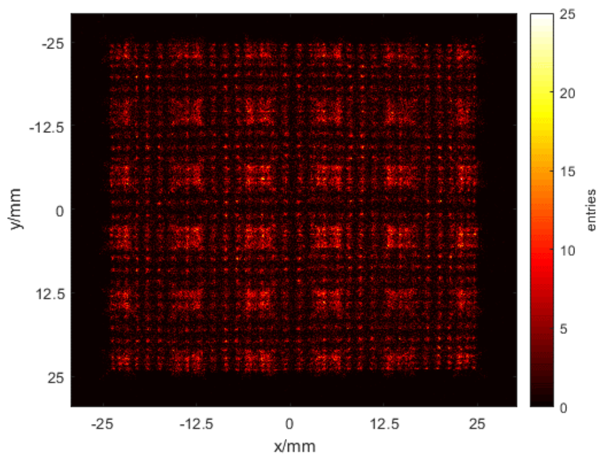

Figure 94: Flood image with a time window of 10 ns

The energy spectrum remains almost the same, but it can be seen how the flood image slightly improves. The events concentrated in the centre of the dies are now spreading to other positions, obtaining a better image.

With a time-window of 20 ns, the results were the following:

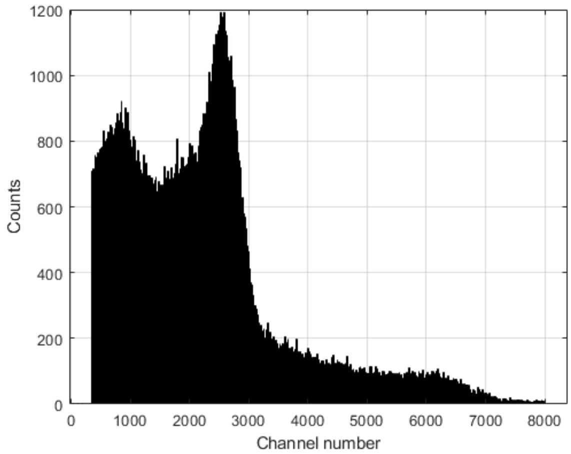

Figure 95: Energy spectrum with a time window of 20 ns

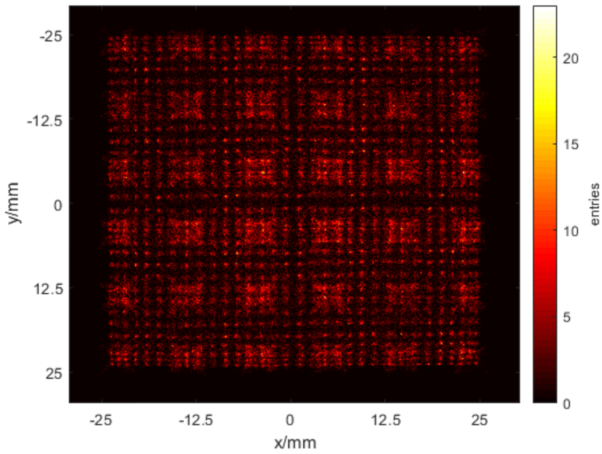

Figure 96: Flood image with a time window of 20 ns

The energy spectrum still resembles the same, and the flood image is further improved. Wider time-windows were tried, but the resulting images looked exactly like the ones for 20 ns. The reason is that the time intervals between different events is a lot more than the ones belonging to the same event. The combined effects of the validation and integration intervals together with our time window give us enough margin to acquire all the light from a LYSO scintillation event, considering that decay time of LYSO is 36 ns [47]. If we were to use a different scintillator, all these timing parameters will need to be readjusted accordingly. The conclusion is that the time-window of 20 ns fits perfectly to properly separate the different events.

To improve the flood image and eliminate the accumulation of high energy events in the centres of the dies, it is necessary to implement an energy window.

4.2.5 Selection of the proper energy window

For the reconstruction in PET imaging, only the energies of interest must be considered, discarding the ones produced by noise and scatter. The main function of the energy window is to select only those events with energies belonging to the photopeak of the radioisotope used, in PET imaging this corresponds to the 511keV photons from annihilation events. The energy spectrum is represented by channel number (proportional to the event energy). The energy window used is between 1500 and 3200 channel numbers, that corresponds with the 511 keV peak, we know this from the shape of the ^{22}Na spectrum.

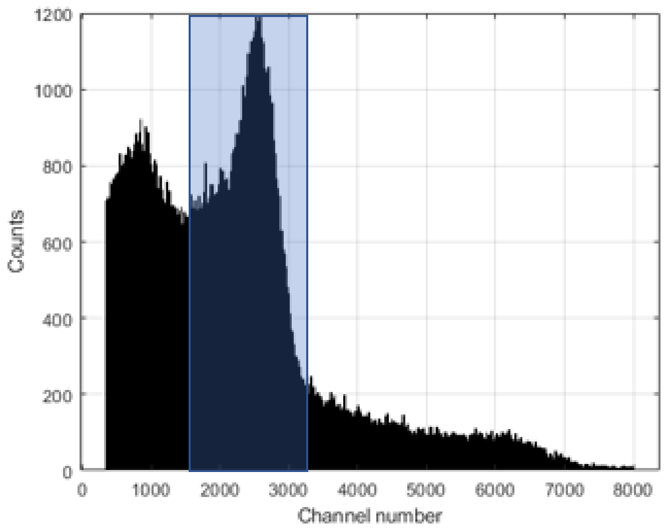

Figure 97: Energy window applied to the obtained spectrum

By selecting the events whose energy lies between that interval, the image is improved, eliminating noise and scatter, as it is shown in **Figure 98**.

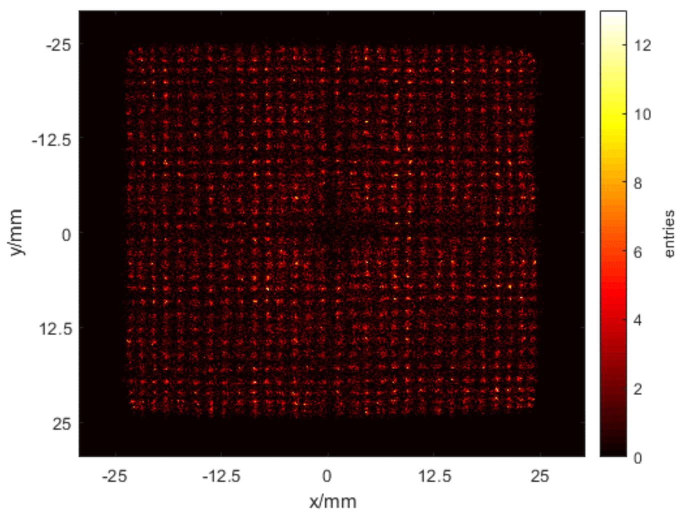

Figure 98: Flood image applying an energy window

It can be seen how the undesired artefacts are eliminated, showing a more homogeneous image and differentiating more easily all the different pixels in the crystal array.

4.2.6 Image improvement using different light guides

With the use of a light guide, the scintillation photons would spread over different die sensors, being detected by a larger number of SPADs and homogenising the resulting flood image. The thickness of the light guide used to improve the image depends on the scintillation crystal used, so different acquisitions were performed with light guides of 1, 2, 3 and 4 mm thickness. To perform these trials, a small scintillator matrix of 10×10 LYSO crystals was used, as the available light guides in the lab had the dimensions of that crystal matrix. Each of the acquisitions were adjusted to their corresponding energy window, as it differed for different light guides, since as they open the light cone, some of the photons are lost, changing the photopeak position. These were the results obtained:

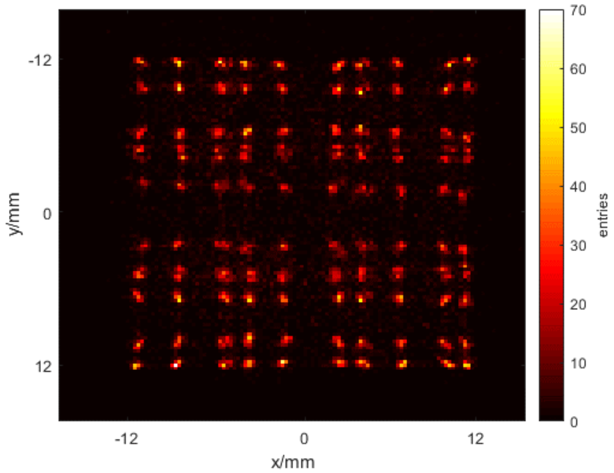

Figure 99: Flood images without light guide

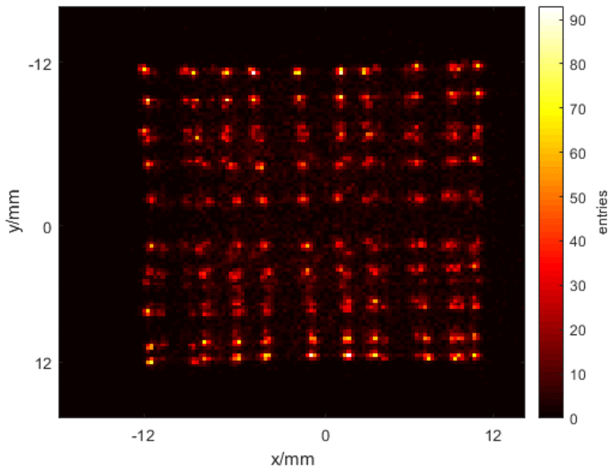

Figure 100: Flood image with 1 mm thick light guide

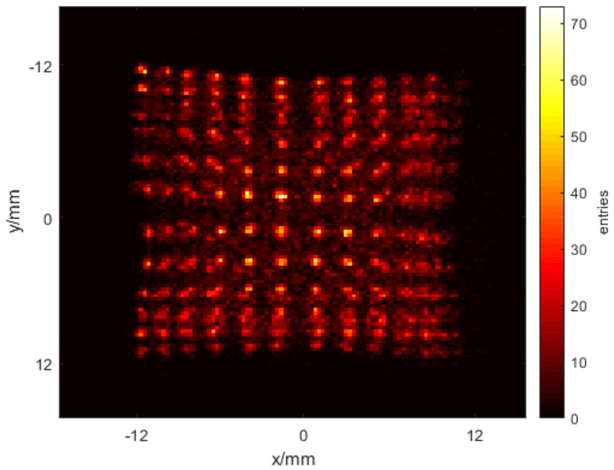

Figure 101: Flood image with 2 mm thick light guide

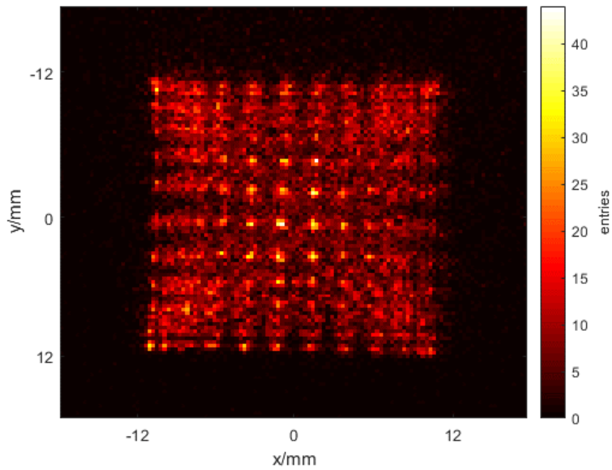

Figure 102: Flood image with 3 mm thick light guide

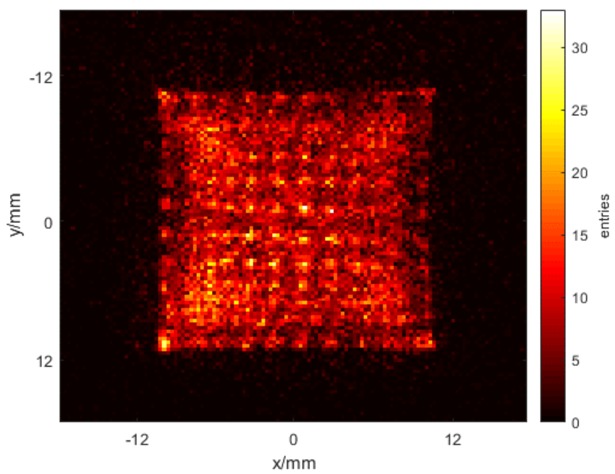

Figure 103: Flood image with 4 mm thick light guide

After comparing all images, the best results were obtained with the 2 mm thick light guide. It represented the most homogeneous image with best resolvability. A same light guide with the same thickness and the proper dimensions was bought to be used on later acquisitions and development of this project.

4.3 New position algorithms

4.3.1 Starting data

Once the acquisition parameters were configured, the time and energy windows were selected, and the proper light guide was used, an acquisition was performed, and the resulting data was analysed. A huge number of files was processed in order to increase the statistics (number of analysed events) to obtain better results. The total number of data frames (see **Figure 79**) analysed was 40,002,379, resulting in a total of 13,008,375 events.

4.3.1.1 Energy spectrum

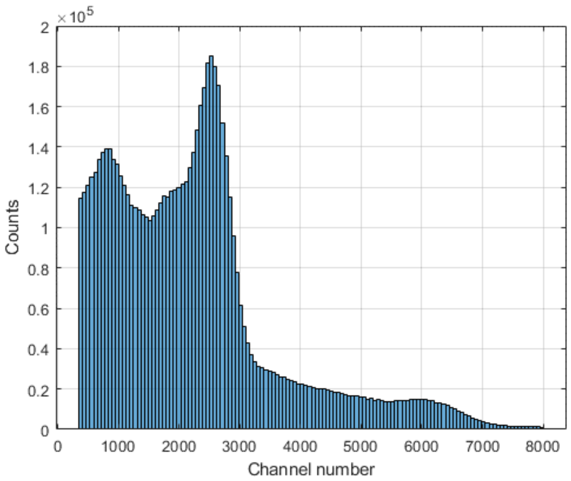

Figure 104: Non-calibrated energy spectrum

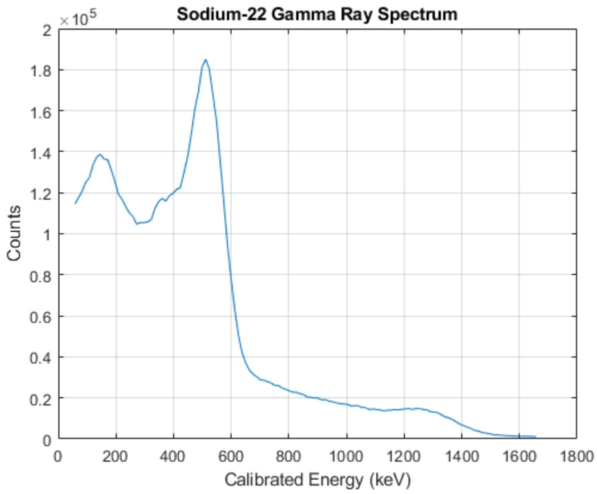

Figure 105: Calibrated energy spectrum

The histogram of **Figure 104** was obtained, but to analyse the results, a linear calibration was performed to give the real energy spectrum of ^{22}Na, as the channel numbers are almost proportional to the energy for this energy range (at higher energies it can be slightly deconfigured). The emission peaks for this radioactive isotope are known to be at 511 and 1275 keV, and they can be seen at the channel numbers 2530 and 6130 in the obtained figure. By performing a linear fitting and obtaining the corresponding equation, the x-axis is calibrated to energy in keV.

4.3.1.1.1 Energy resolution

To study the energy resolution of the detector, we need to calculate the Full Width Half Maximum (FWHM) of the photopeak. The FWHM is equal to the width of the photopeak at the half of its maximum value. For a more precise measurement this value can be computed by adjusting a Gaussian function to the photopeak, obtaining its expected value μ and its variance σ^2.

Then, the FWHM is calculated as:

$$FWHM = 2\sqrt{2ln2}\,\sigma \approx 2.355\sigma \quad (11)$$

Once this value is obtained, the energy resolution is:

$$R_e = \frac{FWHM}{E_p} \times 100 \quad (12)$$

where E_p is the energy at the photopeak (in this case 511 keV).

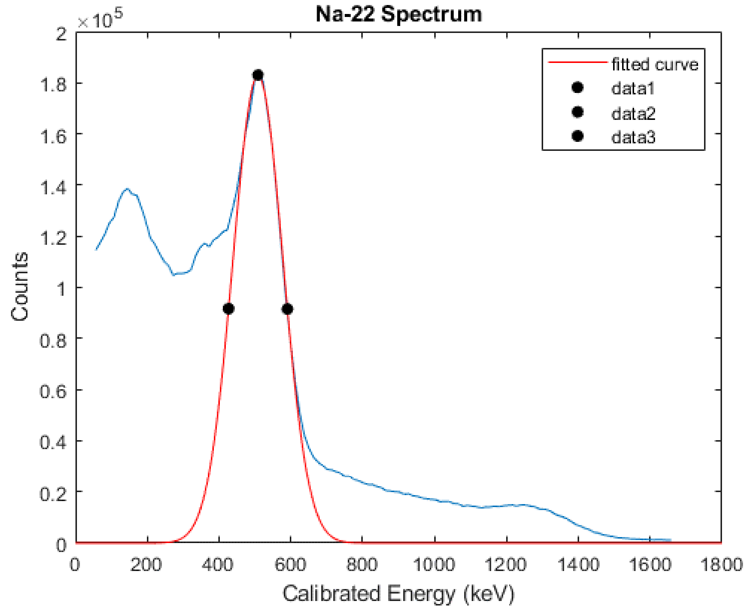

Figure 106: FWHM of the ^{22}Na energy spectrum

The energy resolution obtained was 32.13%, which is a high value, although satisfying, since we are considering the events over the whole array.

4.3.2 First flood field image: all energies

The first flood image was obtained considering all energies, without applying the energy window:

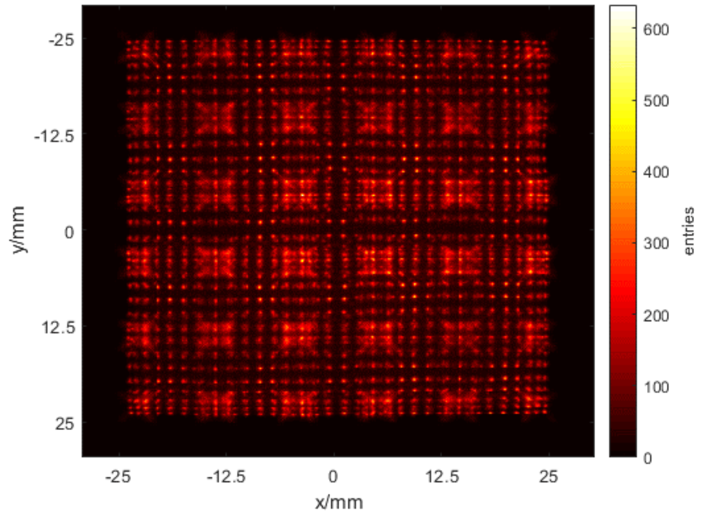

Figure 107: Flood field image considering all energies

A huge number of events were used to generate this image, improving the resulting picture. There is a high accumulation of events in the centre of each die as it is the most sensitive area. At the junctions between dies, there is a dead space making the borders less sensitive, causing the pattern observed in the figure. We use this image as a reference for comparison, to evaluate the improvement on image quality.

4.3.2.1 Spatial resolution

To calculate the spatial resolution, the horizontal and vertical profiles of the flood images were taken. To do so, we draw a line passing through the highest value pixel of each crystal. The same rows and columns were chosen for all images. The horizontal resolution was measured considering the 9th row of crystals, and the vertical resolution, considering the 10th column.

The spatial resolution was calculated in two different ways:

The first one was the valley-to-peak ratio, in which the value of the valleys was divided into the value of the peak. As each peak has two valleys, the final result is the mean of the two resulting values:

$$V/_P = \left(\frac{Left\ valley}{Peak} + \frac{Right\ valley}{Peak}\right)/2 \times 100 \qquad (13)$$

The second one was the resolvability index (RI), in which a Gaussian is fitted to each of the peaks from the profile image, and its FWHM is divided by distance of the peak to the adjacent peaks (D), taken from [48]:

$$RI = \frac{FWHM}{D} \quad (14)$$

To obtain the value of D, there were two cases: if the peak was at an extreme, only the distance to the adjacent one was considered, but if it was between two peaks, the mean distance was calculated.

To differentiate which peaks would correspond to the positions of the crystals discarding noise, the mean average of the profile was set as a threshold. We used these two different measurements because the first one is the most commonly used in literature, but we consider the second one (RI) to be more precise since it also takes into account the distance between pixels.

4.3.2.1.1 Horizontal resolution

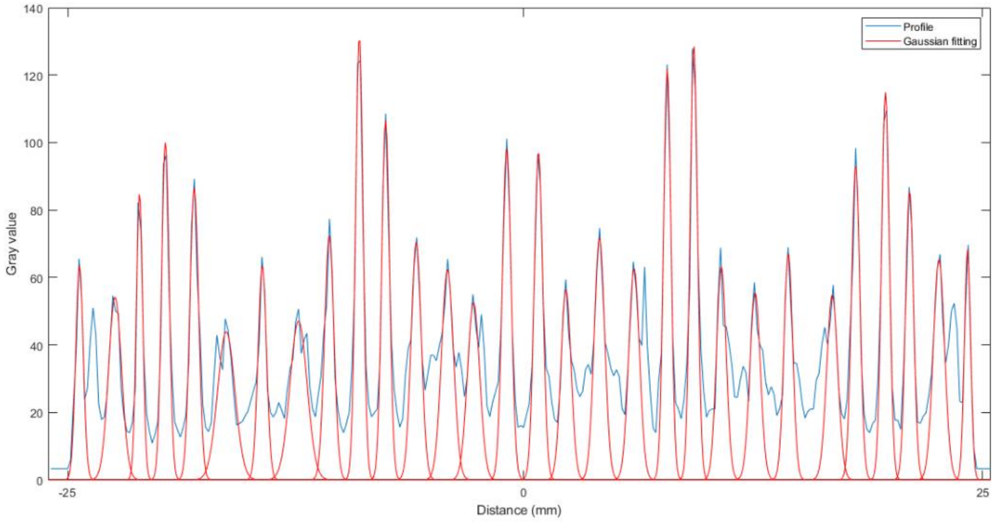

Figure 108: Horizontal profile of the initial image with all the energies and selection of the peaks

The mean V/P ratio of this profile is 43.70%, whereas the mean RI is 0.38. Since false events are considered in the generation of this image, many of the crystal are not resolved in a single peak, but in two or three. This makes the Gaussian fitting wider, as it is impossible to distinguish those pixels, decreasing the resolution, and, in the best case, only one peak is selected discarding the others, as it happens in the first and last peaks.

4.3.2.1.2 Vertical resolution

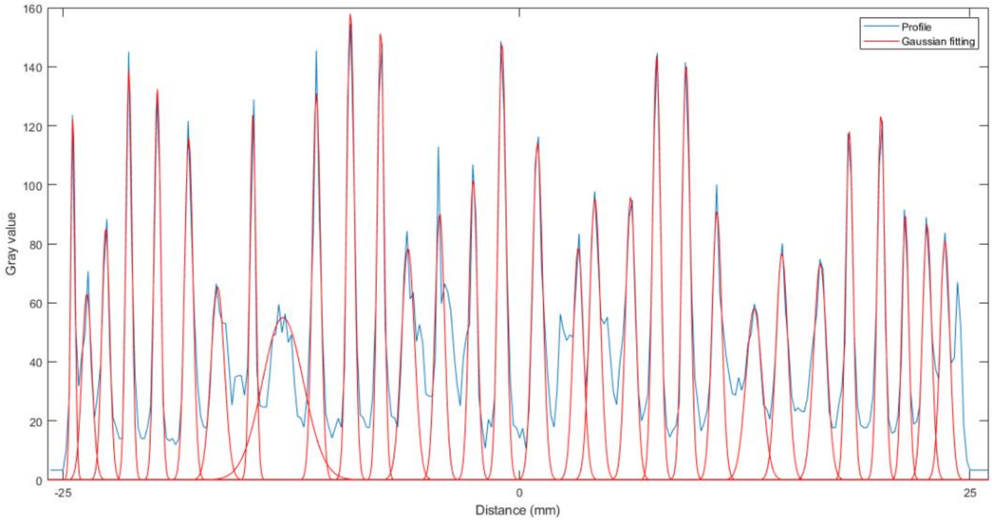

Figure 109: Vertical profile of the initial image with all the energies and selection of the peaks

This profile presents a mean V/P ratio of 36.82% and a mean RI of 0.42, similar to the values above, as both profiles come from the same image. In this picture, the first crystal position is divided in two peaks and since it is impossible to distinguish the pixels, the Gaussian fitting cannot be adjusted properly, augmenting the number of crystals in a column into 31. It does not happen in the last position. The problem of the wider Gaussian fitting because of the division of a crystal in more than one peak is highly visible in the supposed to be the 8th position.

4.3.3 Second flood field image: energy window applied

After the energy window is applied, the image becomes more homogeneous, improving considerably and making it possible to differentiate the positions of each crystal. The false events are eliminated so the high accumulation in the centre of the dies is no longer visible. Although the position of the 30×30 crystals can be distinguished, it still has a lot of noise and scatter, so the image can be further improved.

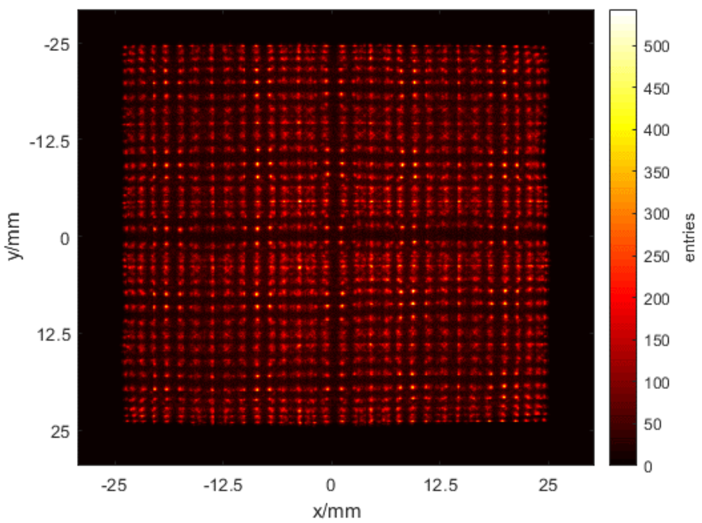

Figure 110: Flood field image applying energy window

4.3.3.1 Spatial resolution

4.3.3.1.1 Horizontal resolution

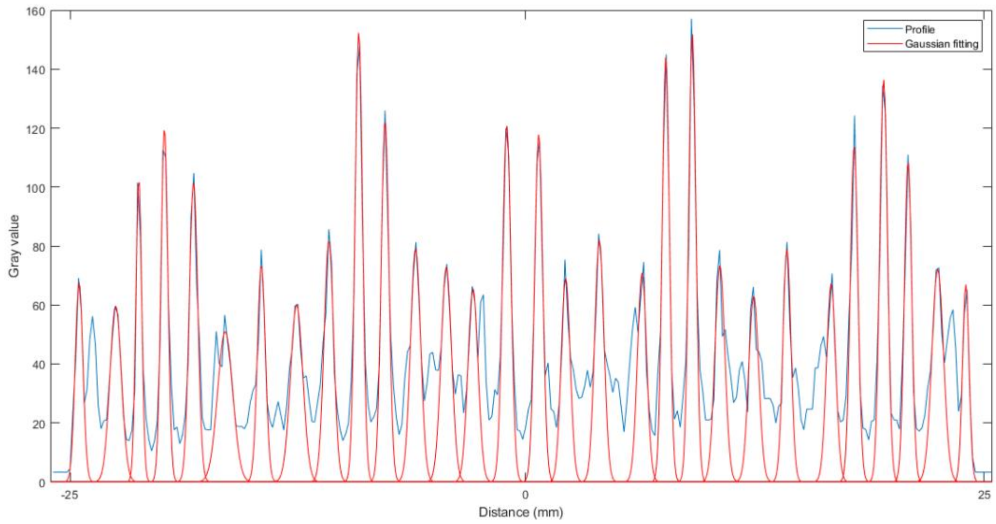

Figure 111: Horizontal profile of the image with the energy window and selection of the peaks

This profile has been slightly improved after the application of the energy window. The mean V/P resolution is 41.61% and the mean RI is 0.35. The profile has not changed too much, and the same problems commented in the previous profile arise.

4.3.3.1.2 Vertical resolution

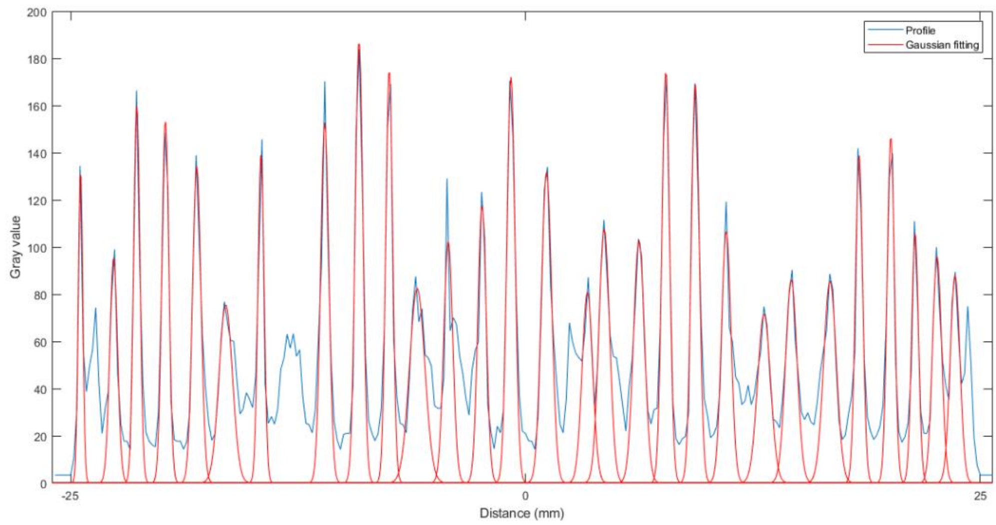

Figure 112: Vertical profile of the image with the energy window and selection of the peaks

The improvement of the resolutions is more noticeable in this vertical profile, obtaining a mean V/P resolution and RI of 30.70% and 0.37 respectively. This time, at the first and last crystal positions, only one peak has been selected, and the position composed of three peaks has not been fitted by a Gaussian. One possible explanation may be that as the noise have been eliminated, the mean value of the profile has increased, and consequently the threshold too, so those peaks have not been recognized.

4.3.4 Third flood field image: 9 higher values

We designed an algorithm that localizes the 9 pixels with the higher photon counts of each event and discards the rest. In this way the pixels with low photon counts belonging to false detections are not considered, as they may not belong to the real event. Those pixels were far away from the centre pixel, and they caused the event to be misplaced obtaining a blurred, noisy image. We applied this algorithm to the image with the energy window, and solved this problem.

One drawback is that the lowest photon counts do not necessarily contribute to false events, as well as the higher ones may contribute to false detections.

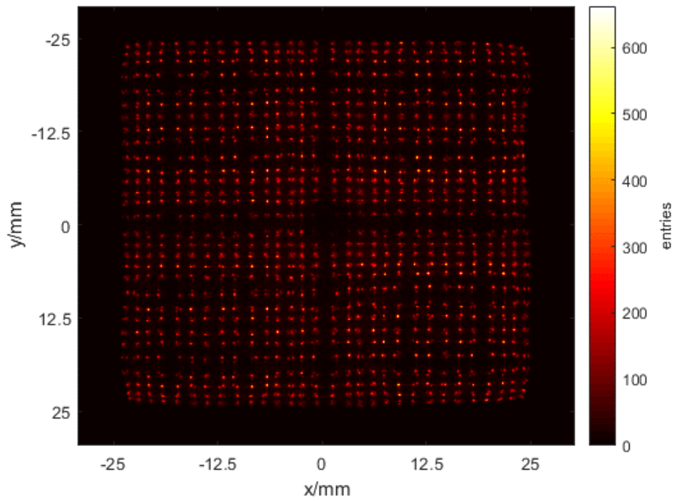

Figure 113: Flood field image applying 9 highest pixels algorithm

4.3.4.1 Spatial resolution

4.3.4.1.1 Horizontal resolution

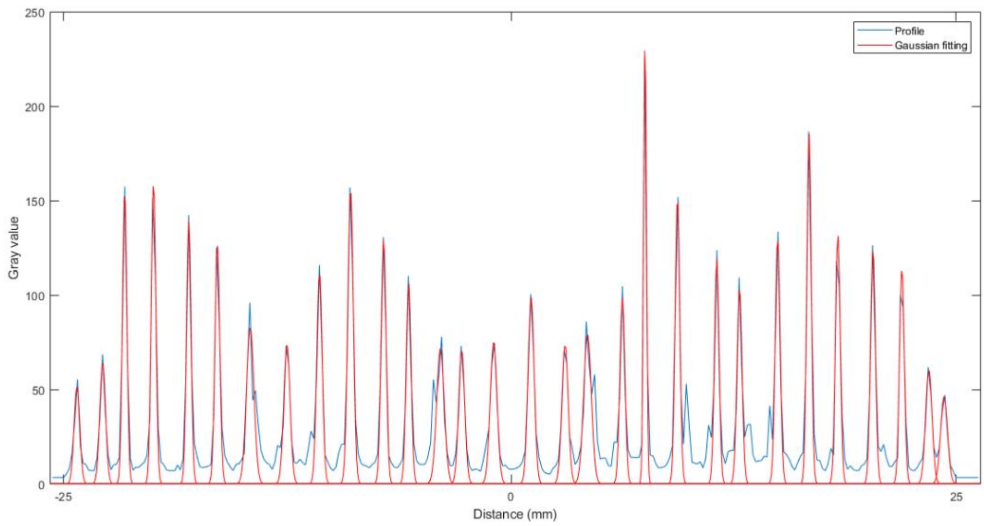

Figure 114: Horizontal profile of the image with 9 highest pixels algorithm

After the application of this algorithm, the mean V/P resolution has decreased considerably, achieving a value of 18.68%. The mean RI has also decreased to 0.23. All the 30 crystal positions are now fitted by their corresponding Gaussians and they can be easily differentiated. As only the highest pixel values of each event are considered, their locations are much more precise. This eliminates much of the noise in the profile and creates steeper peaks. Notice that the background noise in the profile has decreased from a value around 20 to approximately 10.

4.3.4.1.2 Vertical resolution

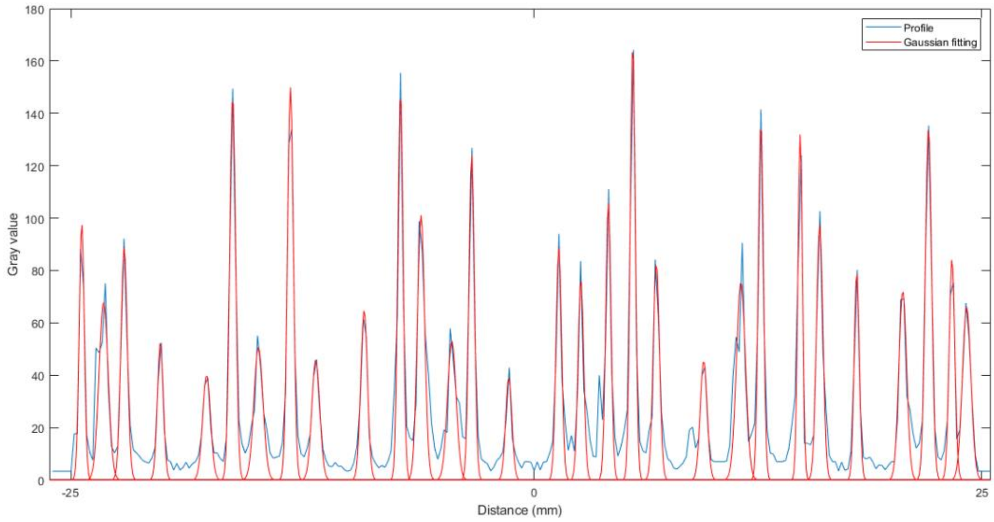

Figure 115: Vertical profile of the image with 9 highest pixels algorithm

The mean V/P resolution of the vertical profile is 18.03% and the mean RI is 0.29. The same arguments as in the horizontal profile can be applied.

4.3.5 Fourth flood field image: main pixel algorithm

Following the same reasoning as in the algorithm of the 9 pixels with highest photon counts, it was considered that if the pixel with the highest photon counts of an event was localized and only the 8 surrounding pixels were considered, discarding the rest, the position of the event would be more precise. This was the procedure followed by the authors of the paper [46].

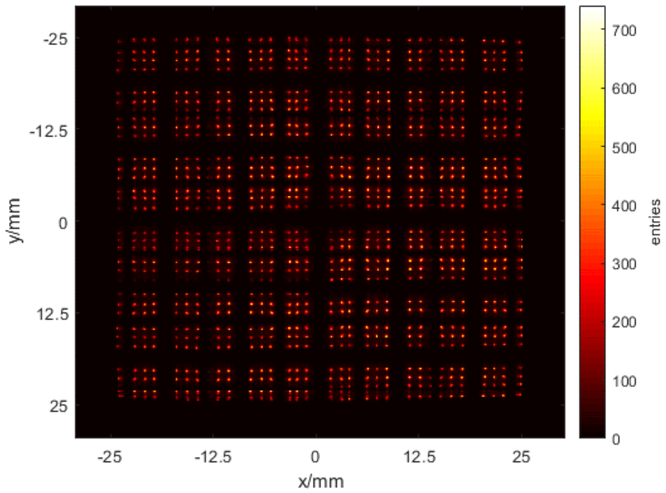

Figure 116: Flood field image applying main pixel algorithm

By applying this algorithm, the 30×30 matrix of crystals can be perfectly differentiated. All the false detections are eliminated, and each event has its correct location. The main drawback of this method is the same that we had at the beginning, but now it happens both in the dies and in the pixels. As the most sensitive part of the detector is the centre of each pixel, the cells with higher photon counts are accumulated at those positions. This is the reason why almost all the detections are localized at the centres of the pixels. In this figure, the visible 3×3 matrix of crystals would correspond to one pixel, and the combination of 4 matrixes would correspond to a die. This problem is very common in this type of research, as many of the images generated have this appearance. Despite of this, the quality of the image obtained is a very good one and it can be considered a great achievement.

4.3.5.1 Spatial resolution

4.3.5.1.1 Horizontal resolution

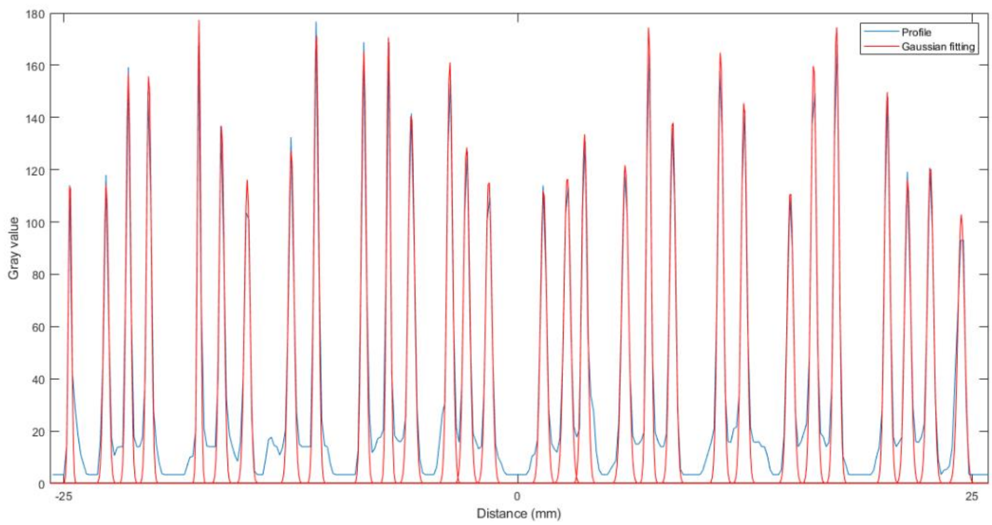

Figure 117: Horizontal profile of the image with main pixel algorithm

By applying this algorithm, the mean V/P resolution has almost halved the one of the previous horizontal profile, obtaining a value of 10.91%. However, the mean RI has kept the same: 0.23. The truth is that the previous mean RI was a very good value, so it does not matter that it has not decreased. By looking at the profiles, all the 30 peaks can be very well resolved, being very steep, homogeneous and very well fitted by Gaussians. The previous discussion about the accumulation of events at the centre of the pixels are the reason why the peaks are grouped into sets of 2 or 3.

4.3.5.1.2 Vertical resolution

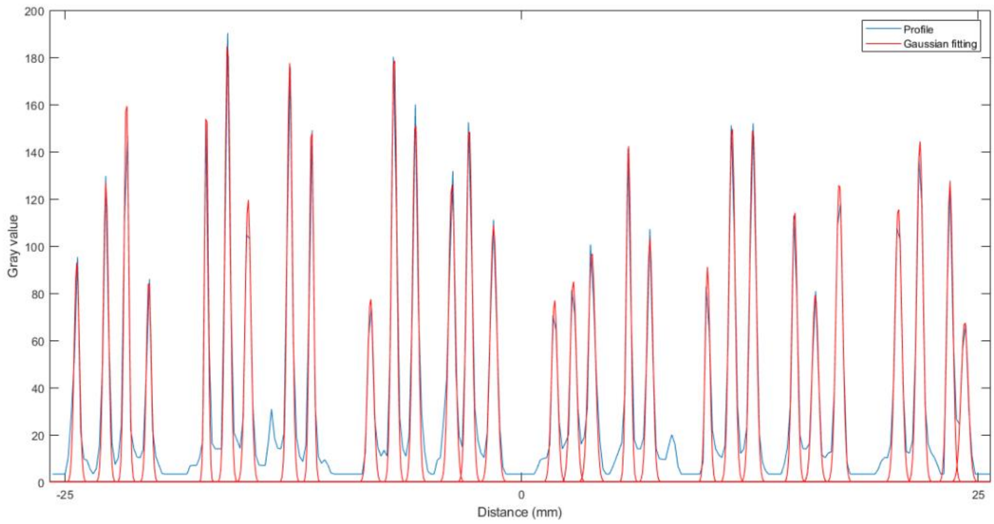

Figure 118: Vertical profile of the image with main pixel algorithm

In this vertical profile we can draw the same conclusions as with the horizontal one. The mean V/P resolution has decreased to 12.83%, and this time, the mean RI has also decreased to 0.26.

4.3.6 Fifth flood field image: main pixel algorithm with a mask

Although the previous image was very good and satisfactory, it could be further improved. We designed a mask so that all the pixels of the image lying below a certain threshold would be set to zero. This way, only the positions with a higher number of events detected were considered, reducing noise. After several tries, we decided to set a threshold of 70 entries, as it was the minimum under which all the pixels could be perfectly separated in order to later analyse the image (section 4.4). This image was perfect for us, even better than the one set as a reference at the beginning (**Figure 87**).

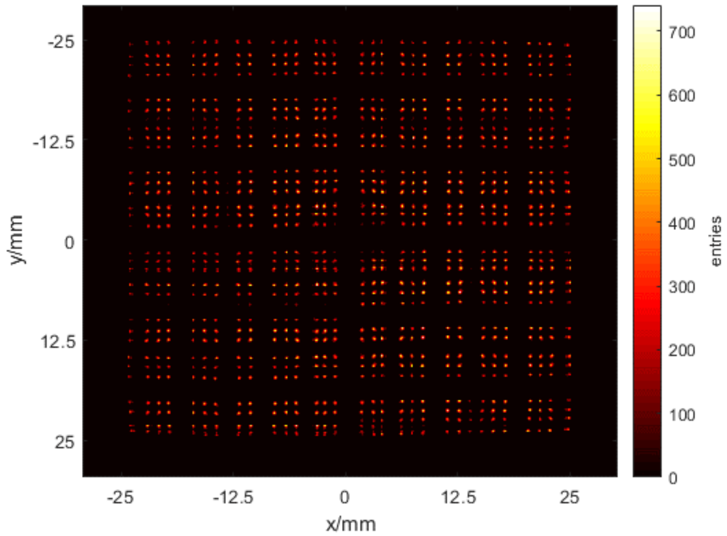

Figure 119: Flood field image applying main pixel algorithm with a mask

4.3.6.1 Spatial resolution

4.3.6.1.1 Horizontal resolution

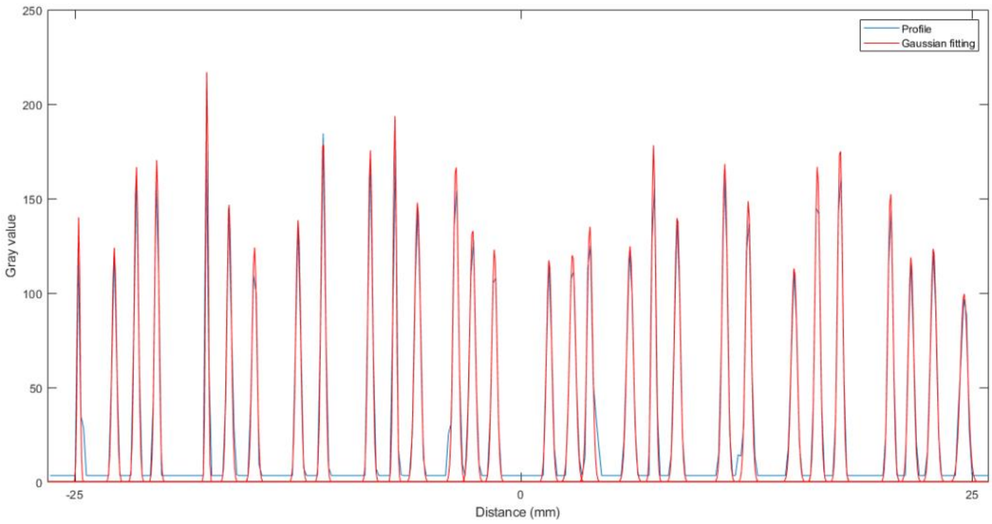

Figure 120: Horizontal profile of the image with main pixel algorithm with a mask

With the mask, all the noise has been set to zero, so the peaks are now perfectly resolvable and fitted obtaining a mean V/P resolution of 3.59 %, the lowest value achieved. It has the same effect on the mean RI, with a value of 0.21. The resulting horizontal profile is highly similar to the previous one, but the application of the mask improves the image.

4.3.6.1.2 Vertical resolution

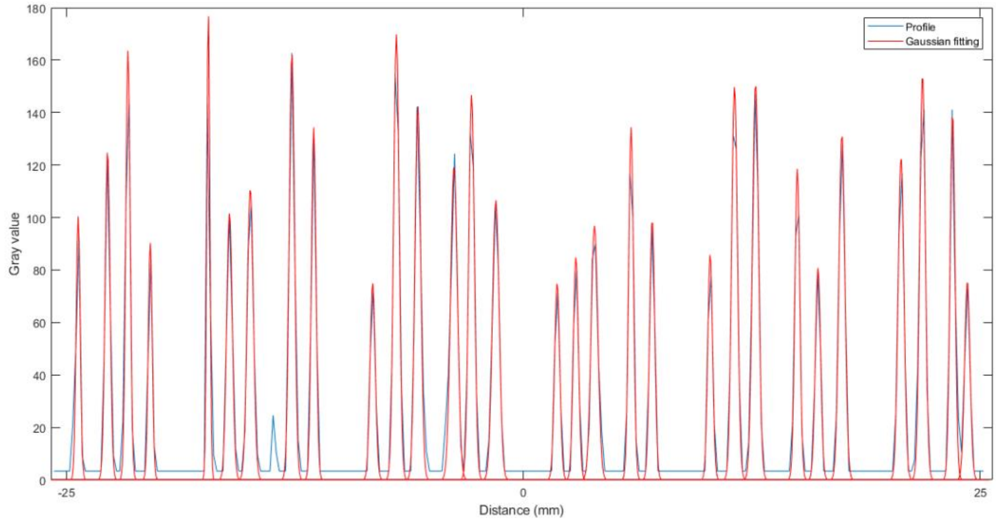

Figure 121: Vertical profile of the image with main pixel algorithm with a mask

The vertical profile follows the same trend as the horizontal one. The mean V/P resolution achieved is 5.03% and the mean RI, 0.25, the lowest values obtained.

4.4 Analysis of the definitive image

Once the definitive flood field image was obtained, the next step was analysing it pixel by pixel. As the scintillator matrix is formed by 30×30 crystals. Each of them is supposed to show the energy spectrum of ^{22}Na since every single crystal converts individually the gamma radiation from the isotope into light photons. As the false detections (caused by noise and scatter) that distorted the energy and position of each event were eliminated, the resulting spectra were expected to be nicer, more accurate and with a better resolution than the one of **Figure 105**.

4.4.1 Considering only the photopeak (energy window applied)

In this case, the expected spectra would show only the photopeak, as the rest of the energies were eliminated with the energy window.

It did not make sense to analyse individually each crystal, since there is a total number of 900, so a section of 3×3 crystals was selected.

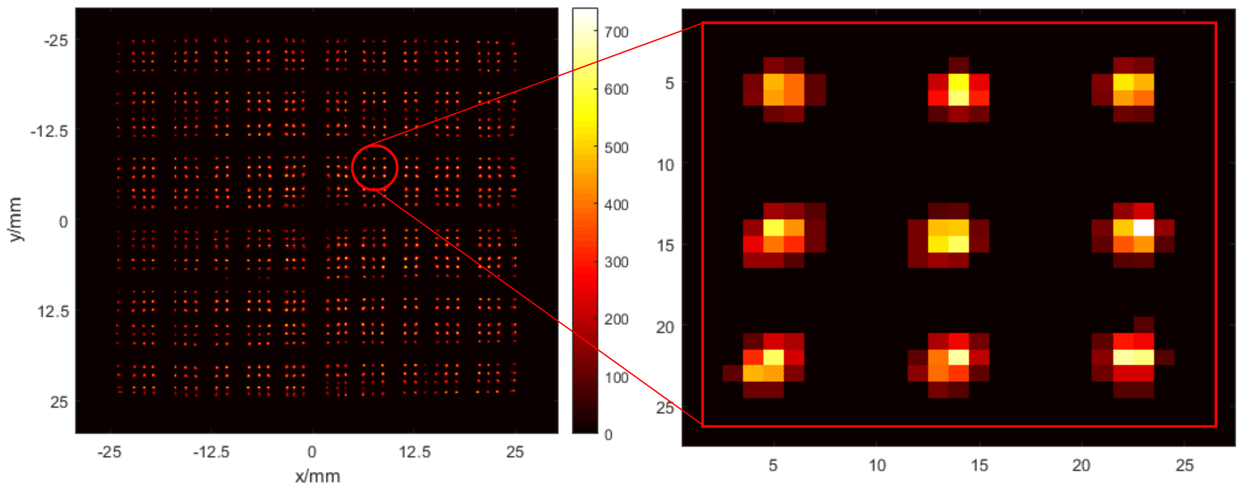

Figure 122: Selection of the 3x3 matrix of crystals to analyse

After that, so as to select the 9 crystals, a threshold was set so that they could be properly differentiated and that there is no noise in the image. The selected threshold was 70 entries (as explained in section 4.3.6). The crystals were labelled from 1 to 9, being 1 the upper left crystal, 2, the bottom one, and so on.

Nine different energy vectors were created, one for each crystal. Since the energy and location of each event was stored, the program ran through each of the 13,008,375 events (position and energy) with the following condition: if the event is detected in one of the 9 crystals, its energy would be stored in its corresponding energy vector.

The next step was to represent the energy spectrum of each crystal:

As expected, only the the photopeak of the ^{22}Na was represented, as by applying the energy window,the rest of the energies were not considered.

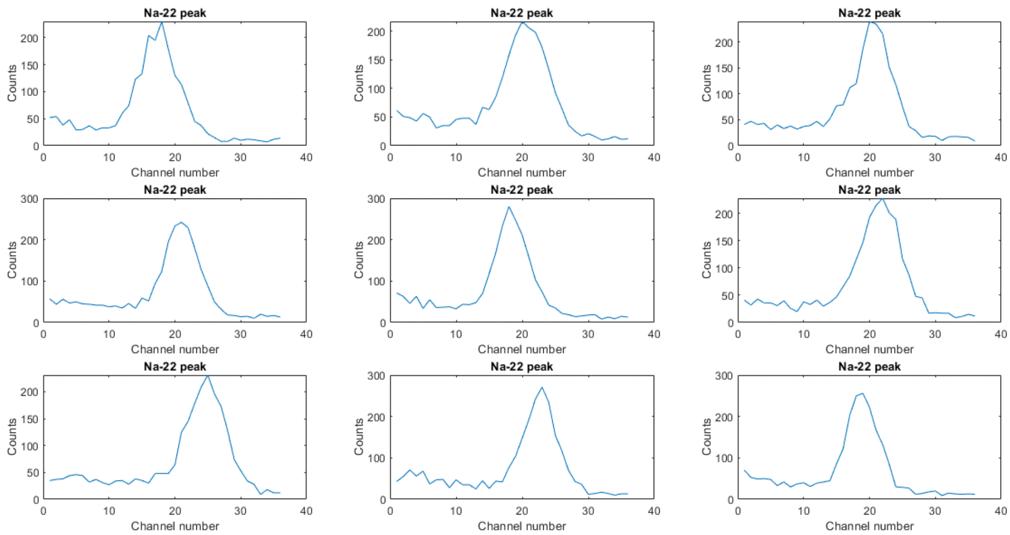

Figure 123: Energy spectra of the 9 selected crystals (with energy window)

As we were interested on analysing the ^{22}Na spectra of the crystals, we generated the same flood field image but considering all the energies.

4.4.2 Considering all energies (energy window not applied)

In order to obtain the total energy spectrum of ^{22}Na, all the energies should be considered. The same procedure as in the preious section was followed, obtaining a flood image with the main pixel algorithm, but this time, the energy window was not applied.

We applied a mask to separate and label the 9 crystals, setting the false events caused by dark counts to zero.

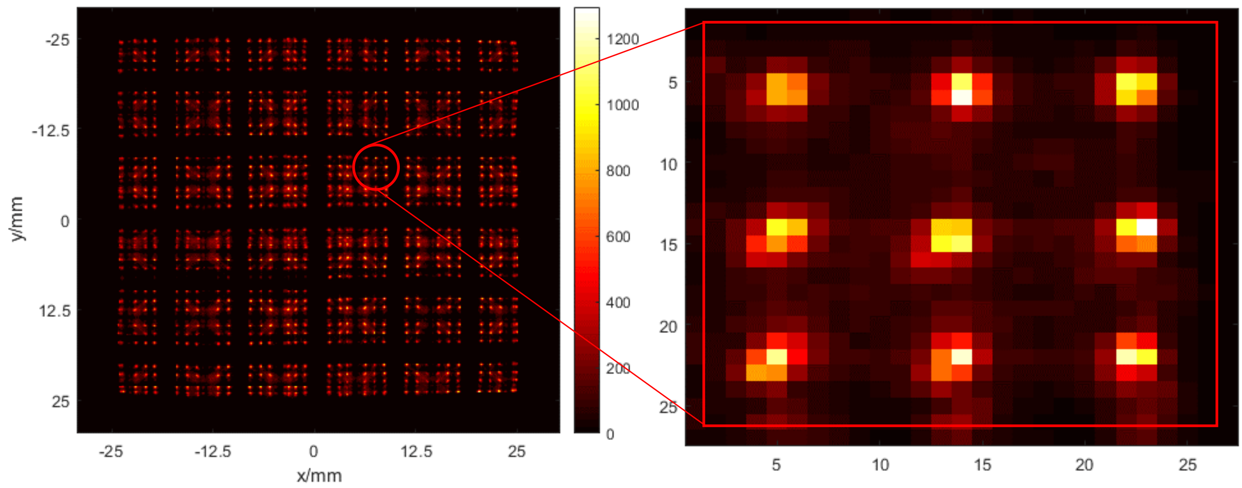

Figure 124: Selection of the 3x3 matrix of crystals to analyse considering all energies

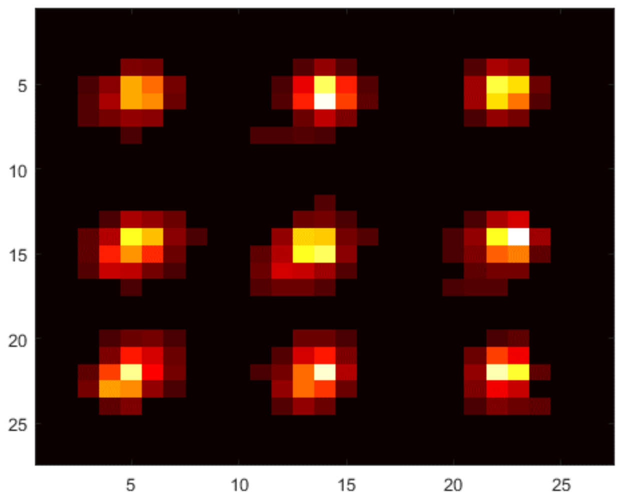

Figure 125: 3x3 matrix of crystals considering all energies with mask

Following the same procedure as in section 4.4.1, the energy spectra of ^{22}Na was generated for each of the 9 crystals. To analyse how good the results are, the energy resolution and the FWHM were calculated by fitting a Gaussian to each of the photopeaks. The procedure was the same as the one followed in section 4.3.1.1.1, using the equations (11) ans (12).

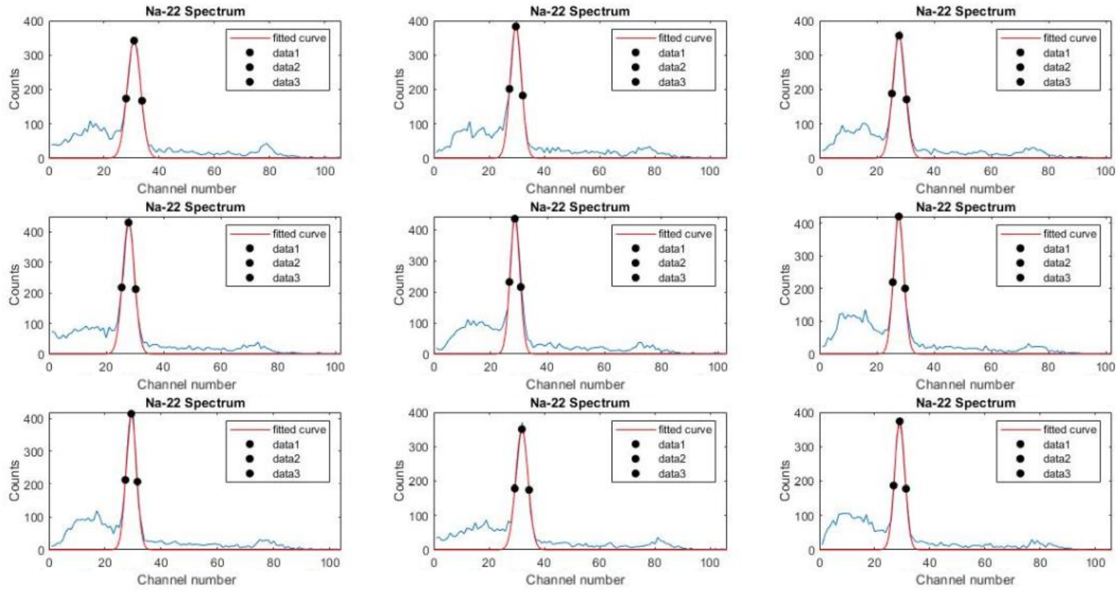

Figure 126: Energy spectra of the 9 selected crystals (without energy window)

These energy spectra can be properly differentiated resembling the one of **Figure 74**, as explained in section 4.4.

The energy resolutions obtained are collected in the following table:

Crystal 1	Crystal 2	Crystal 3	Crystal 4	Crystal 5	Crystal 6	Crystal 7	Crystal 8	Crystal 9
18.06%	15.02%	18.31%	17.50%	14.07%	15.33%	14.48%	16.30%	13.81%

Table 7: 9 selected crystals energies resolutions

The energy resolution achieved with this detector is the mean of the resolutions achieved in the 9 crystals: 15.87%.

5 DISCUSSION AND CONCLUSSIONS

5.1 Dark Count Map

Comparing the initial and final DCMs, there is no doubt that the performance of que detectors has been highly improved.

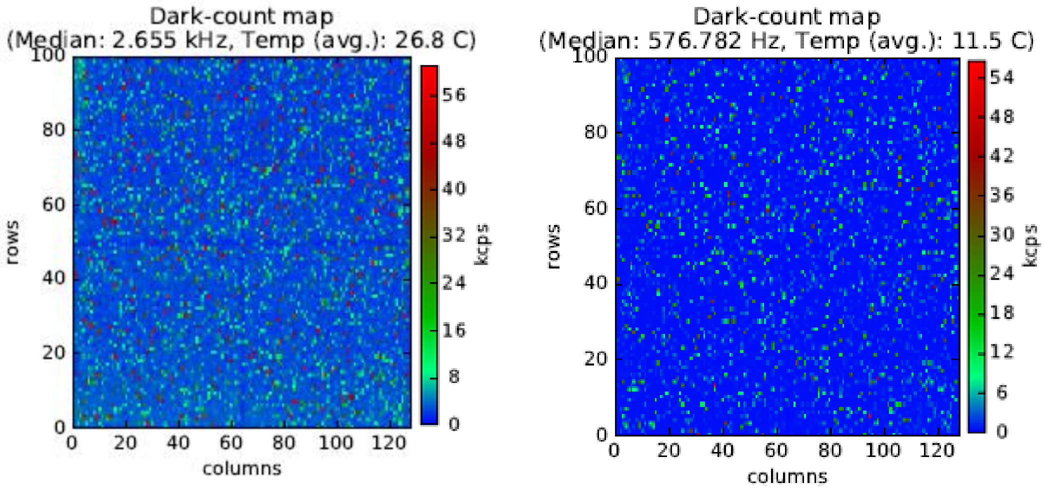

Figure 127: Comparison of initial and final DCMs

With the use of the cooling system (decreasing and maintaining constant the temperature) and increasing the number of frames per cell, the mean dark count rate of the SPADs has decreased considerably, enhancing the sensor efficiency. This is visible in two aspects. The first one is the images themselves, where the red and green dots representing high kcps decrease considerably and a majority percentage of dark blue dots (0 kcps) predominates. The second one is the median of the dark count rates, which has changed from 2.655 kHZ to 576.782 Hz, decreasing 4.6 times its value and improving 78.28% its efficiency.

$$\eta_{sensor} = \frac{2.655\ kHz - 576.782\ Hz}{2.655\ kHz} \times 100 = 78.28\%$$

Taking these arguments into consideration, we can state that the performance of the system has been improved.

5.2 Flood field images

After selecting the proper acquisition parameters, time window and light guide, different algorithms were applied to the image to improve it. Here we present a comparison of the initial image (considering all the incoming events with any energy), and the final one (taking into account only the events of interest, discarding the ones produced by dark counts or any other source of error).

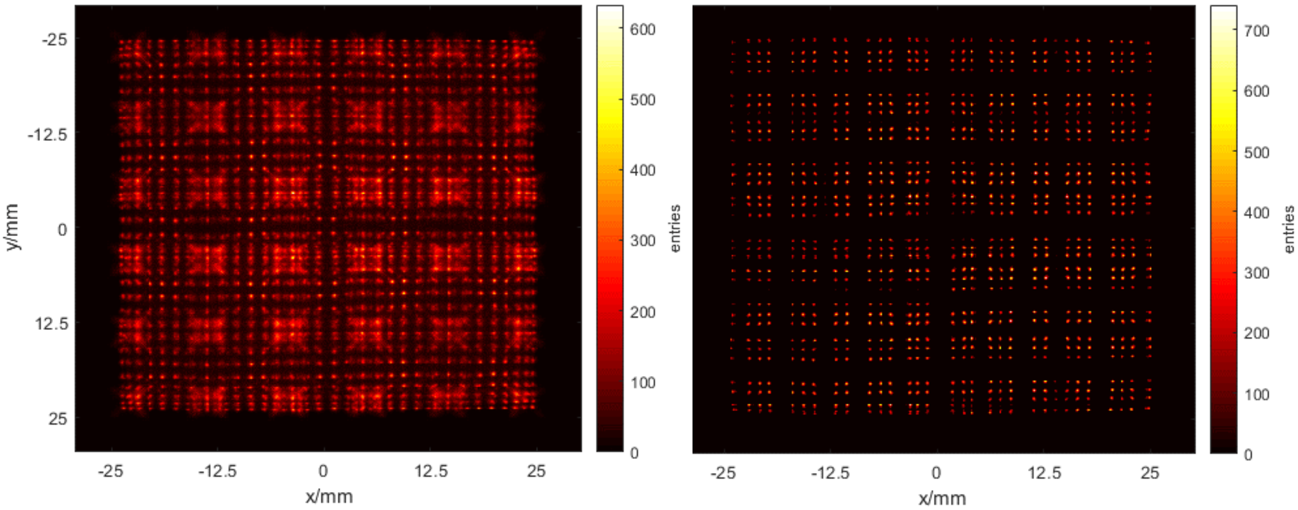

Figure 128: Comparison of initial and final flood field images

The improvement in image quality after applying the correction algorithms is clearly visible. Noise, scatter and false detections have been eliminated and only the true events are considered. All the 900 crystal positions can be well differentiated.

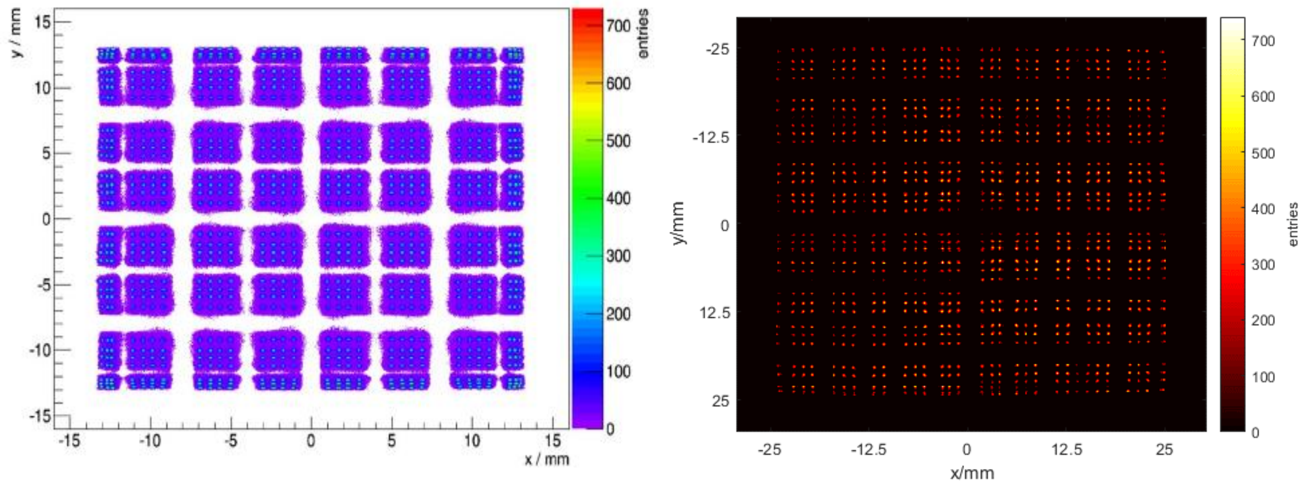

Figure 129: Comparison of the flood field image set as objective [46] and the obtained one

The left image is the one set as reference from the beginning. Comparing these two images we can conclude that the objectives of this work have been highly accomplished.

5.2.1 Spatial resolution

Considering the horizontal profile, the initial and final images also show the huge difference in spatial resolution. In the former, the peaks are not very well distinguished, as some of the crystals have double or triple peaks for the reasons explained in section 4.3.2.1.1. In the later, this problem is solved, being able to distinguish all the 30 crystals without any difficulty.

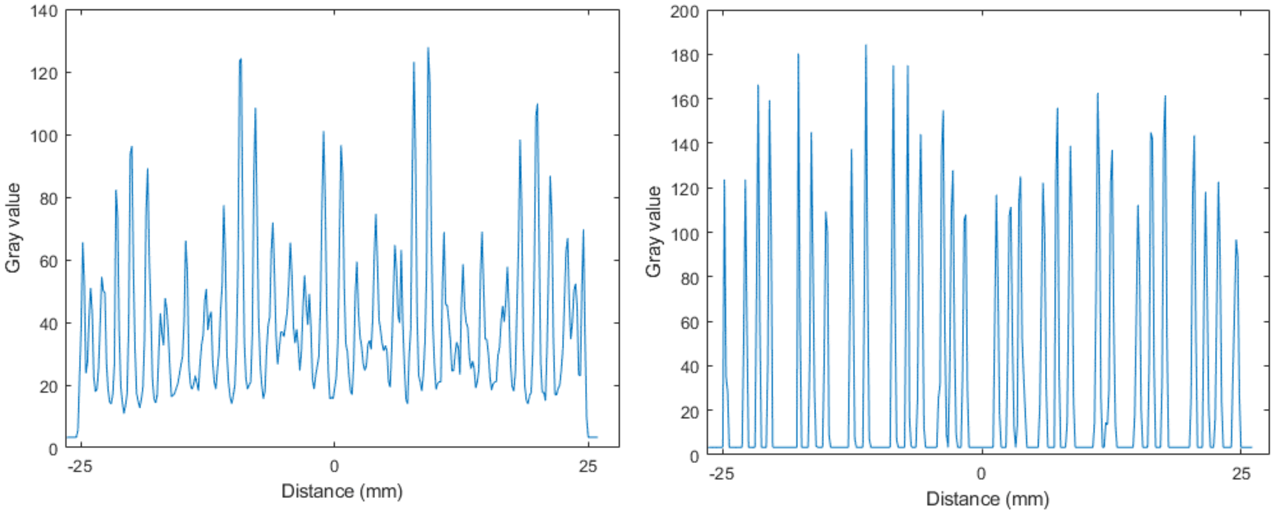

Figure 130: Comparison of the horizontal profiles of the initial and final flood images

Although the disposition of the crystals is less homogeneous in the final profile (see section 4.3.5.1.1), the resolvability of the peaks and the spatial resolution is better in the final image.

Figure 131 represents how the mean V/P resolution and mean RI have been improved for each algorithm, decreasing from 43.70% and 0.38, to 3.59 % and 0.21 respectively. This improvement so abrupt in the V/P ratio and not so much in the RI is the reason why we used two different metrics, as the RI is much more robust than the V/P resolution.

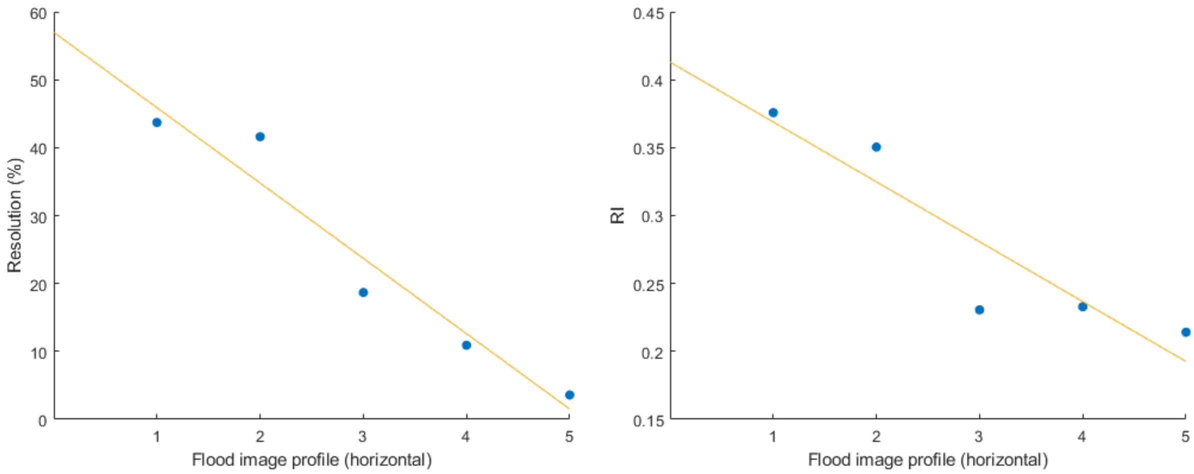

Figure 131: Evolution of the mean V/P resolution and mean RI of the horizontal profiles after each algorithm

Each time a new algorithm has been applied, these values have improved, as can be seen in the decreasing trend line. The difference between the resolutions of the first and last images is quite significative.

Considering the vertical profile, the same discussion can be formulated, as the comparison of the profiles in **Figure 132** resembles the one of the horizontal ones in **Figure 130**.

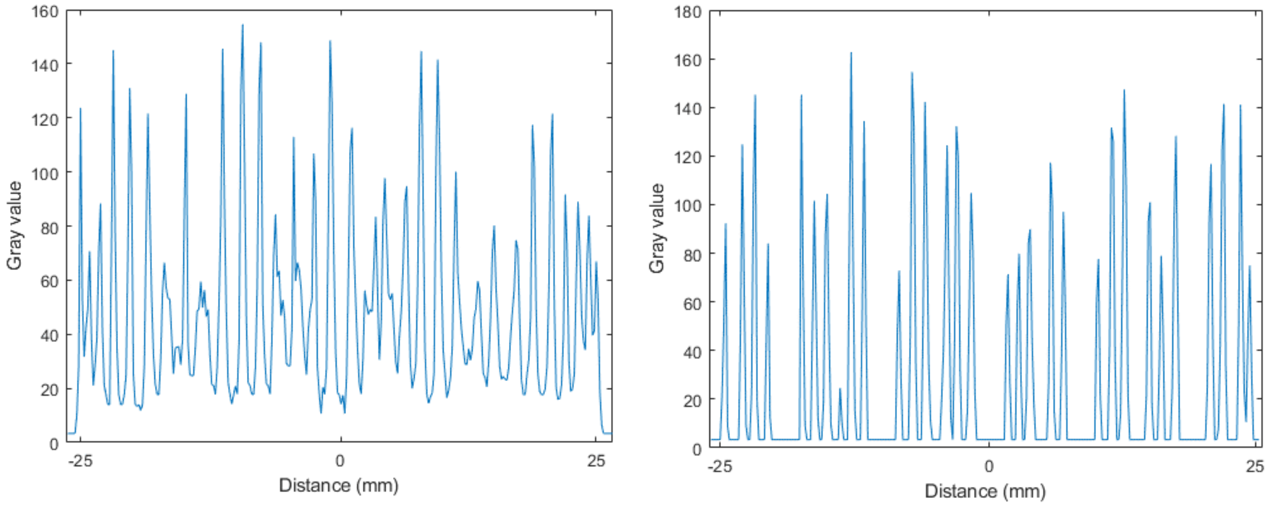

Figure 132: Comparison of the vertical profiles of the initial and final flood images

The mean V/P resolution and the mean RI evolution over the different algorithms is shown in **Figure 133**.

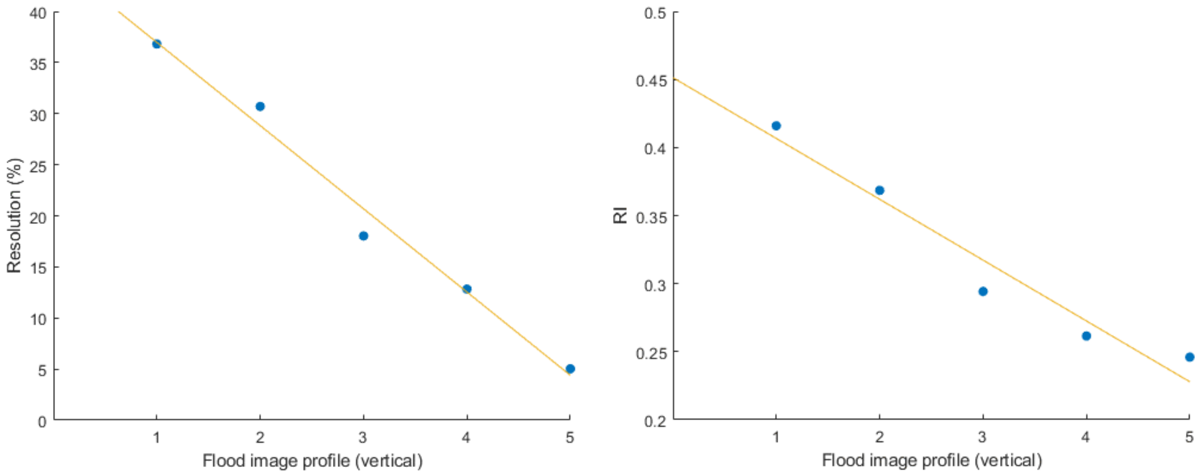

Figure 133: Evolution of the mean V/P resolution and mean RI of the vertical profiles after each algorithm

These values have also followed a decreasing trend from 36.82% and 0.42 to 5.03% and 0.25, respectively. They also explain the robustness of the RI compared to the V/P ratio.

5.3 Energy resolution

The energy resolution achieved with this detector is 15.87% (mean of the resolutions achieved in the 9 individual crystals: see **Table 7**), half the value we obtained considering the events over the whole array (32.13%).

Figure 134 represents a comparison of the ^{22}Na spectrum considering the whole array and the ones considering the individual crystals.

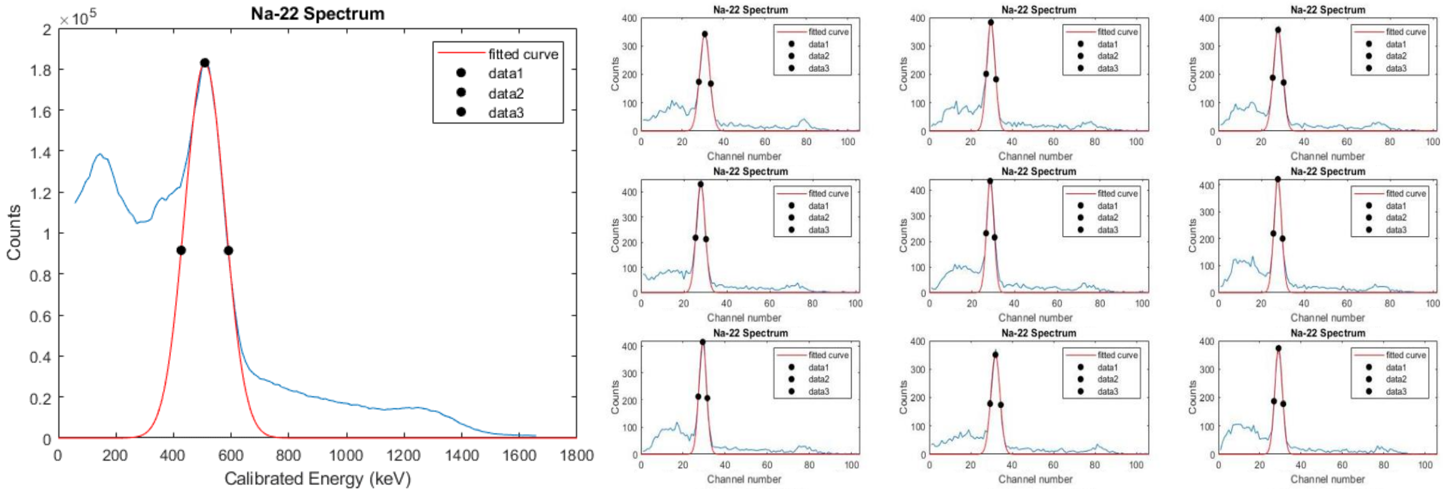

Figure 134: Comparison of the energy spectrum of the whole the detector and of the individual crystals

The peak at the left of the photopeak is caused by noise and scatter events. The individual crystals do not have those energies, as they have been eliminated with the positioning algorithm.

To evaluate the results of this project, we will compare the obtained energy resolution with the ones achieved with the systems described in the section 1.4 (state-of-the-art).

Hyperion II^{D}	12.7% [20]
Vereos PET/CT	11.1% [23]
INSERT	14.0% [26]
EXPLORER total-body PET	11.7% [27]

Table 8: Energy resolutions collected in the state-of-the-art

After analysing their results, we can state that the obtained energy resolution is a success. It is slightly higher than the ones of these projects, but it is a very good result considering the characteristics of this detector and the scintillator crystals used. By applying an energy correction, this resolution would be even improved.

5.4 Final conclusions

Finally, we can conclude that the objectives set at the beginning of this work have been accomplished. We have determined the optimal configuration of the acquisition parameters. We have acquired a clean ^{22}Na spectrum with a good energy resolution. And we have developed an optimal algorithm to obtain a high-quality flood field image with good spatial resolution.

Given the good results obtained, we could consider replacing the analog SiPMs used in the lab by the digital SiPM detectors studied in this thesis for small-animal PET imaging. We have proven their good performance in terms of spatial and energy resolution. Indeed, there is still a lot of work to do with these detectors. If we keep on working with them, we would save a lot of time and would end up having state-of-the-art results. Digital technologies are revolutionizing medicine, and now is the moment to take a step forward and keep on working with digital SiPM detectors to improve medical imaging and the early diagnosis of some diseases.

6 FUTURE WORK

As we have obtained the ^{22}Na spectra of the individual crystals, the next step would be to apply an energy correction to improve the flood field image and the detector energy spectrum.

Since we were able to acquire very good results with the PDPC we attempted to place two detectors in front of each other and capture only the coincident events, simulating a PET scanner. This would have allowed us to generate tomographic images and improved, as well as the flood fields obtained by making use of the electronic collimation provided by coincident events. We tried this experiment, but unfortunately, two tile sensors on one of the DPC modules were damaged while handling them, so the detector was no longer working. We asked Philips for their support to solve this problem, and the solution they gave us was to send the defective module to their headquarter in Germany. This took several weeks, and once the detector came back, we started working with the coincidence detectors, but realised that in order for them to work properly a TDC calibration is required. This TDC calibration is not a trivial matter, it requires a lot of time and study, for that reason it is outside of the scope of the current work and will be left for future works.

Once the previous test is completed, a rotatory stage can be placed in the centre of the detectors in order to reconstruct a 3D PET image, by rotating the sample we can simulate detectors placed in different angles, covering the whole 360 degrees. All the material needed for this experiment has already been bought, but as we could not calibrate both sensors, this work was not performed. This would be the second step of a future work.

7 BUDGET

This section describes an estimation of the cost of realization of this project. We have to consider not only the material costs, but also the hours that the engineers and personnel have dedicated to this work.

1. Autor: Alejandro Canales Barroso

2. Department: Bioengineering and aerospace engineering

3. Description of the project:

Title	Implementation and characterization of radiation detectors based on SiPM for medical imaging
Duration	4 months
Indirect costs rate	20%
Industrial Benefit (IB)	6%

4. Budget breakdown:

Personnel costs

Category	Euros/hour	Total hours	Costs
Senior engineer (director)	35	15	525.00 €
Senior engineer	30	100	3,000.00 €
Junior engineer	20	420	8,400.00 €
Laboratory technician	25	5	125.00 €
Manager	25	5	125.00 €
		Total	**12,175.00 €**

Total personnel costs

Personnel costs	12,175.00 €
Indirect costs	2,435.00 €
Industrial benefit	730.50 €
Total	**15,340.50 €**

Material costs

Description	Price	Approximate duration (years)	Time used (years)	Units	Costs
PDPC	24,000.00 €	10	0.33	1	792.00 €
Reparation of a module	2,600.00 €	-	-	1	2,600.00 €
Cooling system (Thermocube)	2,800.00 €	10	0.33	1	92.50 €
Cold plates	161.00 €	-	-	2	322.00 €
Aluminum plate	15.00 €	-	-	2	30.00 €
Scintillators 30×30 matrix 10×10 matrix	 600.00 € 200.00 €	 10 10	 0.33 0.33	 2 1	 20.00 € 7.00 €
Light guides 50×50 mm 12×12 mm	 24.00 € 12.00 €	 - -	 - -	 2 1	 48.00 € 12.00 €
Tubes and connections	15.00 €	-	-	1	15.00 €
3D printer	3,000.00 €	10	0.2	1	60.00 €
Material	18.00 €	-	-	1	18.00 €
Radioisotpe	73.00 €	5	0.33	1	5.00 €
Optical breadboard	305.00 €	10	0.33	1	10.00 €
				Total	**4,031.50 €**

In order to evaluate the material costs, we have considered that the time dedicated to this project is much shorter than the mean total life of some of the systems, so we have performed some calculations to obtain the cost of the total use of these products.

Costs summary

Total personnel costs +21% IVA	18,562.00 €
Material costs +21 % IVA	4,878.12 €
Total budget	**23,440.12 €**

8 BIBLIOGRAPHY

[1] W. G. Bradley, “History of Medical Imaging,” 2008.

[2] “Medical Imaging | FDA.” [Online]. Available: https://www.fda.gov/radiation-emitting-products/radiation-emitting-products-and-procedures/medical-imaging. [Accessed: 24-May-2019].

[3] M. Abella and M. Desco, “Instrumentation and Multimodality imaging.”

[4] S. R. Cherry, J. A. Sorenson, and M. E. Phelps, *Physics in Nuclear Medicine, ; 2012*. 2012.

[5] “Introduction to PET Physics: The physical principles of PET.” [Online]. Available: http://depts.washington.edu/nucmed/IRL/pet_intro/intro_src/section2.html. [Accessed: 24-May-2019].

[6] Josh Nunez, “What Is "Time of Flight" PET Scanning?,” *Nov 3, 2017*. [Online]. Available: https://info.blockimaging.com/what-is-time-of-flight-pet-scanning. [Accessed: 25-May-2019].

[7] Hamamatsu Photonics, “Photomultiplier Tubes,” *Exp. Methods Phys. Sci.*, 2013.

[8] “PET Project - ift.” [Online]. Available: https://wikihost.uib.no/ift/index.php/PET_Project. [Accessed: 25-May-2019].

[9] J.-M. Regis, “Fast Timing with LaBr 3 (Ce) Scintillators and the Mirror Symmetric Centroid Difference Method,” *PhD thesis*, vol. 3, 2011.

[10] S. Cherry, J. Sorenson, and M. Phelps, *Physics in Nuclear Medicine*. 2012.

[11] G. F. Knoll and H. W. Kraner, “Radiation Detection and Measurement,” *Proceedings of the IEEE*. 1981.

[12] H. Si and S. Pin, “Si photodiodes 2 22,” *Current*.

[13] P. Merken and R. Vandersmissen, “Dark Current and Influence of Target Emissivity,” *Photonics Imaging Technol.*, 2016.

[14] A. Ghassemi, K. Sato, and K. Kobayashi, “MPPC,” 2017.

[15] “What is an SiPM and how does it work? | Hamamatsu Photonics.” [Online]. Available: https://hub.hamamatsu.com/jp/en/technical-note/how-sipm-works/index.html. [Accessed: 29-May-2019].

[16] A. Schmitz, “Integrated Arrays of Digital SiPM’s: the next solid state revolution?,” 2011.

[17] T. Frach, A. Thon, B. Zwaans, C. Degenhardt, and R. de Gruyter, “Digital Silicon Photomultiplier - System Architecture and Performance Evaluation,” *slides from NDIP 2011*, 2016.

[18] J. J. Vaquero and P. Kinahan, “Positron Emission Tomography: Current Challenges and Opportunities for Technological Advances in Clinical and Preclinical Imaging Systems,” *Annu. Rev. Biomed. Eng.*, vol. 17, no. 1, pp. 385–414, 2015.

[19] “Philips - Vereos PET/TCDigital.” [Online]. Available: https://www.philips.es/healthcare/product/HC882446/vereos-pettc-digital-el-primer-pettc-digital-del-mundo. [Accessed: 31-May-2019].

[20] P. Hallen *et al.*, “PET performance evaluation of the small-animal Hyperion IID PET/MRI insert based on the NEMA NU-4 standard,” *Biomed. Phys. Eng. Express*, vol. 4, no. 6, 2018.

[21] M. Streun *et al.*, “PhenoPET: A dedicated PET scanner for plant research based on digital SiPMs (DPCs),” in *2014 IEEE Nuclear Science Symposium and Medical Imaging Conference, NSS/MIC 2014*, 2016.

[22] A. D. Seminar, “Silicon based photodetection in science Table of Contents :,” 2016.

[23] M. Miller *et al.*, “Characterization of the Vereos Digital Photon Counting PET System,” *J. Nucl.*

Med., 2015.

[24] P. Vereos and D. Pet, “Proven accuracy inspires confidence Empowering the people behind the image.”

[25] Philips, “Digital Photon Counting technology overview,” 2016.

[26] M. G. Bisogni, A. Del Guerra, and N. Belcari, “Medical applications of silicon photomultipliers,” *Nuclear Instruments and Methods in Physics Research, Section A: Accelerators, Spectrometers, Detectors and Associated Equipment*, vol. 926, no. November 2018. Elsevier Ltd, pp. 118–128, 2019.

[27] R. D. Badawi *et al.*, “First Human Imaging Studies with the EXPLORER Total-Body PET Scanner*,” *J. Nucl. Med.*, vol. 60, no. 3, pp. 299–303, 2019.

[28] P. Lecoq, “Development of new scintillators for medical applications,” *Nucl. Instruments Methods Phys. Res. Sect. A Accel. Spectrometers, Detect. Assoc. Equip.*, vol. 809, pp. 130–139, 2016.

[29] “Normativa - CSN.” [Online]. Available: https://www.csn.es/normativa. [Accessed: 14-Jun-2019].

[30] National Cancer Institute, “What Is Cancer? - National Cancer Institute,” 2015.

[31] M. Plummer, C. de Martel, J. Vignat, J. Ferlay, F. Bray, and S. Franceschi, “Global burden of cancers attributable to infections in 2012: a synthetic analysis,” *Lancet Glob. Heal.*, vol. 4, no. 9, pp. e609–e616, Sep. 2016.

[32] I. nacional del cancer Cancer, “Estadísticas del cáncer - National Cancer Institute,” *Instituto Nacional De Cancerologia*, 2017. [Online]. Available: https://www.cancer.gov/espanol/cancer/naturaleza/estadisticas. [Accessed: 31-May-2019].

[33] J. F. Eary, “Nuclear medicine in cancer diagnosis,” *Lancet*, vol. 354, no. 9181. Elsevier, pp. 853–857, 04-Sep-1999.

[34] A. Almuhaideb, N. Papathanasiou, and J. Bomanji, “18F-FDG PET/CT imaging in oncology,” *Annals of Saudi Medicine*, vol. 31, no. 1. King Faisal Specialist Hospital and Research Centre, pp. 3–13, 2011.

[35] P. Digital and P. Counting, “Module-TEK,” 2014.

[36] R. Bdnf and E. Kit, “Product Manual,” no. 15, pp. 1–5, 2000.

[37] C. Ompact, O. R. Att, and R. E. C. Hiller, “H e r m o,” no. 845, pp. 0–1.

[38] “CP10G14 Aluminum Cold Plate with 4-Pass Copper tube, straight fittings | AMS Technologies.” [Online]. Available: https://www.amstechnologies-webshop.com/cp10g14-aluminum-cold-plate-with-4-pass-copper-tube-straight-fittings-6071005?c=375. [Accessed: 03-Jun-2019].

[39] “BGO and LYSO Crystals – Omega Piezo.” [Online]. Available: http://www.omegapiezo.com/crystal-scintillators/. [Accessed: 10-Jun-2019].

[40] “Borosilicate or equivalent Windows | Low Expansion Borosilicate or equivalent glass | Standard float sheet material.” [Online]. Available: https://www.knightoptical.com/stock/optical-components/uvvisnir-optics/windows/borosilicate-or-equivalent--windows/. [Accessed: 03-Jun-2019].

[41] Saint-gobain, “Safety data sheet BC-630 Silicone Grease,” 2017.

[42] Ultimaker BV, “Ultimaker 3: Unrivaled print quality,” 2019. [Online]. Available: https://ultimaker.com/en/products/ultimaker-3. [Accessed: 03-Jun-2019].

[43] “Sodium-22.” [Online]. Available: https://www.ld-didactic.de/software/524221en/Content/Appendix/Na22.htm. [Accessed: 04-Jun-2019].

[44] “Radioactive Sources; Isotopes and Uranium Ore.” [Online]. Available: https://www.imagesco.com/geiger/radioactive-sources.html. [Accessed: 14-Jun-2019].

[45] Organismo Internacional de Energía Atómica, “Normas de seguridad del OIEA. Protección

radiológica y seguridad de las fuentes de radiación: Normas básicas internacionales de seguridad. Requisitos de Seguridad Generales. Parte 3," *Normas Segur. del OIEA*, 2016.

[46] D. Schug *et al.*, "Data Processing for a High Resolution Preclinical PET Detector Based on Philips DPC Digital SiPMs," *IEEE Trans. Nucl. Sci.*, vol. 62, no. 3, pp. 669–678, 2015.

[47] "PreLude^{TM} 420 crystal Cerium doped Lutetium | Products | Saint-Gobain Crystals." [Online]. Available: https://www.crystals.saint-gobain.com/products/prelude-420-LYSO. [Accessed: 16-Jun-2019].

[48] C. J. Thompson *et al.*, "Evaluation of high density pixellated crystal blocks with SiPM readout as candidates for PET/MR detectors in a small animal PET insert," *IEEE Trans. Nucl. Sci.*, vol. 59, no. 5 PART 1, pp. 1791–1797, 2012.

[49] "Fundamentos para la utilización de la terminología anatómica - Monografias.com." [Online]. Available: https://www.monografias.com/trabajos61/terminologia-anatomica/terminologia-anatomica.shtml. [Accessed: 13-Jun-2019].

[50] E. Frattini *et al.*, "Clinical Reasoning: A 75-year-old man with parkinsonism, mood depression, and weight loss," *Neurology*, vol. 90, no. 12, pp. 572–575, 2018.

[51] "Thorlabs - MB3090/M Aluminum Breadboard, 300 mm x 900 mm x12.7 mm, M6 Taps." [Online]. Available: https://www.thorlabs.com/thorproduct.cfm?partnumber=MB3090/M. [Accessed: 13-Jun-2019].

ANNEX A

CP10G14 Aluminium Cold Plate specifications

Length Cold Plate (mm):	152.4
Width Cold Plate (mm):	88.9
Performance (°C/W):	0.015
Fluid Compatibility:	Water, Common Coolants
Wetted Path:	Copper
Mounting Surface :	Single-Sided
Tube (mm):	9.5
Configuration:	4-Pass
Fitting:	Straight (SB)
Plate Material :	Aluminum
Maximum Pressure (psi):	150
Maximum Flow Rate (lpm):	8
Thickness (mm):	12.7
Type:	Tubed Cold Plate

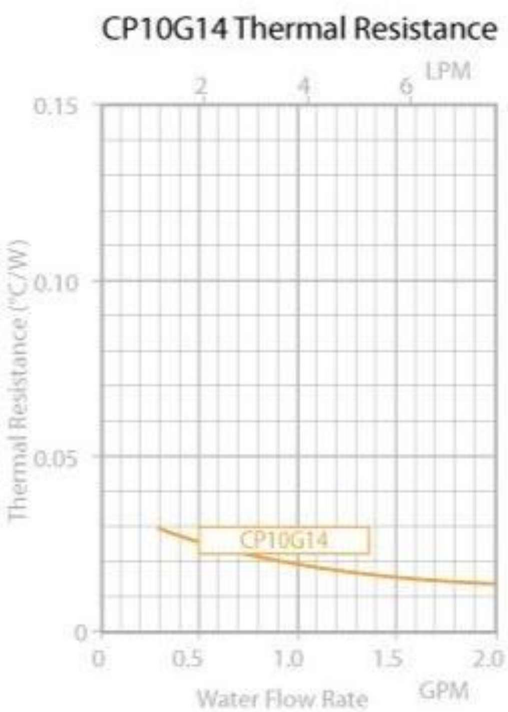

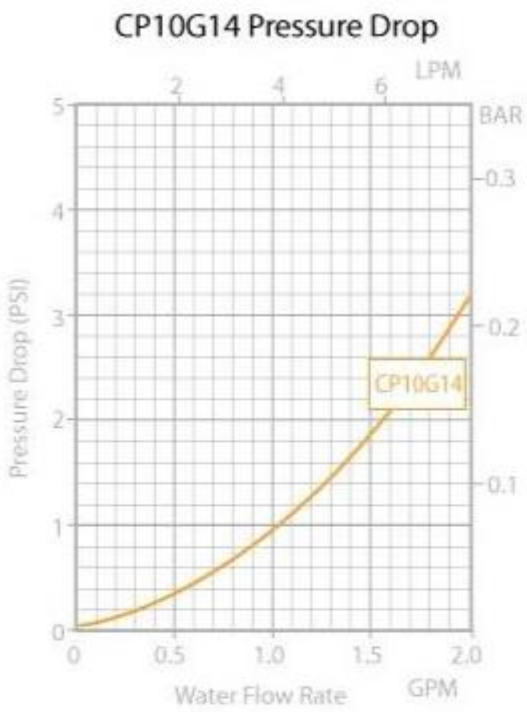

ANNEX B

Aluminium plate connector between the detector and the cold plate

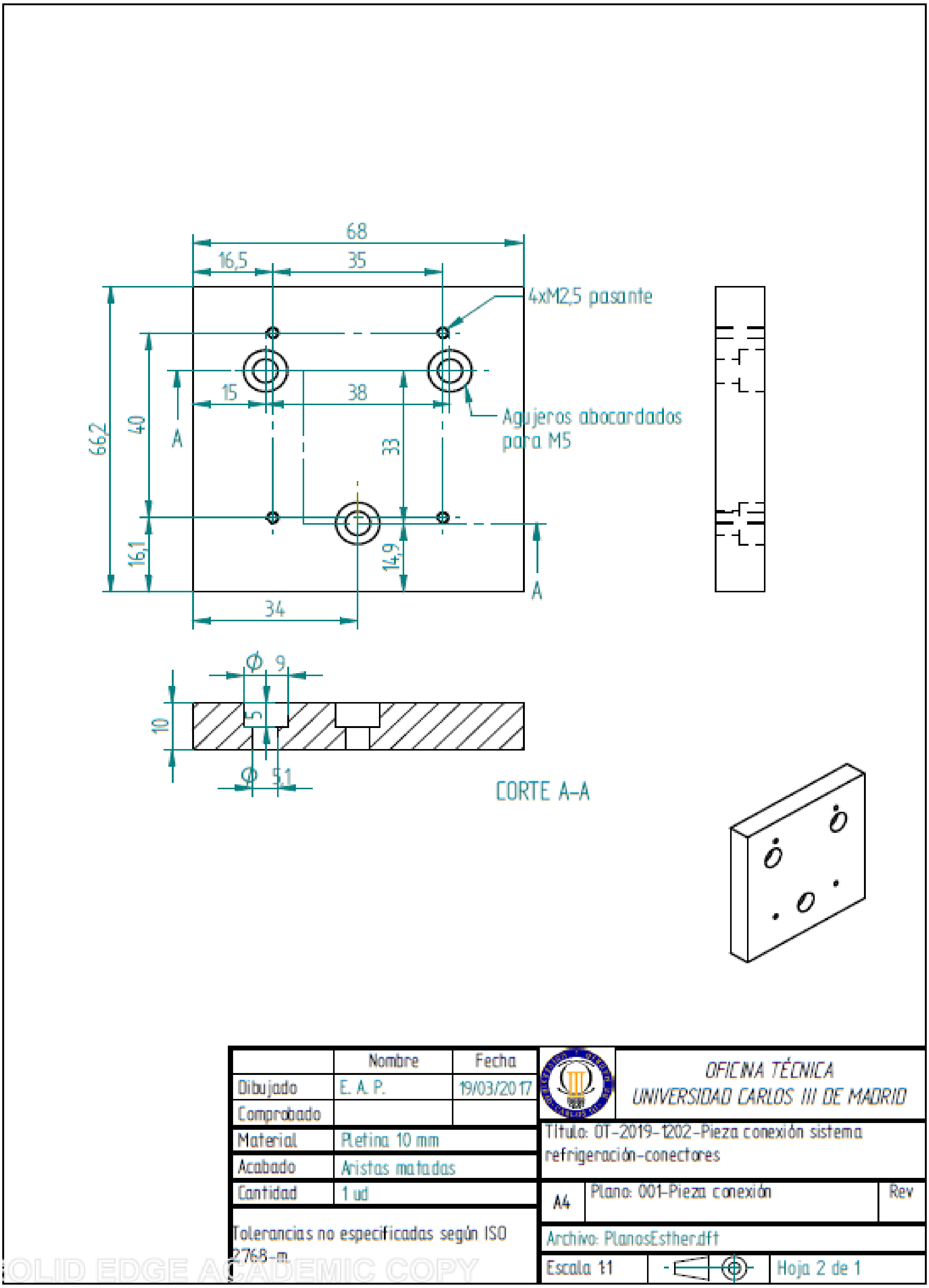

ANNEX C

Light guide technical information